5-2019

Non-Contact Human Motion Sensing Using Radar Techniques

Farhan Quaiyum

University of Tennessee, fquaiyum@vols.utk.edu

To the Graduate Council:

I am submitting herewith a dissertation written by Farhan Quaiyum entitled "Non-Contact Human Motion Sensing Using Radar Techniques." I have examined the final electronic copy of this dissertation for form and content and recommend that it be accepted in partial fulfillment of the requirements for the degree of Doctor of Philosophy, with a major in Electrical Engineering.

<div align="right">

Aly E. Fathy, Major Professor

</div>

We have read this dissertation and recommend its acceptance:

Gong Gu, Jens Gregor, David R. Bassett Jr.

<div align="right">

Accepted for the Council:

Dixie L. Thompson

Vice Provost and Dean of the Graduate School

</div>

(Original signatures are on file with official student records.)

Non-Contact Human Motion Sensing Using Radar Techniques

A Dissertation Presented for the
Doctor of Philosophy
Degree
The University of Tennessee, Knoxville

Farhan Quaiyum
May 2019

Dedication

To my parents, Abdul Quaiyum and Tahmina Banu, and my wife, Sabikun Nahar. Your encouragement and support made all of this possible

ACKNOWLEDGEMENTS

ABSTRACT

Human motion analysis has recently gained a lot of interest in the research community due to its widespread applications. A full understanding of normal motion from human limb joint trajectory tracking could be essential to develop and establish a scientific basis for correcting any abnormalities. Technology to analyze human motion has significantly advanced in the last few years. However, there is a need to develop a non-invasive, cost effective gait analysis system that can be functional indoors or outdoors 24/7 without hindering the normal daily activities for the subjects being monitored or invading their privacy. Out of the various methods for human gait analysis, radar technique is a non-invasive method, and can be carried out remotely. For one subject monitoring, single tone radars can be utilized for motion capturing of a single target, while ultra-wideband radars can be used for multi-subject tracking. But there are still some challenges that need to be overcome for utilizing radars for motion analysis, such as sophisticated signal processing requirements, sensitivity to noise, and hardware imperfections. The goal of this research is to overcome these challenges and realize a non-contact gait analysis system capable of extracting different organ trajectories (like the torso, hands and legs) from a complex human motion such as walking. The implemented system can be hugely beneficial for applications such as treating patients with joint problems, athlete performance analysis, motion classification, and so on.

TABLE OF CONTENTS

LIST OF TABLES

LIST OF FIGURES

CHAPTER ONE
INTRODUCTION AND BACKGROUND

1.1 Human Motion Sensing

Human motion analysis has been recently receiving steadily increasing attention from researchers in different fields due to its wide range of applications [1.1]. These applications include, segmenting the parts of the human body for athletic performance analysis [1.2] and medical diagnostics [1.3-1.5], automatically monitoring human activities in security-sensitive areas [1.6], elderly monitoring [1.7], creating man–machine user interfaces [1.8], smart video conferencing [1.9], and so on. Figure 1.1 shows some of the applications where human motion analysis is of significant importance.

A full understanding of normal motion from human limb joint trajectory tracking is essential to develop and establish a scientific basis for correcting any abnormalities. Accurate reliable knowledge of gait characteristics at a given time, and even more importantly, monitoring and evaluating them over time, will enable early diagnosis of diseases and their complications and help to find the best treatment. Various techniques have been developed to perform such motion analysis. In [1.10], Wahab et al. developed an ultrasonic system in wearable instrumented shoes for gait analysis measurement in sports applications. Middleton et al. [1.11] presented a floor sensor consisting of 1536 individual sensors arranged in a 3 m $\times$ 0.5 m rectangular strip as a prototype for a gait recognition system. A single camera based approach was proposed in [1.12] where the gait

Figure 1.1: Applications of human motion sensing (a) Athlete performance analysis, (b) Remote monitoring in security sensitive areas, (c) Smart video conferencing, (d) Medical diagnostics, (e) Elderly monitoring.

features from various viewing angles were normalized into a common viewing angle to achieve a stable, noise-robust video based gait recognition system. In [1.13], a low-cost, wearable, and wireless insole-based gait analysis system was studied that provided kinetic measurements of gait by using low-cost force sensitive resistors. Salarian et al. [1.14] offered an ambulatory gait analysis method using body-attached gyroscopes to estimate spatio-temporal parameters of gait for normal and pathologic motions. Figure 1.2 shows some of the techniques currently used in human motion analysis. Typically, use of video techniques has proven to be an attractive option for gait analysis due to its remote monitoring capability, high accuracy and ease of data analysis. But the cameras that are utilized are still expensive and require large storage of data. In addition, the subject has to be always in sight of the camera for the analysis. And since the video needs to be recorded, it hinders the privacy of the subject under test, especially in applications that need continuous monitoring. Ultrasonic systems, on the other hand, have the advantage of being low cost as well as immune to interferences. But they have limited range and are thus mounted on the subject to measure relative speed and distance. Meanwhile, the contact sensors like the pressure/inertia sensors typically provide very high accuracy and are insensitive to the surrounding environment. But each organ to track requires separate sensors and the combination of the multiple sensors and the mesh of wires for collecting data makes the method very inconvenient for the subject under test. Then there is floor mat sensors where the subject needs to move within a certain area with a mesh of embedded sensors. Typically these mats provide very accurate results and are insensitive to noise and/or interference. But these are only suitable for analyzing the lower components that
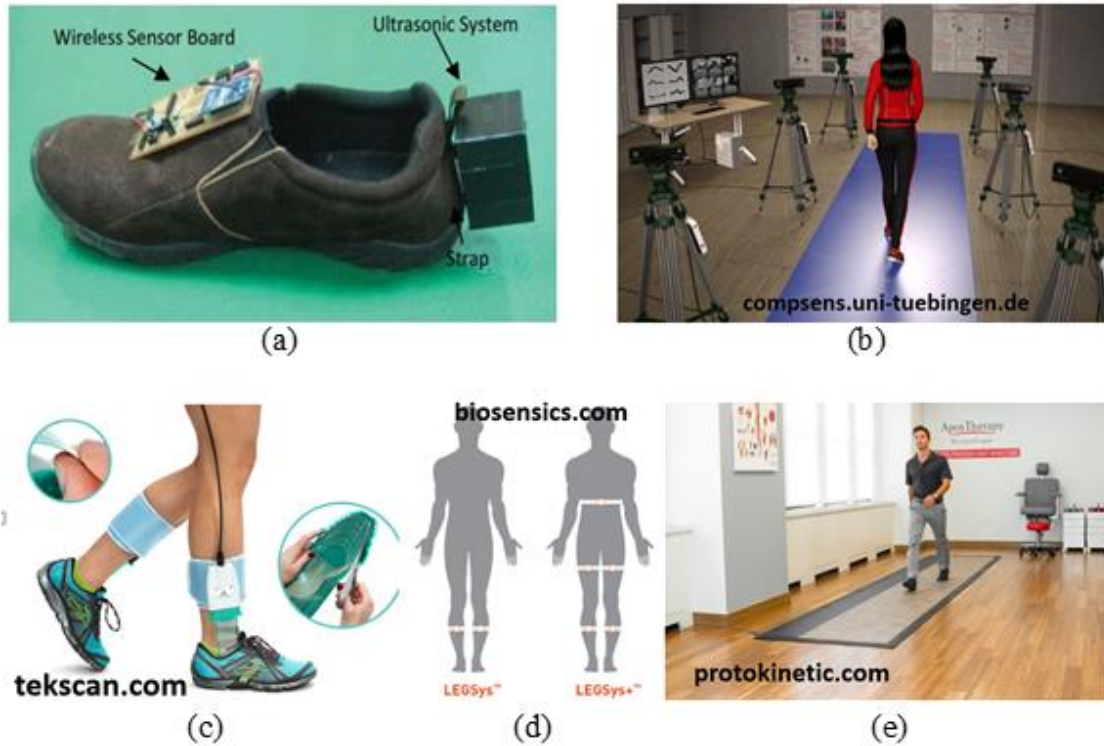
Figure 1.2: Human motion analysis techniques: (a) ultrasonic system in wearable instrumented shoes presented in [1.10], (b) motion sensing using multi-camera video analysis, (c) pressure/force sensors in shoes, (d) wearable gyroscope sensors, (e) floor mat sensor.

come in contact with the mats and the range is limited by the size of the mats. A summary of the advantages and disadvantages of the different traditional techniques mentioned above is presented in Table 1.1.

Thus, there is a need to develop a non-invasive, cost effective system that can be installed indoors or outdoors and can be functional 24/7 without hindering the normal daily activities for the subjects being monitored or invading their privacy. In applications where long-term or continuous monitoring is essential, radar systems have appeared as an attractive solution to this complex problem. Gait analysis using radar systems offers a non-contact method that can cover a long range, can be implemented using low-cost single tone radars and can even perform simultaneous multi-subject tracking with the help of wideband systems.

Table 1.1: Advantages and demerits of different motion analysis methods.

Method	Pros	Cons
Video	- Non-contact method - High accuracy - Relatively easy to analyze data	- Expensive to setup - Line of sight requirement - Privacy problem - Large data storage requirement
Ultrasound	- Inexpensive setup - Robust to interference	- Limited range - Long processing time
Pressure / Inertia sensors	- High accuracy - Low cost sensors - Environment insensitive	- Individual sensor for each organ - Inconvenience to wear sensors
Floor sensor	- High accuracy - Noise/interference insensitive	- Contact method - Can only analyze lower leg - Range limited by sensor size

1.2 Gait Parameters to Study

Gait analysis in general is the methodical examination of a person's movement that serves to provide a unique, personal motion "map." That "map" actually reveals the different information within your body like level of mobility, habit, strength, stability, flexibility and so on. This analysis of movement can be for a walking person, or a running person, or even a person jogging on a treadmill. This research is primarily focused on the analysis of human walking. The series of events that occur during normal human walking can be described by as a gait cycle. According to Whittle [1.15], it is defined as the time interval between two successive occurrences of one of the repetitive events of walking. There are two main phases during the gait cycle: the 'stance' phase and the 'swing' phase. The stance phase occurs when the foot is in ground contact, whereas the swing phase occurs when there is no contact with the walking surface. The stance phase occurs for about 60% of a whole gait cycle and the swing phase occurs for about 40%. Figure 1.3 depicts the gait cycle.

So, in general, human gait research conducts the qualitative and quantitative evaluation of the various factors that characterize the gait. Depending on the application and the field of research, the factors of interest can vary [1.16]. For instance, for remote monitoring in security sensitive areas, interest may center on distinguishing and identifying persons based on a general characterization of their body posture and the movements between the subject's different body segments when walking [1.17]. However, in the field of sports, research may focus on the analysis of the joint trajectories, as well as, the different forces
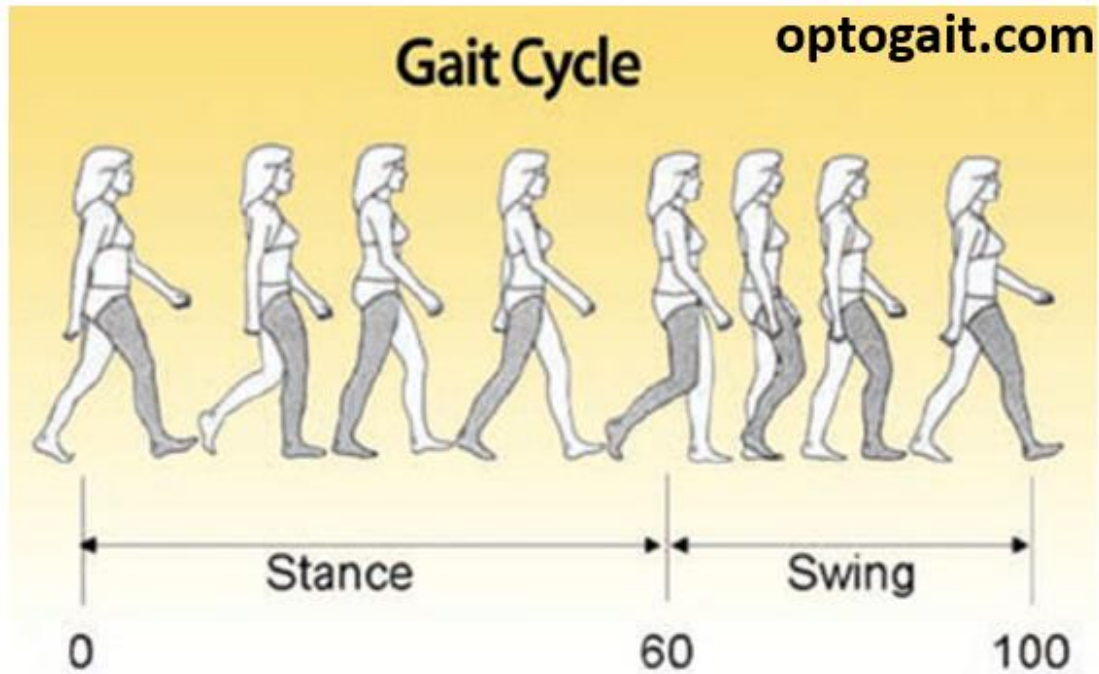
Figure 1.3: Gait cycle showing the stance and swing phases and their relative duration. The gait cycle comprises of one step each from each leg beginning and ending in the same position. Here the phases are shown with respect to the right leg of the subject: stance phase when the right leg is planted on the ground, swing phase when it is in the air. Also, note that the two hands moves in opposite directions to each other.

exerted on muscles of interest through Electromyography (EMG) [1.18]. As an example, there are clinical studies on the elderly which link changes in various gait characteristics such as poor balance, slower pace, shorter steps, lower walking velocity and higher cadence to gait deficiency [1.19-1.20]. Table 1.2 highlights the general gait parameters of interest for different applications.

It can be observed from Table 1.2 that extracting joint velocities is an important factor of analysis for any application of interest. Figure 1.4 shows example results of joint velocities obtained from a human walking model developed in [1.21] moving with a constant velocity of 1 ms^{-1}. The plots show the instantaneous velocities of different body parts including the

Table 1.2: Overview of gait parameters in relation to various applications [1.16].

GAIT PARAMETER	CLINICAL	SPORTS	SECURITY
STEP LENGTH	√	√	√
STANCE/SWING PHASE	√	√	
STEP TIME	√		
CADENCE	√	√	
AVERAGE SPEED	√	√	√
JOINT ANGLES	√	√	
FORCE ON MUSCLES	√	√	
BODY POSTURE	√	√	√
JOINT VELOCITIES	√	√	√

legs, the hands and the torso during a complete walking cycle. We can easily notice that, by performing some rudimentary analysis on the joint velocity plot, we can extract other useful gait parameters of interest such as step length, gait phase, step time, cadence and average speed. For example, the torso velocity observed in Figure 1.4 would represent the average walking velocity. The time interval between the maximum velocity points of the two legs multiplied by the average velocity would give the step length. We can also observe the time duration during which the foot velocity is higher than zero to obtain step time and similarly obtain the gait phases as well. Thus, this research focuses on the extraction of joint velocities during motion using non-contact method which can be useful in a number of different practical applications.
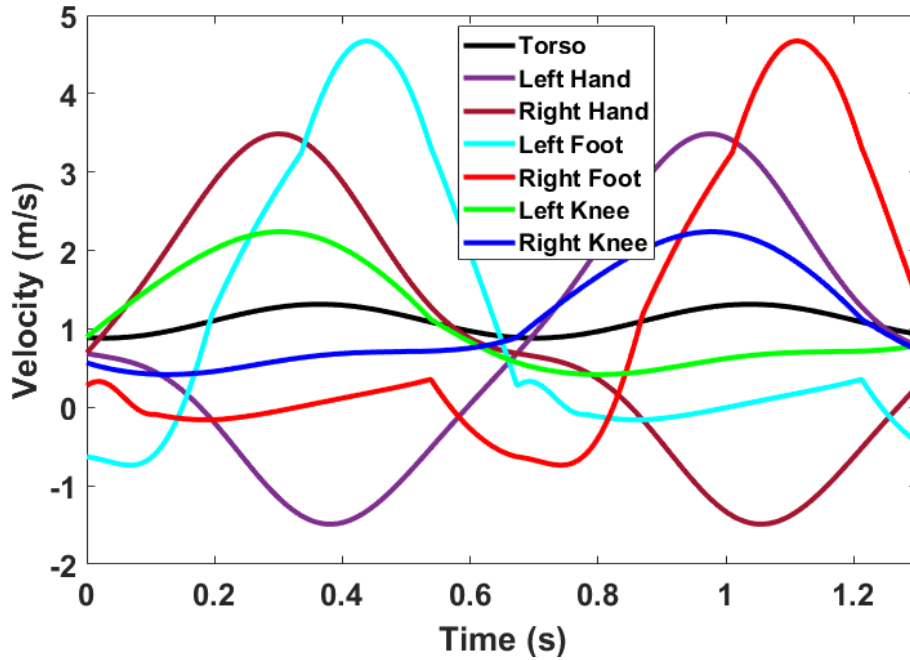
Figure 1.4: Joint velocities extracted from a human walking model developed in [1.21].

9

1.3 Radar Fundamentals

Radar, an acronym for radio detection and ranging, is an electronic device used to transmit an electromagnetic signal to a target and to receive the reflected echo, on the basis of which the target's speed and absolute distance can be extracted [1.22]. A simplified block diagram of a radar is shown in Figure 1.5. The transmit signal in time domain can be expressed as:

$$T(t) = cos(\omega_0 t) \tag{1.1}$$

where ω_0 is the fundamental angular frequency.

The signal travels in the air and gets reflected from a subject in front of the radar. Thus, the signal at the receiving antenna can be expressed as:
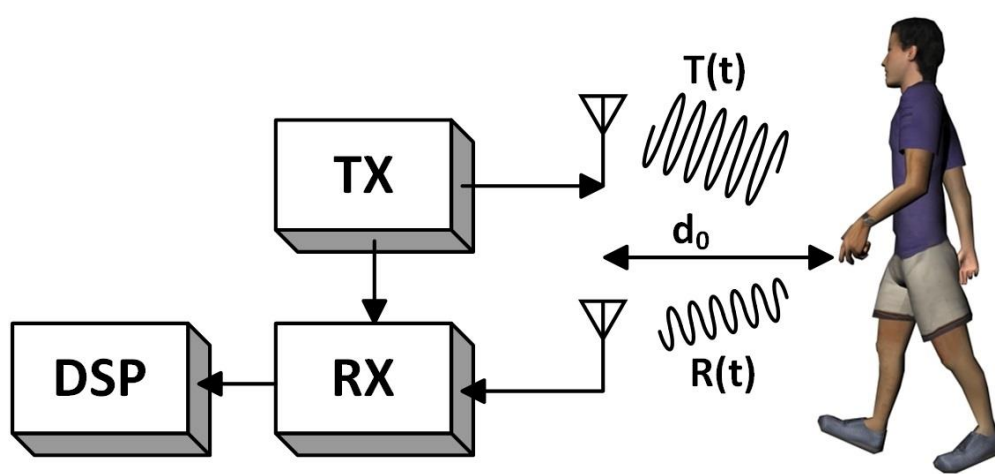
Figure 1.5: Simplified block diagram of the radar system for noncontact biomedical applications.

$$R(t) = A\cos\left(\omega_0 t + \frac{2\pi}{\lambda}(2d_0 + 2d(t))\right) \qquad (1.2)$$

where d_0 is the static distance of the subject to the transmitter (TX) and $d(t)$ represents the displacement due to human motion, A is the amplitude of the received signal and λ is the wavelength. This received signal is mixed with a part of the transmitted signal to obtain the baseband signal, which after low-pass filtering has the form:

$$x_{BB}(t) = B\cos\left(\frac{2\pi}{\lambda}(2d_0 + 2d(t))\right) \qquad (1.3)$$

where B is and the magnitude of the received baseband signal. The variable part of the phase $\varphi(t) = \frac{2\pi}{\lambda}2d(t)$ is the part that used for feature extraction and gait analysis. Use of radar for motion analysis can provide advantages such as:

- It is a non-contact method which does not cause any inconvenience for the subject under test.
- It can cover a long range.
- Motion analysis through wall/barrier is possible.
- It can be implemented through very low cost hardware compared to the video techniques.
- Simultaneous multi-person tracking is possible through the use of wideband radars.

11

1.4 Radar Architectures

Radar systems can be basically of two types: single tone radar (CW) and wideband (UWB) radar. Continuous wave (CW) or Doppler radars are typically the simplest to implement with inexpensive components, which makes it an attractive choice for low-cost portable motion sensing systems. However, ultra-wideband (UWB) radars in general provide many advantages over the CW radars such as: ability to resolve closely spaced targets in range, reduction of multi-path, multi-target identification capabilities and so on. UWB radars signals can be implemented in several ways like impulse radio, stepped frequency continuous wave (SFCW) and frequency modulated continuous wave (FMCW). In the UWB impulse radio (UWB-IR) radar architecture, the signal has a large instantaneous bandwidth. Thus, the receiver (RX) requires high performance Analog to Digital Converters (ADCs) or other sophisticated methods to capture the signal, which makes it very expensive. In SFCW or FMCW radars, however, the wideband signal is emulated by sweeping the frequency in discrete or continuous steps over a wide bandwidth. The narrow instantaneous bandwidth combined with the large effective bandwidth (sequentially over many pulses) of these radars imply that the hardware requirements become less stringent. Lower-speed ADCs and lower level processors can be used. Moreover, the receiver bandwidth is smaller, resulting in lower noise bandwidth and higher signal-to-noise ratio thereby increasing the radar sensitivity. Compared to UWB-IR waveforms, stepped frequency or frequency modulated waveforms require lower AD conversion sampling rates, low peak power sources, and less resource requirement for processing smaller sets of data. Another disadvantage of the UWB-IR architecture is the difficulty in detecting the

target's speed by exploiting the Doppler effect like in conventional CW radars. The speed information is obtained by dividing space displacement by the time interval which means that for a good accuracy in velocity, high accuracy in target position is required [1.23]. In case of the FMCW radars, one of its disadvantages is due to the frequency being swept in a continuous manner or in very fine steps, it is very difficult to compensate the amplitude and phase distortions for all different frequencies. For SFCW, this calibration becomes much simpler since only a discrete number of frequencies (with wide frequency steps) need to be calibrated. In addition, techniques such as compressive sensing method, where a fraction of the total number of frequencies can be randomly chosen within the band without degrading the performance, can be implemented for SFCW systems. This is not possible in the FMCW case, where the frequency needs to be swept continuously. Table 1.3 compares the different radar techniques according to their characteristics.

Table 1.3: Comparison between different radar technologies.

	CW	UWB	FMCW	SFCW
Localization	No	Yes	Yes	Yes
Multiple Subjects	No	Yes	Yes	Yes
ADC Speed	Low	Fast	Low	Low
Calibration[*]	-	-	Difficult if nonlinearity exists	Relatively Straightforward

[*]Compensation of the amplitude and phase distortion for different frequencies

Thus, in order to determine the optimal architecture aiming at human sensing applications, we are proposing to investigate two radar architectures: CW radar, and SFCW radar. As opposed to CW radar that can only determine target's speed, SFCW radar can determine simultaneously both the target's speed and absolute distance [1.24]. The characteristics of these architectures, together with their advantages and disadvantages, are detailed below.

1.4.1 Continuous Wave Radar

Continuous Wave radar, or Doppler radar, is a type of radar system that transmits a single-tone continuous-wave signal, which is reflected by a target and then demodulated in the receiver. It is used to determine the target's speed. If $D=do+d(t)$ is the distance from the radar to the target, the total number of wavelengths λ contained in the two-way path is $2D/\lambda$. Since one wavelength corresponds to an angular excursion of 2π radians, the total angular excursion φ traveled by the electromagnetic wave is $4\pi D/\lambda$ radians. If the target is moving, D and the phase φ are changing continuously. A change of φ with respect to time is equal to a frequency, such as the Doppler angular frequency ω_d is:

$$\omega_d = 2\pi f_d = \frac{d\varphi(t)}{dt} = \frac{4\pi}{\lambda} \frac{d\,(d(t))}{dt} = \frac{4\pi v(t)}{\lambda} \tag{1.4}$$

where f_d is the doppler frequency shift and $v(t)$ is the radial target speed. The Doppler frequency shift is therefore

$$f_d = \frac{2v_t}{\lambda} = \frac{2v_t f_c}{c} \tag{1.5}$$

14

where f_c is the radar center frequency. Thus, a velocity of 1 ms^{-1} detected by a radar with operating frequency of 2.45 GHz would correspond to a Doppler frequency shift of about 16.33 Hz. We can also see that as we increase the operating frequency, larger Doppler frequency shifts are generated which increases the sensitivity.

The main advantage of a CW radar is measuring the target's speed without ambiguity as long as the Nyquist–Shannon sampling theorem is satisfied. Which means that the frequency at which data is sampled (equivalent to the pulse repetition frequency of the CW radar) has to be at least twice the maximum Doppler frequency generated by the movement of interest. Moreover, as opposed to ultra-wideband architectures, it presents a simpler architecture and it does not require large isolation between the antennas since the presence of a portion of the transmitted signal in the receiver is not harmful [1.25]. In fact, both the leakage due to poor isolation and stationary targets, such as furniture, produce a DC baseband signal that has no contribution in the Doppler frequency shift so it can be easily filtered.

1.4.2 Stepped-Frequency Continuous Wave Radar

A SFCW radar, also known as frequency-domain radar, transmits and receives a group of N coherent CW pulses whose frequencies are increased from pulse to pulse by a fixed frequency increment Δf, as shown in Figure 1.6. The frequency of the n-th pulse can be written as:

$$f_n = f_0 + (n-1)\Delta f \tag{1.6}$$
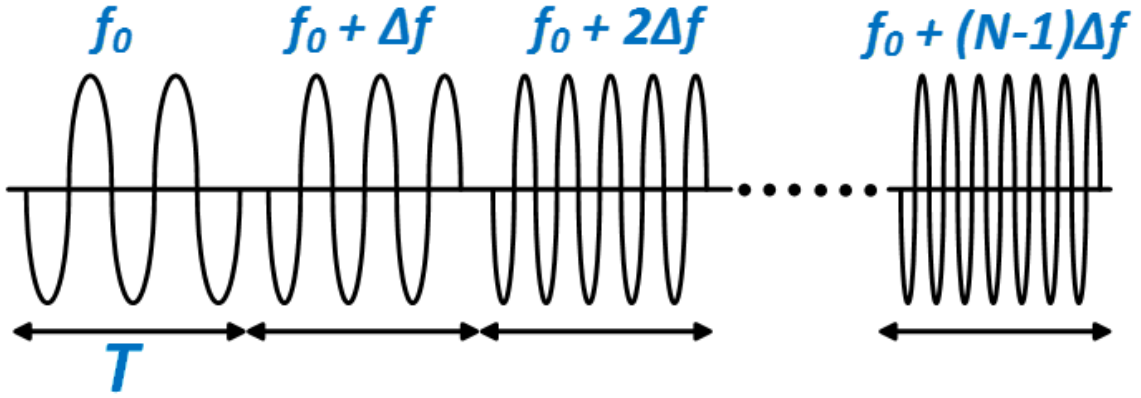
Figure 1.6: Stepped frequency waveform. Limited number of cycles are shown at each interval T for illustration purposes.

where f_0 is the starting carrier frequency and Δf is the frequency step size, that is, the change in frequency from pulse to pulse. Each pulse is T seconds wide, the minimum value of which is dependent on the settling time of the frequency generator. A group of N pulses, also called burst or frame, is transmitted and received before any processing is initiated to realize a high-resolution measurement of the signal being measured. The burst interval is called the coherent processing interval (CPI).

The total bandwidth of the signal is $N\Delta f$. However, since the frequency is constant within the individual pulse, its bandwidth is approximately equal to the inverse of the pulse width. These pulses have narrow bandwidths, thus making the instantaneous bandwidth of the radar narrow which improves the radar sensitivity.

16

1.5 Conclusion

This chapter highlighted the importance of human motion analysis in various applications such as athlete performance analysis, elderly monitoring, medical diagnostics, remote monitoring in security sensitive areas. The traditional techniques of motion analysis were discussed and it was observed that all of those had some shortcomings. There is a need for a low-cost motion analysis system that can perform non-contact, full-body analysis from a distance and radar systems provide all these capabilities. The basic working principle of such systems for gait analysis was introduced here along with discussing the different types. It was observed that the CW radar is the most convenient system to implement due to its simplicity and inexpensive component requirement but does not provide range resolution capabilities. In order to achieve that feature that would provide localization and multi-subject tracking capabilities, SFCW radars can be a convenient solution due to its low-cost data acquisition and simpler calibration requirements compared to UWB-IR and FMCW radar systems. That is why, we focused our research mainly on these two types of radars. The subsequent chapter will examine some of the previous research on radar systems for human motion analysis.

CHAPTER TWO
LITERATURE REVIEW

In general, human locomotion as a whole is complex, but it consists of a combination of different limb joints of the body. Hence, if the body is irradiated with a radar, then different limb joints will cause an ensemble of micro-Doppler shifts which can be distinctly detected by a sensitive radar. Various radar technologies and signal processing schemes have been previously utilized to perform human motion analysis.

2.1 Radar Hardware

One of the first attempts in gait analysis using radar techniques was presented by Geisheimer et al. in [2.1]. They proposed a fully coherent, continuous-wave (CW) radar operating near 10.5 GHz to detect the motion signatures corresponding to the walking human gait. Figure 2.1 (a) shows the implemented system. They conducted the experiments in a fifty-foot long room suitable for collecting gait data. After that, they processed the collected data to show the combined time-frequency spectrogram: the spectrum of frequencies of the signal as they vary with time without extracting individual limb motions. M. Otero [2.2] implemented a low-cost, low-power CW radar for remote sensor applications like: security, perimeter protection, and border monitoring. Spectral analysis using Fourier transform techniques was used on the Doppler signatures captured by the radar to identify some key features of the human walking like the walking speed and stride length. But the analysis was only intended to extract very basic information that could be

used to determine if a person was present or not. It was not intended to identify individuals or classes of people from their gait motion. Munoz-Ferreras et al. [2.3] implemented two integrated radar systems, one at C-band, the other at K-band to detect and compare the time-frequency spectrogram performance from Doppler-radar signatures. The C-band radar IC operated at 5.8 GHz and the K-band radar at 24 GHz with both having 8 dBm transmitted output power. Their experiments showed that the higher frequency radar demonstrated better performance in terms of spectrogram resolution. In [2.4], a single-frequency continuous-wave Doppler radar sensor implemented with a redundant single-input multiple-output (SIMO) front-end was presented for localization of moving objects. They operated the CW radar at 5.8 GHz and used a single transmitter and three receivers to localize a moving object in front of the radar. Lv et al. [2.5] proposed a high dynamic range Doppler radar sensor for reconstructing time-domain motion information. They used a 2.36 GHz tone with 25 dBm transmit power to track the walking velocity of human subject. In [2.6], V. C. Chen implemented an X-band CW radar and performed experiments in a typical environment in the presence of other objects. Since CW radars are not inherently capable of clutter suppression, the range profiles showed strong backscattering from the background objects and unwanted moving objects. He used a notch filter to suppress the stationary clutter from the moving subject. Time frequency analysis of the filtered signal showed spectrograms for different complex hand and leg movements, but again, the individual features could not be extracted as shown in Figure 2.1 (b). In addition to clutter suppression problem, CW radars can also suffer from DC offset issues and quadrature imbalance. DC offset can saturate or limit the dynamic range of the baseband

<center>(a)</center> <center>(b)</center>
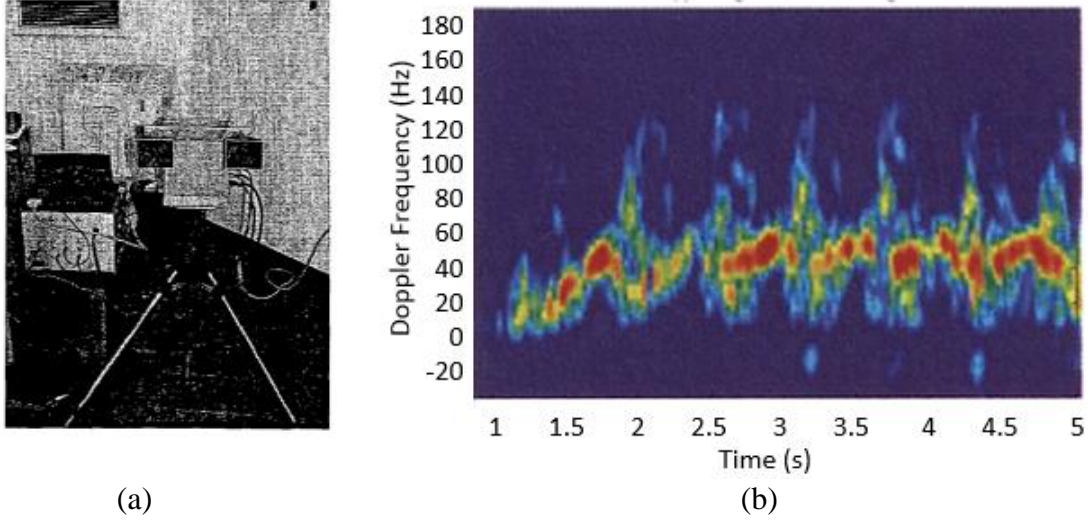
Figure 2.1: (a) 10.5 GHz CW radar reported in [2.1] which was one of the first attempts in gait analysis using radar systems. (b) Time frequency spectrogram for a walking subject detected by a X-band CW radar in [2.6].

amplifiers [2.7] whereas quadrature imbalance can distort the shapes of the detected physiological signals, resulting in motion tracking errors [2.8].

Wang et al. [2.9] utilized both a CW (continuous wave) radar and UWB-IR (ultra-wideband impulse radio) radar for human sensing applications. They used the CW as a low-cost option for single human activity monitoring, vital sign detection, etc., where target range information is not required. They utilized a novel superhetrodyne receiver to suppress low-frequency noise and included a digital downconverter module implemented in an FPGA. Meanwhile, the UWB-IR radar was more suitable for through-wall sensing, multiple-object detection, real-time target tracking, and so on, where a high-resolution range profile is

<center>20</center>

acquired together with a micro-Doppler signature. They employed a carrier-based transceiver and a novel equivalent time sampling scheme based on FPGA for narrow pulse digitization. They were able to perform through-wall detection of two people walking using the UWB-IR radar prototype, but they just demonstrated the overall time-frequency spectrogram without extracting the individual limb joint features. Figure 2.2 depicts some of their reported results. Ren et al. also used an UWB-IR radar in [2.10] to track the torso and leg features of a walking subject. They used a 400-700 ps pulse transmitted at a repetition rate of 75 Hz and used an equivalent time sampling technique implemented using an FPGA to capture the wideband reflected signal. Their ability to track the other organs like the hands, ankles and toes was limited by the low pulse repetition rate and weaker return signals from those organs. Figure 2.3 presents some of their results. Tang et al. [2.11]

(a)   (b)
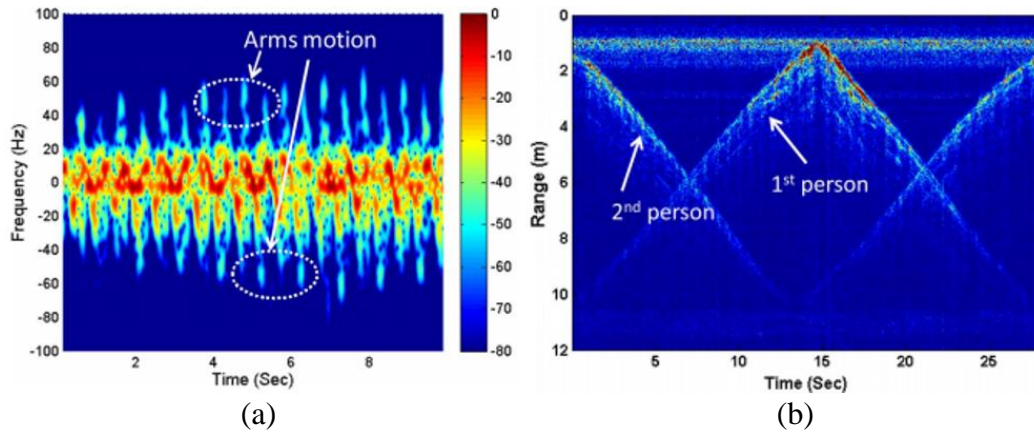
Figure 2.2: (a) Spectrogram of a person walking/jogging on the treadmill using the CW Doppler radar prototype in [2.9], (b) Range profile of two persons walking in opposite directions using the UWB pulse Doppler radar reported in [2.9].

21
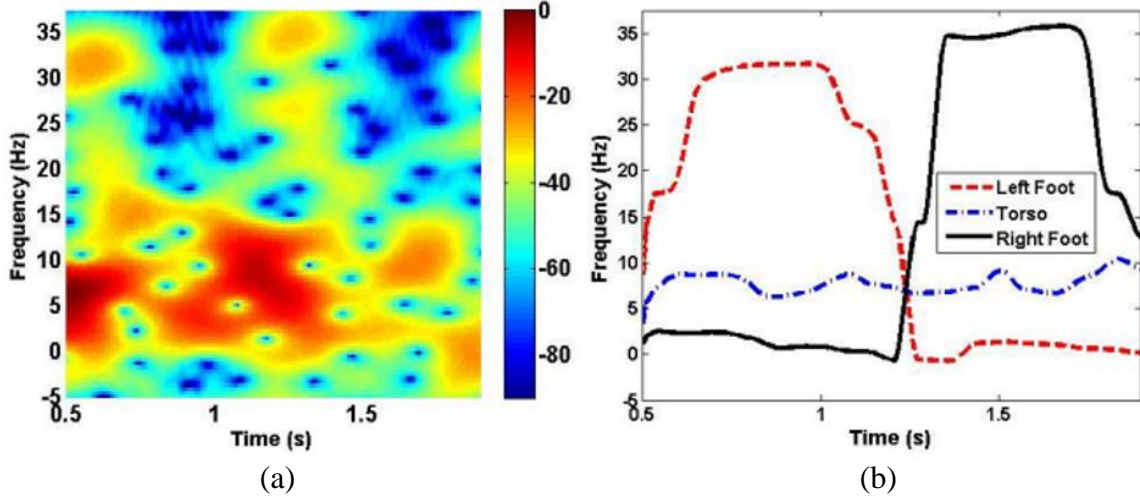
Figure 2.3: (a) Combined time-frequency spectrogram in for a walking person detected by an UWB-IR radar reported in [2.10], (b) Tracking of torso and the leg features.

utilized a combination of UWB radar and Doppler radar to perform short range indoor localization. They used the commercial DWM1000 UWB transceiver chip [2.12] from decawave as the UWB radar and a K-band Doppler radar InnoSenT IPS-154 [2.13] operating at 24.125 GHz to detect the walking trajectory of a human subject.

Maaref et al. studied possible solutions for the detection of human beings walking or even just moving behind a wall with the help of a UWB FMCW radar in [2.14]. They utilized a UWB fast frequency swept Yttrium Iron Garnet (YIG) source with a voltage to frequency characteristic that is very linear compared to a voltage controlled oscillator (VCO). Its maximum sweeping velocity was 200 μs/GHz which led to a minimum sweeping time of 0.4 ms for a frequency bandwidth of 2 GHz. Using a sweeping frequency range between

2-4 GHz, they investigated the possibility to track a person walking behind a brick wall. But the pulse intensity fluctuated all along the tracking duration and they did not perform any gait analysis. In [2.15], Wang et al. proposed a novel radar system for precise 2-D positioning and life activities surveillance. Operating in the 5.8-GHz industrial–scientific–medical (ISM) band with a 160-MHz bandwidth, the radar system incorporated both the FMCW mode and the interferometry mode based on a continuous waveform. The signal generation is performed using a National Instruments PXIe 1075 chassis with three function blocks, which costs about $7600. They used the radar to extract the micro-Doppler information of a series of motions performed by a person facing the radar. They showed the Doppler frequency shifts due to different movements but did not extract the individual features from the different organs as shown in Figure 2.4. Greneker [2.16] proposed to use human gait characteristics detected by radar to determine if a human subject is carrying a

(a)   (b)
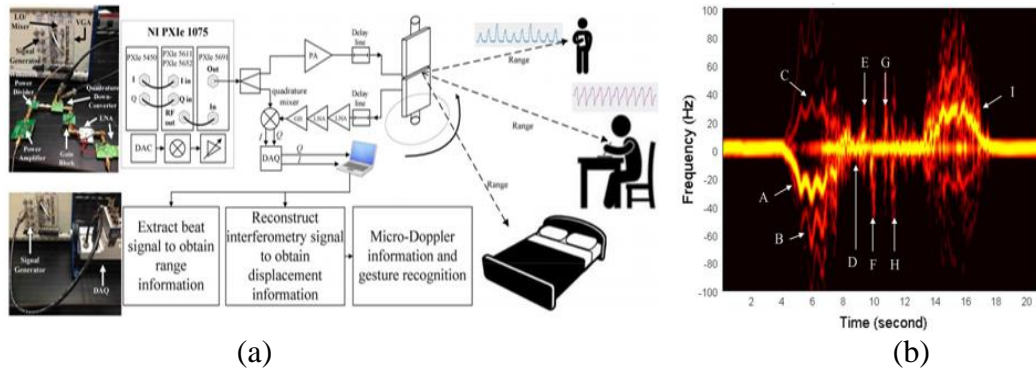
Figure 2.4: (a) Photograph of the FMCW radar system and experimental setup for indoor positioning and life activity monitoring reported in [2.15], (b) Micro-Doppler signatures extracted by the radar for a walking person.

23

concealed object under their clothes. Using an X-Band homodyne/frequency modulated-continuous wave radar (FM-CW) operating at a frequency of 10.525 GHz, they measured both the radar cross-section of an individual and the derived gait characteristics that are associated with individuals carrying a bomb on their body. But they only needed to track the thorax to make the classification, and did not track any other organs. Peng et al. [2.17] presented an FMCW radar operating at 5.8 GHz with 320 MHz chirp bandwidth and 3.5 ms frequency ramp period for human gesture recognition. They were able to detect the hand gesture motion of a subject in the presence of multiple targets, but they did not perform any tracking of the limb joints.

Lu et al. implemented a stepped-frequency CW (SFCW) radar in [2.18] to perform through wall imaging and motion detection. They used a local oscillator (LO) frequency synthesizer that generated the SFCW waveform, scanning repeatedly from 1.0 GHz to 2.0GHz at a frequency step 2MHz, where four parallel phase locked loops (PLLs) and an eight to one switch are used to increase the frequency sweeping speed which enabled a minimum sweeping time of 90 ms for the radar. Without performing gait analysis, they only generated images of a person standing and walking behind a wall and it was shown that the signal to clutter ratio (SCR) for the walking person was higher than the SCR for the standing person due to the larger position displacements during the coherent processing interval for the walking person. Thayaparan [2.19] utilized an SFCW radar operating between 8.9–9.4 GHz with 10 MHz step frequency and 20 Hz frame rate to analyze human motion in high noise environment.

Thus, we can see there has been plenty of research on radar systems for motion analysis. The summary of these hardware systems along with their limitations are listed in Table 2.1.

2.2 Signal Processing Scheme

Along with using different types of radar, there has been plenty of research on using and developing different signal processing techniques for analyzing the collected data from the radar. Most of these techniques involve performing a time-frequency analysis of the radar echoes. For example, short-time Fourier transform (STFT) has been extensively used in human gait analysis and motion pattern classification [2.1, 2.2, 2.6, 2.9, 2.20-2.28]. Other promising techniques include: inverse Radon transform [2.29], chirplet transform [2.1], Hilbert-Huang transform [2.30], MUSIC (Multiple Signal Classification) algorithm [2.31], wavelet transform [2.32], artificial neural network [2.33], Wigner-ville distribution (WVD) [2.34], complex probabilistic principal component analysis (CPPCA) [2.35], empirical mode decomposition (EMD) [2.36], Matrix Pencil method [2.37], ESPRIT (Estimation of Signal Parameter via Rotational Invariance Technique) [2.38] and so on. To understand the human complex motion such as human walking, multiple signal components corresponding to various target scattering parts need to be identified. While the aforementioned techniques can successfully extract some general information from this complex motion, they sometimes demonstrate insufficient capabilities in tracking the movement patterns of specific limbs. In order to overcome this issue, more sophisticated algorithms have been proposed in literature for separating components according to their scattering parts.

Ren et al. [2.10] utilized the short time state space method (ST-SSM) to extract micro-Doppler (μ-D) features for gait analysis using an ultra-wideband impulse Doppler radar. They were successful in extracting the torso and the leg features, but the detection of other weaker signals from body joints such as knees, ankles, toes, etc. via ST-SSM was inconsistent due to the low Doppler resolution used. In [2.19], the authors applied the S-method- (SM) based approach in conjunction with Viterbi algorithm to recognize the μ-D features from a rotating fan and human gait in indoor and outdoor environments. The SM was numerically very simple and requires just a few more operations than the standard Fourier transform based algorithm. This technique is simple but is suitable for mono-component signals or multi-component signals that are non-overlapping in the time-frequency plane. In the latter case, the separation of signals can be performed only when components significantly differ in magnitude. For a walking human subject, the authors performed the estimation of the dominant component: torso first. After they calculated the new time-frequency representation by removing the dominant component and repeating the process. Using the method, they were able to extract the torso and leg component, but the extraction of other signatures like the complete swing of the hands, knees for example was not possible as depicted in Figure 2.5. Du et al. [2.39] proposed a novel short-time iterative adaptive approach (ST-IAA) to form an improved spectrogram using a 2.4 GHz CW radar. Owing to its adaptive (data-dependent) property, ST-IAA has much higher frequency resolution and lower sidelobes than STFT and thus ST-IAA provides much more accurate spectrograms. Using this method, they were able to clearly identify the legs hands and torso from simulated data of a walking subject. However, the clear identification was

26
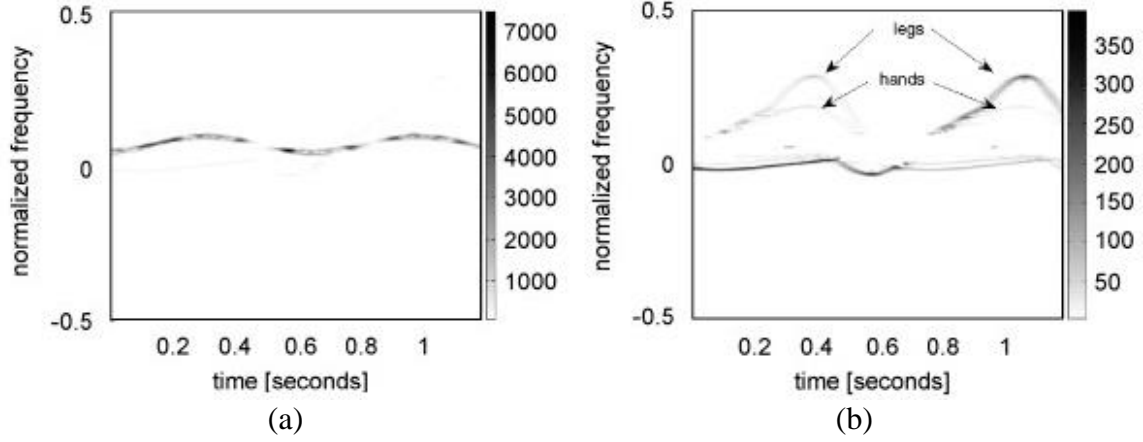
Figure 2.5: (a) Time–frequency representations using S-method and IF estimation for human data presented in [2.19]: (a) Signal showing all the micro-Doppler components with the main body having the most significant relative magnitude, (b) micro-Doppler components after removing the main body component showing legs and positive swing of the hands only.

not possible from the measured results as shown in Figure 2.6.

Using an 8-12 GHz ultra-wideband radar data with nonlinear least squares (NLS) and an expectation-maximization algorithm, Fogle et al. [2.40] were able to track the torso, hands and legs of multi-subjects walking simultaneously. Leveraging the fine range and Doppler resolution from the UWB radar, they were able to decompose the human signatures into the responses of constituent body parts. But, the experiment data was collected in a controlled environment and the ultrafine resolution (1.5 inch) was required to fully exploit the human signature information. Ding et al. [2.41] proposed a novel theoretical method to extract target micro-Doppler trajectories from CW radar echo with a modified high-order

27
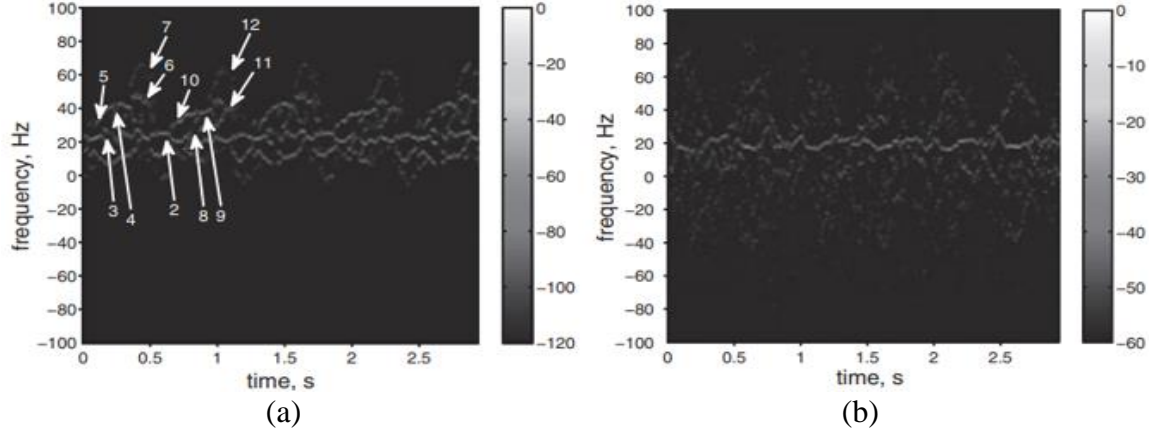
Figure 2.6: (a) Spectrograms of simulated human gait data extracted using ST-IAA approach reported in [2.39] showing identification of head (1), torso (2), upper and lower legs (5-7, 10-12), upper and lower arms (3-4, 8-9). (b) Identification from experimental data using the same approach.

ambiguity function and an adaptive de-noising technology. Through this method, they claimed that it is possible to accurately extract multiple components corresponding to different target scattering parts and their micro-Doppler trajectories in a time-varying low signal-to-noise ratio environment. In order to alleviate the weak component extraction interference from stronger ones, they used the CLEAN algorithm [2.42] which extracts the multiple components in the echo sequentially, instead of simultaneously, according to their energy scale. The authors presented the tracking results of torso, hands and legs of a walking subject from simulated CW data only reported in Figure 2.7.
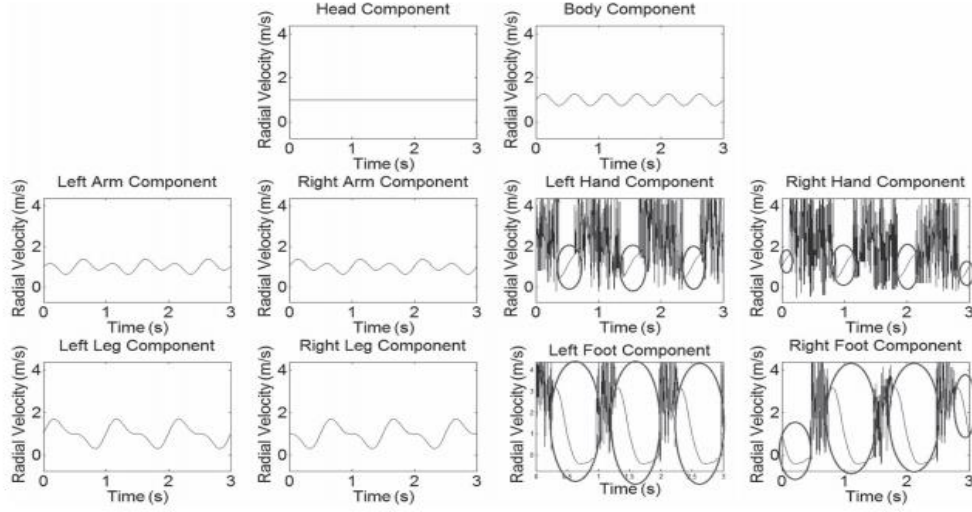
Figure 2.7: Estimation of different body part velocities of a walking subject from simulated CW radar data using the MHAF-CLEAN algorithm reported in [2.41].

In [2.43], the authors proposed the use of the combination of a human walking model and a motion capture model using infrared cameras as training data for classifier to decompose μ-D signatures of limbs from a walking human signature on real-time basis. Using the classifier and wideband simulated radar data, they were able to identify the trajectories of the torso, legs and hands of a walking subject. Raj et al. [2.44] used the simple steepest descent equations that enable the estimation of the optimal parameters for a given time-frequency distribution. The motion curves were estimated for each one-half cycle of walking and then concatenated to form the optimum motion curve estimates for slow and fast walking motions. Using this method, the authors were only able to identify the torso and the lower body parts of a walking human subject from simulated UWB radar data as depicted in Figure 2.8. In [2.45], Orovic et al. combined multi-window S-method and the
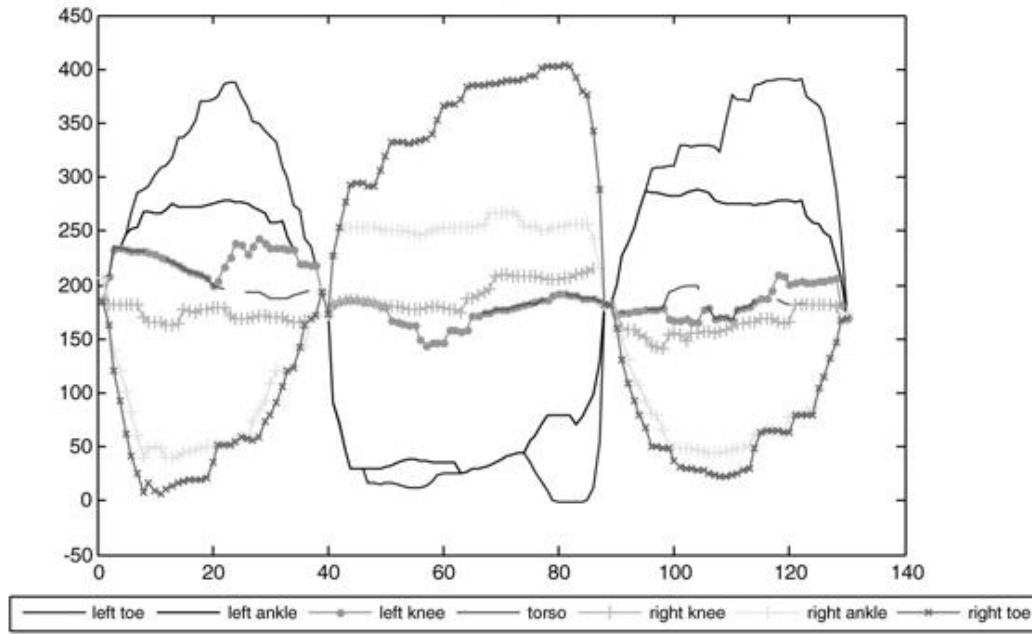
Figure 2.8: Motion curve extraction of the toes, ankles, knees and the torso of a walking subject using the simple steepest descent equations proposed in [2.44].

Hermite functions to obtain a highly concentrated time-frequency distribution to exhibit good motion extraction capabilities in the presence of noise while being computationally effective. However, analysis of Doppler radar data using the method for a walking human showed no distinction of hands and feet. Table 2.1 lists the above discussed software and hardware methods and summarizes their performance and limitations.

Table 2.1: Summary of existing research on radar systems for human motion sensing.

Ref	Radar Type	Signal Processing	Summary
[2.1] 2001	CW	STFT & chirplet transform	• One of the first attempts in gait analysis using radar techniques • 10.5 GHz CW radar • Combined time-frequency spectrogram only • No extraction of features
[2.2] 2005	CW	STFT	• Low-cost, low-power CW radar for remote sensor applications for security, perimeter protection, and border monitoring • Basic features like walking speed and stride length extraction only
[2.16] 2005	FMCW	-	• Use of 10.525 GHz FMCW radar to derive gait characteristics associated with carrying a bomb attached to the body • Tracking of thorax only
[2.32] 2007	SFCW	Wavelet	• 8.9-9.4 GHz SFCW signal with 10 MHz step size and 20 Hz PRF • Overall spectrogram only, no individual organ tracking
[2.6] 2008	CW	STFT + Notch Filter	• Use of notch filter to remove stationary clutter • No extraction of features
[2.19] 2008	SFCW	S-Method + Viterbi Algorithm	• 8.9–9.4 GHz SFCW signal with 10 MHz step frequency and 20 Hz frame rate • Analysis of human motion in high noise environment using computationally simple method • Extraction of torso and leg component of a walking subject, but extraction of the complete hand swing was not possible
[2.14] 2009	FMCW	IFFT	• 2-4 GHz FMCW signal at 0.4 ms PRF generated from a fast frequency swept Yttrium Iron Garnet (YIG) source • Pulse intensity fluctuated along the tracking • Tracking only, no feature extraction
[2.33] 2009	CW	Artificial Neural Network	• Use of eight 2.4 GHz radars for tracking • Walking trajectory and velocity determination only

31

Table 2.1 (continued from last page): Summary of existing research on radar systems for human motion sensing.

Ref	Radar Type	Signal Processing	Summary
[2.39] 2009	CW	Short Term Iterative Adaptive Approach	• Identifying the legs, hands and torso trajectories from simulated data of a walking subject • Difficult to identify organs from measured data
[2.44] 2010	CW	Gaussian G-Snake Model	• Identification of torso and lower body components only from simulated radar data
[2.18] 2011	SFCW	IFFT	• 1-2 GHz SFCW waveform with 2 MHz frequency step with four parallel PLLs and 11.1 Hz PRF • Motion sensing only, no tracking
[2.31] 2011	CW	STFT + MUSIC	• 5 GHz radar with 30 dBm transmitted power • Detecting maximum frequency of torso and legs only
[2.30] 2012	CW	STFT + Hilbert Huang Transform	• 10.48 GHz CW radar operating with calculated SNR of at least 32 dB • Tracking of torso and legs only with inconsistency in the tracked frequency
[2.34] 2012	CW	Wagner-Ville Decomposition	• 10.525 GHz radar • Walking speed, arms, and legs swinging cycle detection only
[2.40] 2012	UWB	Nonlinear Least Squares & Expectation Maximization Algorithm	• Tracking torso, hands and legs of multi-subjects walking simultaneously using a 8-12 GHz radar • Computationally expensive, experiments performed in controlled environment and high resolution radar required
[2.9] 2013	CW + UWB-IR	STFT	• 3 GHz CW and UWB-IR radar with 700 ps pulse with 3 GHz carrier for through-wall sensing, multiple-object detection, real-time target tracking • FPGA based equivalent time sampling data capture • Combined spectrogram, no extraction of features
[2.36] 2013	CW	Empirical Mode Decomposition	• Classification of different simulated motions • No features extracted

Table 2.1 (continued from last page): Summary of existing research on radar systems for human motion sensing.

Ref	Radar Type	Signal Processing	Summary
[2.5] 2014	CW	Extended Differentiate and Cross-Multiply	• 2.36 GHz radar with 25 dBm transmit power • Walking velocity extraction only
[2.15] 2014	CW + FMCW	STFT	• 160 MHz FMCW signal with 5.8 GHz carrier frequency for positioning and motion detection • Very expensive (7600$) signal generation scheme • Showed Doppler frequency shifts due to different movements but no feature extraction
[2.35] 2014	CW	Complex Probabilistic Principal Component Analysis	• Ka-Band (26.5-40 GHz) radar • Noise-robust classification of moving targets (human and vehicles) • No limb tracking
[2.41] 2014	CW	Modified High-order Ambiguity Function + CLEAN	• Torso, hands and legs of a walking subject from simulated CW data only
[2.11] 2017	CW + UWB-IR	-	• DWM1000 chip from Decawave as UWB-IR radar and a K-band Doppler radar InnoSenT IPS-154 operating at 24.125 GHz • Walking trajectory detection, no feature extraction
[2.17] 2017	FMCW	STFT	• 5.8 GHz carrier with 320 MHz chirp BW and 3.5 ms PRF • Detection of hand gesture motion in presence of multiple objects, no tracking of limb joints
[2.43] 2017	UWB	Machine Learning	• Real time classification using training data from combined motion-capture and Boulic model • Results shown from simulated data only
[2.4] 2018	CW	Cooperative Tracking-Localization Algorithm	• 5.8 GHz CW radar • One TX, 3 RX system for localizing moving object • No extraction of features

33

2.3 Software Defined Radars

In addition to the traditional implementation of radar systems, there has been significant research interest recently in software defined radars as compact and portable radar systems. The concept of a software-implemented radar first arose in the early 1970's through defense-related research and development [2.46], and later emerged into the public domain where the term SDR was officially coined [2.47]. There has been extensive research on radar systems based on SDR technology. Ralston et al. explored the potential of SDR technology in providing flexible and low-cost subsurface radar prototypes for the GPR community in [2.48]. In [2.49], Colorado et al. presented an approach for explosive-landmine detection by developing and integrating a GPR onboard an autonomous aerial drone. They used the USRP B210 hardware [2.50] and generated a 56 MHz wide raised cosine filter (RCF) pulse mixed with a 2 GHz carrier as their transmitted signal. An automotive radar system based on a custom designed SDR making use of a hybrid radar scheme of FMCW and pseudorandom (PN) code pulse techniques was presented in [2.51]. The FMCW measurement technique was deployed to obtain the range value of a target while the PN code pulse radar technique was used to determine the inter-vehicle radar information for communication purpose. The generation of the FMCW signal and the PN code was modulated by the DDS using the BPSK scheme. The FMCW signal had a bandwidth of 300 MHz starting at 24 GHz with 80 ms PRF and the PN modulated signal had a bandwidth up to 40 MHz. Costanzo et al. [2.52] used the USRP NI 2920 [2.53] to design a high resolution L-Band SDR system for target detection. They used a 25 MHz wide FMCW chirp mixed with a 1.8 GHz carrier signal to perform their experiments. In

[2.54], a custom designed SDR was utilized in FMCW and dual CW mode to conduct precise range measurements. The FMCW signal was a 75 MHz wide chirp signal carried by a 4 GHz carrier with 15 ms PRF and the dual CW signals were at 4 GHz and 4.01 GHz, all generated from a DDS.

In biomedical applications, Marimuthu et al. proposed an SDR system for medical imaging in [2.55]. They used the LMS6002D [2.56] SDR and programmed it to generate an SFCW signal from 1.2–2.14 GHz with a step frequency of 10 MHz and PRF of 608 ms. Park et al. used the OSU radar [2.57] for the study of human motion signature in [2.58]. They used a 500 MHz wide linear FM chirp mixed with 2.25 GHz and 8 GHz carriers and used them separately to generate Doppler spectrograms for a walking subject. Liu et al. [2.59] used the USRP N210 [2.60] SDR to operate as CW and FMCW radar to analyze micro-Doppler signatures. For CW, they used a single tone at 4.3 GHz and for the FMCW mode, they used a 10 MHz wide chirp at a center frequency of 4.3 GHz with 1.221 kHz PRF. A. R. Hunt [2.61] implemented a custom designed SDR to generate an SFCW waveform between 750 MHz to 2 GHz with 512 linearly spaced points and PRF of about 30 Hz. He used the radar imaging and through wall motion detection. Thus, we can see that SDRs have the potential to be utilized as compact, portable systems for non-contact gait analysis, but the wideband SDRs reported in literature typically has low PRF and narrow bandwidth.

2.4 Conclusion

From the above discussion, we can observe that there are some limitations in terms of both hardware and software in utilizing radar systems for motion analysis applications. From a hardware perspective, there are limitations like low pulse repetition frequency for UWB radars and SDRs, expensive signal generation scheme for SFCW and FMCW radars, high-performance ADC requirement for UWB-IR radars, DC offset problem, quadrature imbalance and so on. In terms of software, problems like inability to clearly extract individual features of the limbs, requirement of high range resolution radar data, and inability of extraction from measured data in a typical non-controlled environment and so on. Thus, there is a need for a system combining both hardware and software that can perform human motion analysis using simple, low-cost, portable radars and is capable of identifying different limb joints (like hands, legs and torso) from complex human motions in a typical non-controlled environment. The next chapter looks at the challenges for implementing such a system in more details.

CHAPTER THREE
IMPLEMENTATION CHALLENGES

In previous chapters, we introduced the concept of performing gait analysis using radar techniques. We discussed the different advantages of using the radars for non-contact method. But a thorough investigation of previous research in this field points out some challenges. We have observed that there are obstacles to address and overcome, i.e. both hardware and software problems/issues to make the radar technique a viable gait analysis tool. In this chapter, some of these challenges are discussed in detail.

3.1 Radar Pulse Repetition Frequency

Referring back to Figure 1.4, we observe that for a typical walking motion, the torso velocity represents the average walking velocity. The highest velocity components arise from the movement of the toes, which as an example for a walking velocity of 1 ms^{-1}, the maximum velocity for the toes are about 4.7 ms^{-1}. If the walking velocity changes, the velocity components of the toes will scale accordingly. Now, converting these velocity components into Doppler frequencies detected by a 2.45 GHz CW radar using Eq. 1.5, we see that the maximum Doppler frequency components are about 76 Hz as shown in Figure 3.1. But for a radar operating at 3.5 GHz, the same velocity would generate Doppler shift of about 110 Hz. Thus, for proper detection of the toe components, the radar Pulse Repetition Frequency (PRF) has to be at least twice the maximum Doppler frequency generated according to the motion and the operating frequency. Note that, having a PRF

$$f_d = \frac{2v_t f_c}{c}$$
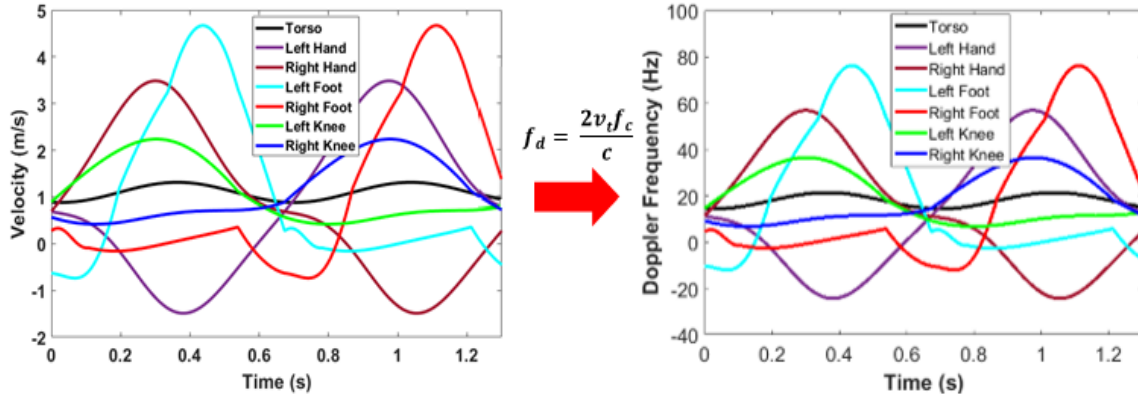
Figure 3.1: Converting the velocity components of different organs of a walking subject into Doppler frequencies with respect to a 2.45 GHz radar operating frequency.

higher than that does not necessarily mean that the radar will have better detection capability, rather it defines the minimum requirement for the Doppler frequency detection.

In order to demonstrate the minimum PRF requirement based on the Doppler frequency, we consider a scenario where a subject stands in front of a radar and creates a motion with gradual increasing velocity. This is achieved by swinging one hand back and forth slowly at first and then gradually increase the speed. The radar collects data at a PRF of 200 Hz and afterwards, we use the short-term Fourier transform (STFT) method to generate the time frequency spectrogram. STFT on the collected data is implemented in MATLAB using the built-in function *spectrogram* [3.1]. The function has the following form:

```
[s, f, t, ps] = spectrogram(x, window, noverlap, nfft, fs)
```

38

where each column of *s* contains an estimate of the short-term, time-localized frequency content of *x*. The parameter *window* divides the signal into segments and perform windowing and *noverlap* represents the number of sample overlaps between adjoining segments. *nfft* is the sampling point numbers to calculate the FFT and *fs* is the sampling rate. The function also returns a vector of normalized frequencies, *f'* and a vector of time instants, *t*, at which the spectrogram is computed and *ps* contains an estimate of the power spectral density (PSD) or the power spectrum of each segment.

Figure 3.2 shows the STFT results for the described scenario. We can immediately observe that the frequency range of the plot is ± 100, which is half of the PRF used. Initially when the motion is slow, we can see the full swing cycle of the hand. But as the velocity of the hand movement increases, the Doppler frequencies begin to go outside of the ± 100 Hz range and the spectrogram begins to collapse.
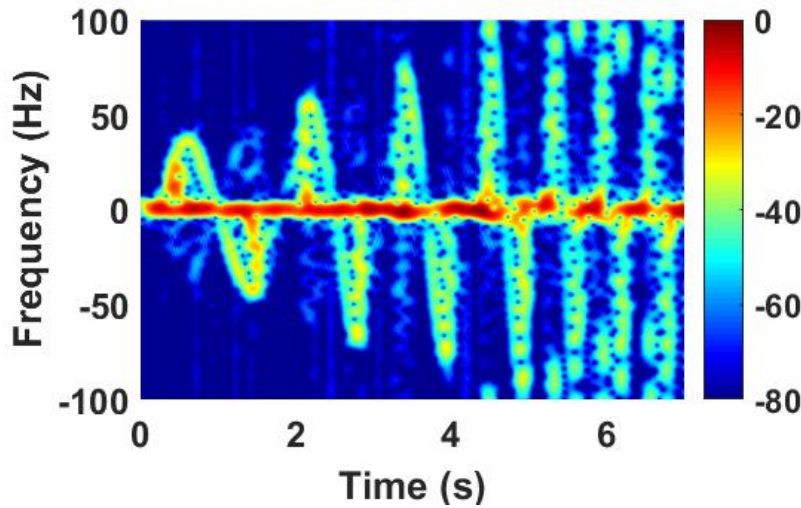
Figure 3.2: Demonstration of the minimum PRF requirement for motion sensing.

39

For a CW radar where a single tone is continuously transmitted, the PRF is simply the frequency at which the received data is sampled. For the UWB-IR where the pulses are sent intermittently, the PRF depends on the transmission, reception and the capturing period of the wideband pulse. Previous work in our group on gait analysis using UWB-IR [2.10] utilized a pulse circuit that would generate Gaussian pulses at a rate of 10 MHz, but had to use an equivalent time sampling scheme to capture this wideband pulse due to the expensive ADC requirements. In the equivalent time sampling scheme, a train of pulses with a period of 100 ns (1/10 MHz) is utilized, where the sampling trigger clock is set to have a period of (100 ns + Δt). The equivalent time sampling rate is decided by Δt and a fine resolution of 10 ps was achieved by using commercial delay line chip SY100EP196 from Micrel. Using the sub-sampling method, the system was configured to collect data from 8 elements of a phased array, each channel having a refresh rate of 75 Hz. Ren *et al*. [2.10] utilized data from only one of the channels with PRF of 75 Hz, which provided a Doppler resolution of only ±37.5. But, as Yazhou Wang suggested in his dissertation [3.2], the system can be adapted for higher PRF operation (up to 3 kHz). Still, there is no way around the complexities associated with the digitization of the data using the equivalent sampling method such as sophisticated FPGA implementation, clock jitter and drift, non-linearity of the delay line and so on [3.3].

Subsequently, in order to eliminate the sampling complexity of the UWB-IR while utilizing the benefits of the UWB radar, we can implement a SFCW radar system. The overview of the sampling scheme in SFCW radar is presented in Figure 3.3, where the frequency is stepped at an interval of *T* and at each frequency step, there would be some time required
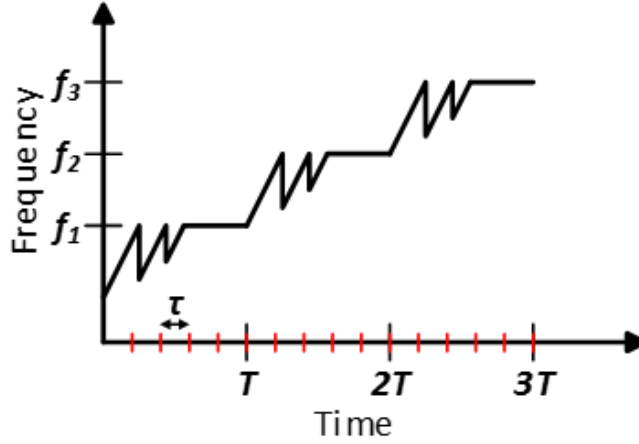
Figure 3.3: Sampling scheme overview of the SFCW system. Note that the frequency transition phase is exaggerated here.

for the signal to be locked before a stable sample could be captured. The ADC captures N number of samples ($N = 5$ in this case) at each step with a sampling interval of τ. Note that in this example, the first two samples of each frequency step are not reliable. Thus, the ADC sampling rate will be $1/\tau$ which is related to the dwell time (T) by the relation N/T.

In this case, the PRF of the radar is mainly dependent on the dwell time of each frequency. Previously in our group, there has been research on implementing single or multi-channel SFCW radar systems operating in 2-4 GHz band for vital signs detection [3.4, 3.5]. A direct digital synthesizer (DDS) driven phase locked loop (PLL) architecture was used to generate the stepped-frequency signals. The DDS generated the reference signals for the HMC833LP6GE PLL from Analog Device which was then multiplied by a programmable factor to produce the RF signal. Each time the reference signal was stepped, the PLL had

to lock to a new frequency according to the multiplier that was set. The step frequency, the start and stop frequency, the step duration could all be programmed through an FPGA that controlled the DDS. However, the minimum step duration was basically limited by the locking time of the PLL. Figure 3.4 shows a frame of a SFCW radar reported in [3.5] operating between 2-3 GHz with 20 MHz steps (a frame here is defined as the complete set of stepped frequencies between the pre-determined start and stop frequency that is repeatedly transmitted by the radar while the rate at which the frames are transmitted is the PRF of the SFCW radar). As shown in Figure 3.4, the PRF of the SFCW radar was only 20 Hz, which was adequate for vital signs detection, but certainly not suitable for gait analysis. The low PRF was the consequence of the slow locking speed of the PLLs that were utilized, thus an alternative PLL system is required now for use in motion analysis applications.
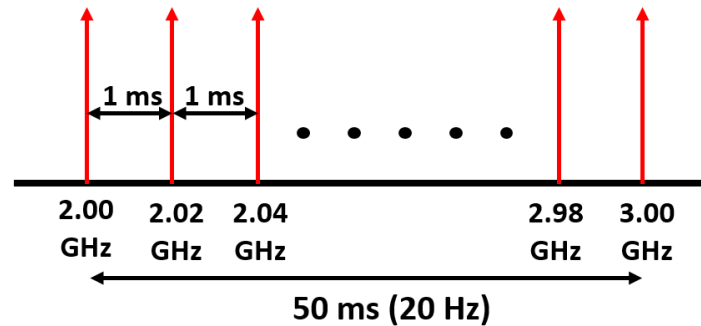
Figure 3.4: A frame of the SFCW system reported in [3.5], where the frequency is stepped from 2-3 GHz in 20 MHz steps. Each step duration is 1 ms to provide adequate locking time for the PLL (> 400 µs), in addition to having enough time to capture stable samples, which makes the PRF only 20 Hz.

42

If we target the detection of maximum 100 Hz Doppler frequency, it would require a radar with a 200 Hz PRF. If we consider a bandwidth of 1 GHz and a step frequency of 20 MHz, the dwell time per step comes out to be 100 µs. Thus, a PLL with frequency retuning time of around 50 µs is desired for this application. Note that, if we still consider capturing 5 samples per frequency step, the ADC sampling rate would be 50 kHz, which is still fairly low and easily achievable using low-cost ADCs. Table 3.1 lists some of the commercially available wideband PLLs suitable for frequency hopping that have frequency settling time less than 100 µs whereas Table 3.2 lists some ADC options for wideband radar operations.

Table 3.1: Commercially available wideband PLLs capable of fast frequency hopping.

Part Number	Manufacturer	Operating Range (MHz)	Min. Settling Time (µs)	Eval. + Interface Board Price
STW81200	STMicroelectronics	47-6000	> 80	-
LMX2572	Texas Instruments	12.5-6400	> 40	$ 310
ADF4196	Analog Device	400-6000	> 20	$ 190
ADF4152	Analog Device	500-5000	> 40	$ 150

Table 3.2: Commercially available ADCs for wideband radar applications.

Part Number	Manufacturer	Radar Type	Sampling Rate	No. of Bits	No. of Channels	Eval. + Int. Module Price
ADC32RF45	Texas Instruments	UWB-IR	3 GSPS	14	2	$ 3900
ADC12J4000	Texas Instruments	UWB-IR	4 GSPS	12	1	$ 3700
AD9208	Analog Device	UWB-IR	3 GSPS	14	2	$ 4800
USB-6003	National Instruments	SFCW or FMCW	100 kSPS	16	8	$ 551
USB-205	Measurement Computing	SFCW or FMCW	500 kSPS	12	8	$ 200

3.2 Phase Coherence

UWB radars provide range resolution capabilities due to its bandwidth which allows localization and multiple subject tracking abilities. The range information is actually obtained by the phases of the radar return echoes. Let us consider a SFCW radar that is transmitting frequencies f_1, f_2, …. f_N each with a step frequency of Δf. The transmitted signals for the first two frequencies can be written as:

$$T_1(t) = A_{t1} \cos(2\pi f_1 t + \theta_1) \; and \; T_2(t) = A_{t2} \cos(2\pi f_2 t + \theta_2) \qquad (3.1)$$

where A_{t1} and A_{t2} are the amplitudes and θ_1 and θ_2 are the initial phases of the transmitted signals for the two frequencies. The received signals from a target at a distance R from the radar for these two frequencies are:

$$R_{1R}(t) = A_{r1}\cos(2\pi f_1 t + \theta_1 - \varphi_1) \; and \; R_{2R}(t) = A_{r2}\cos(2\pi f_2 t + \theta_2 - \varphi_2) \quad (3.2)$$

where A_{r1} and A_{r2} are the amplitudes of the received signals and $\varphi_i = \frac{4\pi f_i R}{c}$ and c is the speed of light. If the values of θ_1 and θ_2 are defined phase angles compared to a reference, which is the case for coherent radars, the variation of the phases of the two received signals compared to the respective transmitted signals are φ_1 and φ_2 which are directly related to the distance travelled by the two waves. Thus the calculation of the phase difference between the two received signals allows the determination of the range R as:

$$R = \frac{c\Delta\varphi}{4\pi(f_2 - f_1)} = \frac{c\Delta\varphi}{4\pi\Delta f} \quad (3.3)$$

Note that the maximum unambiguous range of the radar is determined when $\Delta\varphi = 2\pi$ in Eq. 3.3.

$$R_{max} = \frac{c}{2\Delta f} \quad (3.4)$$

Thus, for $\Delta f = 20$ MHz, the maximum unambiguous range comes out to be 7.5 m.

In SFCW radars, multiple frequencies are transmitted repeatedly over multiple frames. In order to obtain a meaningful range information, it is imperative to have phase coherence across all frequencies in all frames where the only difference of phase between the transmitted and received signals is the outcome of the waves traveling through the medium. If this phase relationship is non-deterministic for a system, a calibration scheme has to be employed to achieve phase coherence.

3.3 Signal Processing Scheme

Although gait analysis using radar techniques provide a lot of advantages over the traditional gait analysis methods, one of the main drawbacks of using radar is the requirement for sophisticated signal processing algorithms to extract the desired features from the received data. In Chapter two, we discussed various algorithms reported in the literature to track specific body parts during motion and saw that even though some of the techniques were very promising, they all had their drawbacks. Some of the techniques proposed in the literature could not extract individual features of the limbs, while some of them were successful, but required wideband radar data. We know that UWB radars provide range resolution capability according to its bandwidth that allows them the capacity to track multiple subjects at the same time while providing localization capabilities. But they do add some complexity and additional cost to the system due to the required signal generation or data capture scheme. For applications where multi-subject tracking is not required, use of the much simpler and low-cost CW radar can be the more prudent solution. Thus, it is highly beneficial to have a signal processing algorithm that can extract the desired features from a complex motion using either CW or UWB radar data operating in typical non-controlled environment.

Previously, our group investigated the short-time state space method (ST-SSM) [2.10] with UWB data to perform gait analysis. We extracted the high resolution range profile from the collected data to show the real-time location of the subject or detect the walking path of a human target. We observed the range bins traversed by the subject and applied time-frequency analysis to these range bins to extract the micro-Doppler signatures of the target.

46

But since only one tone is available in a CW radar system, the previously used ST-SSM method does not provide meaningful estimates due the lack of range-information. Furthermore, the sinusoidal model that ST-SSM relies on to carry out the estimation is absent due to the heavy non-linearity of the CW data and the single tone does not offer a diversity in range bins from compressed domain in which the centered bin could be exploited to extract joint motions from the human limbs for short time intervals. It is not a failing only of ST-SSM on CW data, rather is a limitation of the 1-D spectral estimation approach that relies on a sinusoidal model to extract signal components from a target that exhibits motion and can be extracted within a single motion period. Because human is a complex target that depicts highly non-linear walking motion; the failing appears to be observed in other single 1-D techniques such as MUSIC, Matrix Pencil, ESPRIT, etc. for similar reasons.

3.4 Portable System

While the performance of a system is of a paramount interest, consideration should be also given towards making it ideally suited for use in any environment. The system has to be portable such that it gives the user some flexibility. Previous works reported in our group [2.10, 3.4, 3.5] utilized commercially available off-the-shelf components to implement the UWB-IR and SFCW systems. Figures 3.5 and 3.6 shows the photos of the two systems.
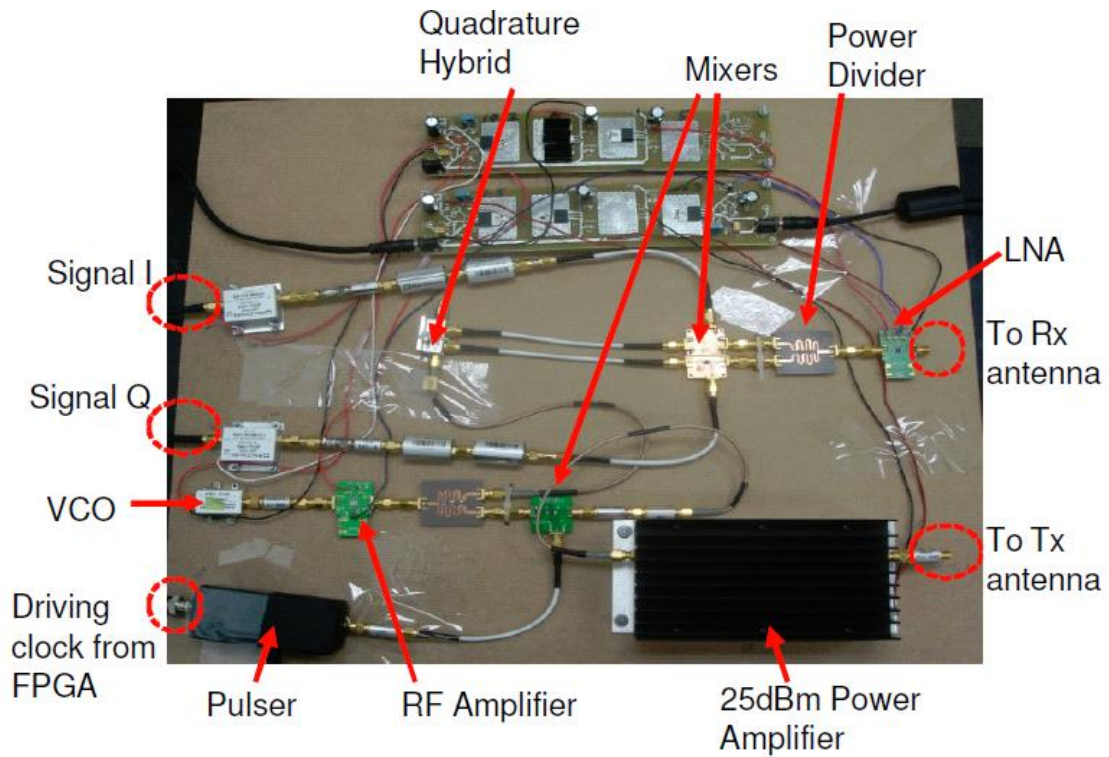
Figure 3.5: UWB-IR system in [2.10] showing the RF front-end and biasing components. The FPGA (not shown here) has two functions: driving the pulser to generate Gaussian pulses in 10 MHz intervals and capturing the I and Q signals using the equivalent time sampling method discussed before.
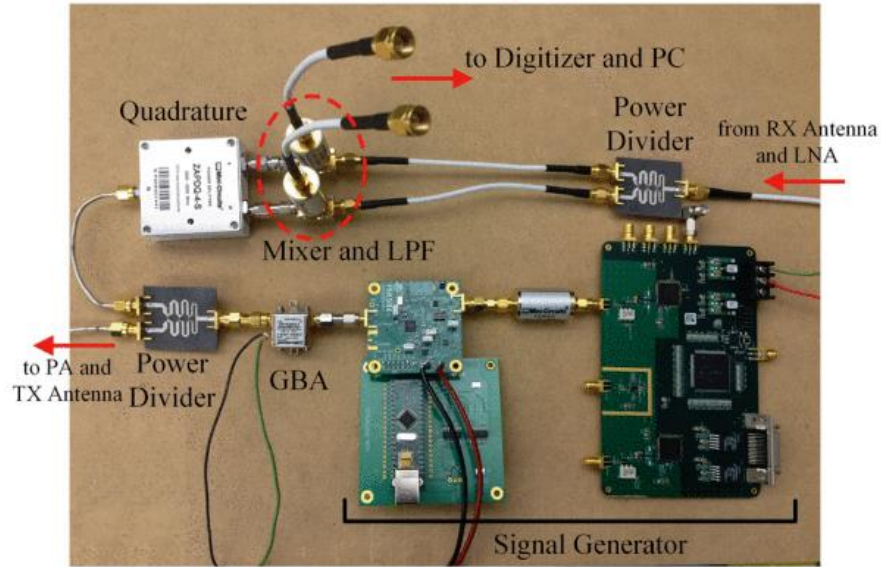
Figure 3.6: Photograph of the single channel SFCW radar system reported in [3.5].

As can be observed, both systems are very bulky and lack portability. In literature, there has been a lot of research on implementing integrated radar systems. These systems can be of two types: complete system on a single chip and individual ICs placed together on a single board in a hybrid system. Table 3.3 lists some of the work on integrated sub-10 GHz wideband radar systems used in biomedical applications reported in literature. As can be observed from the table, there is definite room for improvement on the receiver noise figure while implementing an application specific custom integrated radar system.

49

Table 3.3: Integrated wideband biomedical radar systems operating below 10 GHz.

Ref.	Process or Technique	Radar Type	Application	Freq. (GHz)	Tx Power (dBm)	Rx Power (dBm)	Rx NF (dB)	P_{DC} (W)
[3.6]	65nm CMOS	SFCW	Med. Imaging	2-16	-14	-29	5.4-8.4	0.2
[3.7]	65nm CMOS	Pulsed	Vital Signs	3-5	-	-	6-10*	0.02
[3.8]	180nm CMOS	Tunable CW	Vital Signs	Tunable 4.6-5.7	-6.1 to -12.5	-	-	0.04
[3.9]	130nm CMOS	Tunable CW Receiver	Vital Signs	Tunable 5.3-6.3	-	-28	2.2*	0.02
[3.10]	130nm SiGe BiCMOS	FMCW	-	8-9	-	-35	4.5*S	0.66
[3.11]	Hybrid	FMCW + CW	Localization & Vital Signs	5.64-5.96	8	-	-	-
[3.12]	Hybrid	SFCW + CW	Fall Detection	5.8-7	2	-	-	-

The other approach towards the implementation of portable radar systems is the use of commercially available software defined radars (SDR or SDRadar). SDRs have recently gained a lot of research interest due to their affordability, frequency tunability, small size, enhanced baseband signal handling capabilities and the lack of need for any external local oscillator signal sources, which lead to a compact overall radar platform and easily portable system. Table 3.4 lists a summary of SDRs utilized in different applications reported in literature. We can observe that the wideband SDRs reported in literature typically have very low PRF not suitable for human motion sensing applications apart from [2.58] and [2.59]. Although the SDR reported in [2.59] had a high PRF of 1.221 kHz, the transmitted FMCW chirp had a bandwidth of only 10 MHz which would result in a range resolution of

50

Table 3.4: Summary of wideband SDR techniques reported in literature.

[Ref.] Year	Part Number	Application	Type	Bandwidth (MHz)	PRF (Hz)	Price (USD)
[2.49] 2017	USRP B210	GPR	Pulse	56	-	1216
[2.51] 2007	Custom	Automotive	FMCW	300	12.5	-
[2.52] 2013	USRP NI 2920	Target Detection	FMCW	25	-	3182
[2.54] 2008	Custom	Range Measurement	FMCW + CW	75	66.67	-
[2.55] 2016	LMS6002D	Biomedical Imaging	SFCW	940 (with 10 MHz steps)	1.65	480
[2.58] 2012	Custom	Human Motion Sensing	Pulse	500	800	-
[2.59] 2014	USRP N210	Human Motion Sensing	FMCW + CW	10	1221	1943
[2.61] 2009	Custom	Imaging and Motion Detection	SFCW	1250 (with 2.4 MHz steps)	30	-

15 m. The radar used in [2.58] was a custom designed SDR [2.57] capable of providing excellent performance in terms of both bandwidth and PRF. But as shown in Figure 3.7, it is a very complex system and not easily portable. Thus, there is an opportunity of research on SDR techniques operating in CW mode and over wideband with fast enough PRF for performing gait analysis.

3.5 Original Contributions

Having discussed the challenges for developing a non-contact gait analysis system using radar technique, my major contributions towards the solution of these problems include:

1. In collaboration with my co-worker (Farnaz), we implemented a high PRF ultra-wideband radar capable of performing gait analysis. Faster PLL techniques were
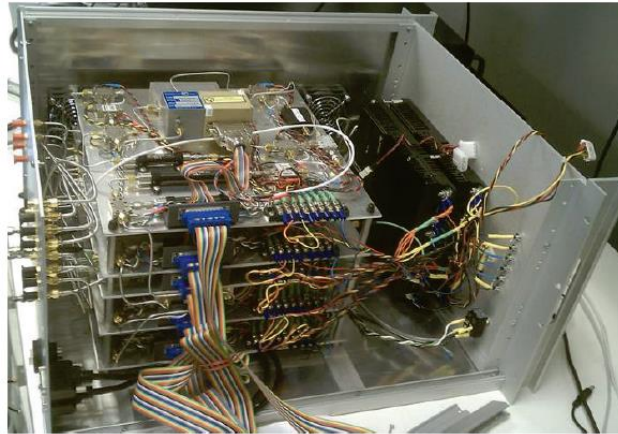
Figure 3.7: The SDR reported in [2.57] that was utilized in [2.58]. The five layers contains the hardware are stacked in a custom metal box.

investigated to generate stepped frequency signal swept over at least 1 GHz bandwidth with at least 200 Hz PRF.

2. Investigation of the feasibility of designing custom radar front-end integrated circuits. Design of wideband system components covering at least 1 GHz bandwidth such as gain block amplifier, LNA, mixer, power dividers for low RX noise, integrated and portable UWB radars.

3. Investigation of ultra-wideband and single tone software-defined radars (SDRs) for use in gait analysis with a target to achieve portability while keeping the implementation cost low. Implementation of a SDR based CW radar capable of performing gait analysis and a phase coherent SFCW radar.

4. Utilizing a signal processing technique called the 1-D block algorithm developed by our collaborators at MIT Lincoln Laboratory that is capable of individual organ tracking from complex human motion using either CW or UWB radar data.

5. Conducting gait analysis experiments in typical laboratory environment and extract the desired features using the hardware and software methods explored above. Comparing the experimental results to reference data obtained from motion modeling performed by Catholic University of America.

6. Investigation of other relevant applications utilizing the developed systems, like vital signs monitoring. Exploring the effect of switching the radar operating frequency for through barrier and higher sensitivity detection.

3.6 Conclusion

In this chapter, we discussed the main challenges of developing a non-contact system for gait analysis. The hardware challenges come in the form of implementing a fast PRF radar while maintaining the system portability. The obstacles in terms of the signal processing scheme come from the availability of an algorithm that can successfully extract the desired features from any type of radar (single-tone or wideband) operating in normal environment. We also defined the original contribution of this work that would address the challenges presented by this work. The subsequent chapters delve into the details of how we actually overcame these challenges to implement the system.

CHAPTER FOUR
HARDWARE IMPLEMENTATION: COMMERCIAL COMPONENTS

We discussed the various challenges: both in terms of hardware and software in developing a radar system that can successfully perform human motion analysis in the previous chapter. The hardware implementation can be approached from two perspectives: using commercial components and using custom designed circuits. This chapter sheds some light on how we tackled some of the challenges related to the hardware implementation using commercially available components.

4.1 Software Defined Radar

Our motivation in using the software defined radar (SDR) was its potential to be utilized as a flexible platform that can provide any CW tone within its operating range while having the capability to be used as a SFCW radar without using any external frequency generators. The proposed SDR for non-contact vital signs detection and gait analysis is mainly comprised of a hardware and software sub-system, as shown in Figure 4.1. The SDR hardware is based on the software-controlled RF Agile Transceiver AD9364 from Analog Devices. Previous reported works using commercially available wideband SDRs [2.49, 2.59] utilized systems based on the same series of ICs from Analog Device. But their overall system is very expensive, costing upwards of $1200. The SDR systems used in [2.52] and [2.55] both had a smaller operating frequency range, inferior receiver noise figure and narrower channel bandwidth compared to AD9364 as reported in Table 4.1.
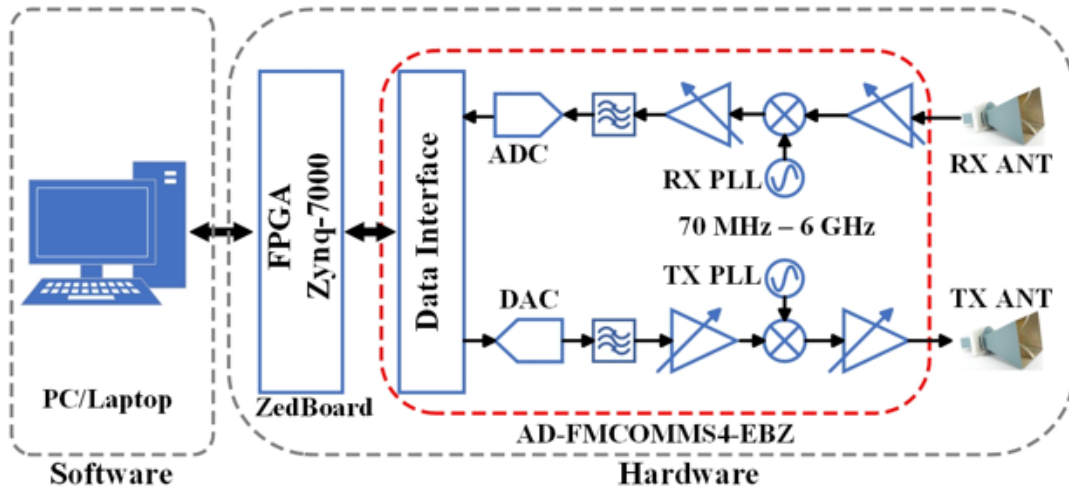
Figure 4.1: Block diagram of the proposed software-defined radar platform.

Table 4.1: Commercially available SDRs and associated parameters.

Part Number	Frequency Range (MHz)	Channel BW (MHz)	Noise Figure (dB)	Eval. & Int. Board Price (USD)
USRP B210	70-6000	56	2-3.8	1216
USRP NI 2920	50-2200	20	5-7	3182
LMS6002D	300-3800	28	3.5	480
USRP N210	DC-6000	50	5	1943
AD9364	70-6000	56	2-3.8	579

The hardware subsystem includes the software-controlled transceiver (AD9364), carrier board (ZedBoard), and two horn antennas for bi-static operation, chip transceiver details could be found in [4.1]. The software subsystem consists of a controlling code written in MATLAB, and the embedded software running on the associated carrier board.

The baseband signal generation, carrier frequency control, data storage and processing operations are performed in the software subsystem using a laptop/PC. The baseband signal and the control signals are sent to the SDRadar platform via Ethernet cable/USB, which are handled by a field-programmable gate array (FPGA) (Zynq-7000 All Programmable SoC on Zedboard) for interacting with the AD9364 transceiver hardware. The transceiver chip converts the baseband digital signal to analog and up-converts the frequency to the desired carrier frequency value for transmission using single sideband mixer. It also receives the reflected microwave signal, amplifies it via an LNA, down-converts it to baseband using direct conversion, and then digitizes it for storage. More details on the hardware and the software sub-systems are presented in the following sections:

4.1.1 Hardware

The software-controlled RF Agile Transceiver AD9364 from Analog Devices operates between frequencies 70 MHz to 6.0 GHz with channel bandwidths from less than 200 kHz to 56 MHz. The chip contains direct-conversion transceiver with larger than 17 dBm OIP3 for the transmitter and less than 3.8 dB noise figure for the receiver. The chip offers functionalities such as automatic gain control (AGC), quadrature and dc offset corrections,

and digital filtering. Having these compensation capabilities inside the chip significantly simplifies the operations of the digital baseband. The AD9364 chip is mounted on the commercially available evaluation board AD-FMCOMMS4-EBZ. The FMCOMMS4 board consists of four functional partitions – the transmit path, the receive path, clocking and power supply. The interaction with the transceiver board is performed using the ZedBoard carrier platform. The ZedBoard actually houses the Ethernet and USB interfaces, the Xilinx FPGA chip and other interfacing chipsets. The SPI signals and the control/monitoring pins coming from the AD9364 chip go directly to an FPGA Mezzanine Card (FMC) connector on the ZedBoard. Figure 4.2 shows a photograph of the hardware sub-system and Table 4.2 lists the performance specifications. The transceiver board houses the AD9364 chip, the RF connectors, a port for external reference signal. It also provides access to the different control/monitoring pins of the AD9364 chip.
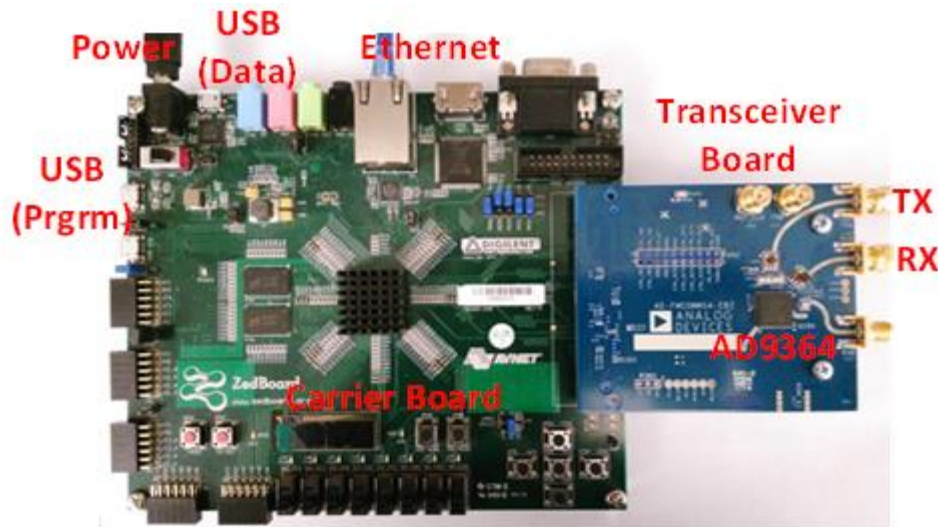
Figure 4.2: The SDR hardware platform.

Table 4.2: Performance specifications of the AD9364 software defined transceiver.

Parameter	Value
Frequency of Operation	70 MHz – 6 GHz
Channel Bandwidth	200 kHz – 56 MHz
Maximum TX Power	6.5 - 8 dBm
TX OIP3	> 17 dBm
RX Input Return Loss	-10 dB
TX Output Return Loss	- 10 dB
TX-RX Isolation	> 50 dB
RX Noise Figure	2 – 3.8 dB
RX IIP3	> -18 dBm
I-Q Gain Imbalance	0.2 %
I-Q Phase Imbalance	0.2 Degrees
Variable RX Gain	0-74 dB
ADC Resolution	12 Bits
ADC Sampling Rate	520.8 kHz – 61.44 MHz

As can be seen from the block diagram of the components inside the AD9364 chip presented in Figure 4.1, the transmitter and received frequencies are controlled by two different PLLs. Although it provides the capability to individually control the transmit and receive frequencies, it does pose a challenge in achieving phase coherence required for range detection. Figure 4.3 shows more detailed blocks of the frequency generation and PLL schemes inside the AD9364. A 40 MHz crystal oscillator from Epson is populated on the evaluation board that connects between the M12 and M11 pads shown in Figure 4.3. The on-chip digitally controlled oscillator (DCXO) allows the calibration of the frequency jitters of the crystal oscillator if required. The output of the DCXO drives the input of three

59
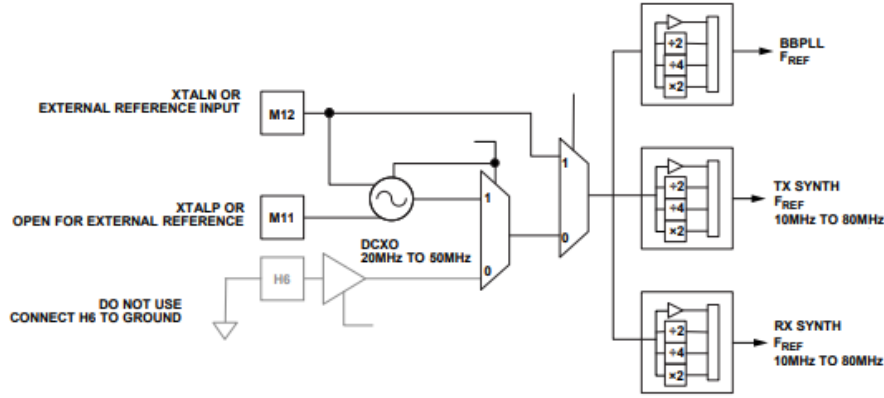
Figure 4.3: PLL reference block inside the AD9364 [4.2].

dividers which work as the reference frequencies of the baseband, transmitter and receiver PLLs. There is also an option to use external clocks instead of the on-board crystal oscillator, but still the PLLs are always individually driven by the three dividers. Based on the frequencies and the phases of the output of the dividers, the PLLs were locked.

For radar operation, we obviously want the transmit and receive frequencies to be identical, as well as having deterministic relationships between the phases. While the first condition is easily achievable, the second condition is not satisfied since there is no way to control the phases of the individual dividers. For CW operation, when we no range information is available, this non-deterministic phase relation is not really a problem. But for SFCW operation, where the reference divider settings are constantly changing due to the stepped frequencies, the phase difference between transmit and receive are randomly changing at every step. Thus, it is imperative to employ a calibration scheme to account for this non-deterministic phase relationship.

4.1.2 Software

The software sub-system establishes the connection between the transceiver and the FPGA hardware and the user. The software can be implemented either using MATLAB or through application program interface (API) libraries. The two methods are discussed in more details below:

4.1.2.1 <u>MATLAB</u>

The MATLAB interface is achieved through the use of Communications System Toolbox Support Package for Xilinx Zynq-Based Radio [4.3]. The support package contains the functions required to control the SDR hardware from the MATLAB/Simulink environment. The interaction between the hardware and software occurs through Ethernet cable connected between the host computer and the FPGA carrier board. It requires an SD memory card that is configured with the firmware of this support package. The firmware includes the embedded software and the FPGA programming files necessary for using the radio hardware as an I/O peripheral.

The MATLAB controller code creates the baseband signal by setting the Direct Digital Synthesizer (DDS) in the FPGA to transfer the baseband sinusoid to the RF card. The code also sets the sampling rate, the carrier frequency and the radio frame rate. After that, the Zynq-based Radio Transmitter and Receiver system circuits are initiated to operate the transceiver for a certain amount of time, and the data coming from the board is stored. Figure 4.4 shows a conceptual overview of the transmitting and receiving radio signals
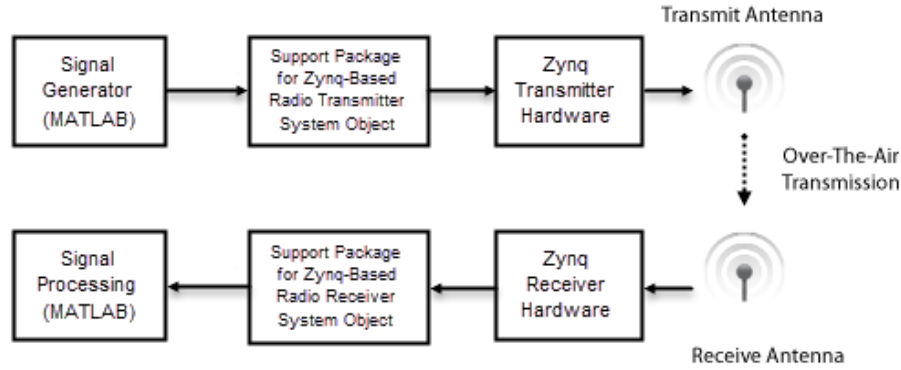
Figure 4.4: Conceptual overview of the SDR MATLAB interface [4.3].

with this support package and Appendix 1 contains the No-OS code and the associated MATLAB script that operates the radar as a SFCW radar. The MATLAB platform is convenient to use and has well-established examples to follow. But it does not provide access to all the functionalities of the chip and the evaluation board. In addition, since each operation/instruction for the transceiver has to be routed from the computer to the FPGA through Ethernet, the operating speed becomes slower compared to the case where everything is programmed inside the FPGA.

4.1.2.2 API: No-OS Platform

Analog Devices provides the API libraries [4.4] for controlling the AD936x generation of transceivers as open source for the users and those can be used on systems without running an operating system (OS). It is called the No-OS software where the libraries and the hardware descriptions are written in C. The carrier board specific FPGA files can be found in [4.5]; whereas the No-OS setup instructions are listed in [4.6]. We utilized the Xilinx

Software Development Kit (Xilinx SDK) version 2017.2 to customize the code and interface with the hardware. Once a code is written, it is directly written in the memory of the FPGA and code can be run to directly utilize the embedded ARM processing capabilities of the ZedBoard carrier, which makes the functionality faster. In addition, the use of the No-OS platform gives access to all the available functionalities of the AD9364 chip and along with the control pins on the evaluation board.

One of the important functionalities that No-OS allows is the use of fast lock options. Figure 4.5 shows the PLL synthesizer block diagram and the VCO divider configuration of the AD9364. Each time the PLL frequency of the AD9364 is retuned, the correct loop filter configuration, VCO calibration and the VCO divider values need to be determined and loaded in the respective registers. After the values are loaded, it takes some time for the frequency to lock to the desired frequency. The configuration value determination and VCO calibration typically takes up most of the time (typically about 600 µs) compared to the locking time (typically about 20 µs). The AD9364 offers a fast lock option, where the configuration values and VCO calibration settings (called profiles) for the desired frequencies are pre-determined and stored in registers inside the AD9364 chip. When the frequency has to be retuned, the correct register values are readily loaded and the retune time comes down to the locking time only. The fast lock allows up to 8 full TX and RX profiles of frequency configuration information to be stored in the chip memory for faster frequency changes. If more than 8 profiles need to be saved, the configuration bits can be saved in the base band processor or FPGA memory. The steps for using the fast lock option are listed below:
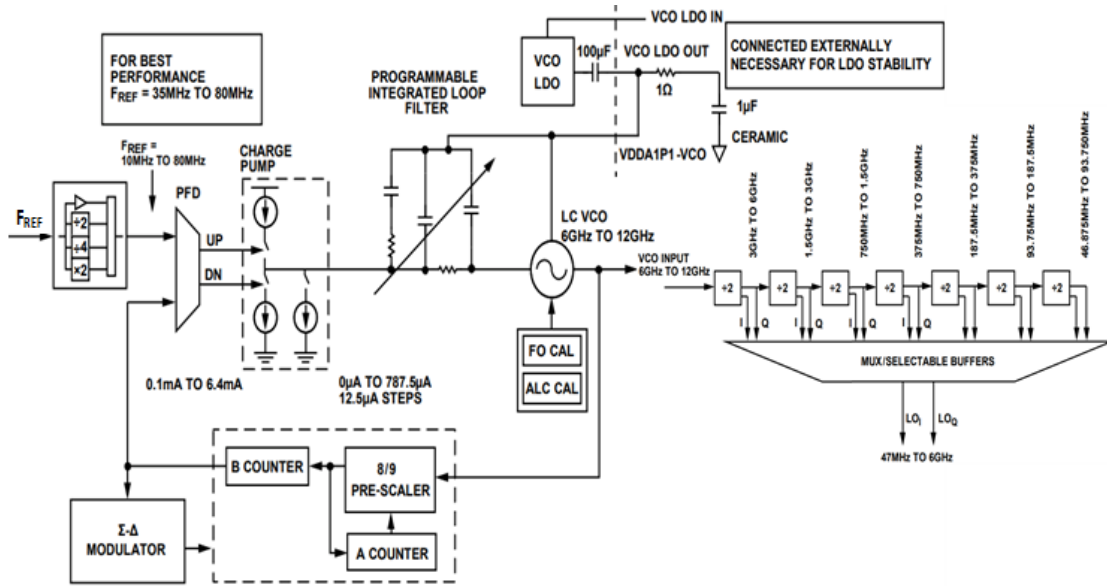
Figure 4.5: PLL Synthesizer with VCO divider block diagram [4.2]. The synthesizer consists of a phase frequency detector (PFD), a charge pump, programmable loop filter and a LC VCO that operates between 6-12 GHz. The VCO frequency is divided by a set of dividers to finally reach the operating frequency range of 47 MHz to 6 GHz. The TX and RX synthesizers are identical, but work independently. The F_{REF} comes from the digitally controlled oscillator as shown in Figure 4.3.

1. Before starting the actual sweep and collecting data, the profiles needs to be saved. Therefore the first step is to set the starting frequency in both the TX and RX PLLs.

2. The next step determines the appropriate register values and stores them in a profile. Available options for the profiles are 0-7. If only eight total frequencies are needed, then we would store the configurations sequentially in 8 different profiles. But if more frequencies are needed, it does not matter which profile is chosen, let us assume we chose profile 0 for TX and profile 2 for RX.

3. If only eight or less frequencies are needed, this step is not required. But for higher number of frequencies, save the register values stored in profile 0 and 2 in the FPGA memory. After saving, the profile 0 and 2 can be overwritten for other frequencies.

4. Go to all the other desired frequencies and repeat steps 1-3. After this step, the configurations for all the frequencies are already determined and saved.

5. To start the radar operation where TX, RX and data capture operations are performed, first the previously saved register values of the first frequency need to be loaded from the FPGA memory into profiles. Let us assume the TX and RX values are loaded in profile 1 and 3 respectively. If 8 or less frequencies are needed, this step is not required.

6. Recall the profiles 1 & 3 that would tune the TX and RX frequencies to the appropriate values. After this, the received data can be captured and stored for processing.

65

7. Load the register value of the next frequency and repeat steps 5 and 6 for all frequencies.

8. Continue steps 5-7 for the desired number of frames.

The actual codes for these steps that contain explanations of each step in comments are presented in the appendix section.

4.1.3 Phase Incoherence Calibration

As discussed in the previous chapter, for each frequency of the SFCW radar, the difference of phases of the TX and RX signals should only arise from the waves traveling in air. If the TX and RX local oscillator (LO) signals are generated from the same source, this is not really an issue. However, as discussed previously in this chapter, the TX and RX LOs inside the AD9364 are generated from two independent PLLs. Although the two frequencies can be locked, the phases cannot and they change randomly at every step. In order to mitigate this issue, we employ the following calibration technique presented in Figure 4.6:
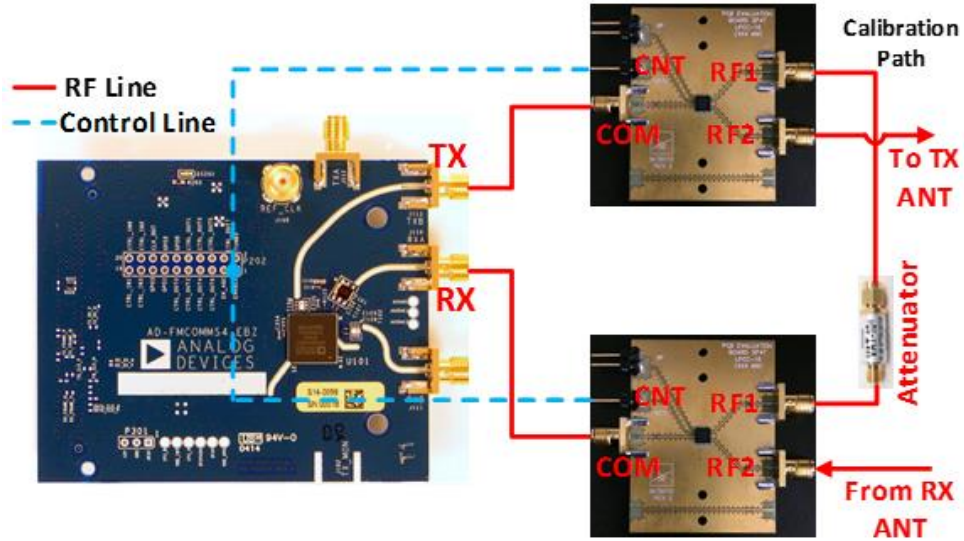
Figure 4.6: Phase incoherence calibration for the AD9364 SDR operating in SFCW mode.

For every frequency step, we obtain data from two paths: one a calibration path, the other the actual measurement path. The two paths are isolated by two high isolation SPDT switches SKY13286-359LF from Skyworks. The TX and RX ports from the SDR connect to the RF common ports of the two SPDTs as shown in Figure 4.6. RF1 ports of the two SPDTs are through connected using a coaxial cable and this path acts as the calibration path. An attenuator is also included in this path so that the signal going into the RX port through the calibration path is not higher than the 1 dB compression point of the receiver. The RF2 port of the SPDT connected to the TX port is connected to the TX antenna and the RF2 port of the other SPDT is connected to the RX antenna. This path, which includes the antennas, the medium of transmission and the target is the actual measurement path. After each frequency retune, the SPDTs are at first operated in the RFC-RF1 path. The control signal for the SPDTs are generated through one of the general purpose input output

(GPIO) pins available on the AD9364 evaluation board and the No-OS code running on the FPGA drives the GPIO signals. After saving data from the calibration path, the SPDTs are routed to the RFC-RF2 path and data is collected from the measurement path. This technique is repeated for each frequency step across all data frames, and finally the phase information from the calibration path is used to correct the phase incoherence in the measurement data.

In order to understand how the calibration is achieved, we go back to the transmitted signal equations presented in Eq. 3.1:

$$T_1(t) = A_{t1} \cos(2\pi f_1 t + \theta_{t1}) \tag{4.1}$$

Since the receiver signals are generated from a different source, they have different initial phases (θ_{r1} in this case):

$$R_{1R}(t) = A_{r1} \cos(2\pi f_1 t + \theta_{r1} - \varphi_1) \tag{4.2}$$

For the calibration path, φ_1 represents the fixed delay through the path depending on the frequency. The phase angle of the collected signal from this path for a certain frequency contains this fixed delay along with the difference of θ_{t1} and θ_{r1}. For the measurement path data, the initial phases for the TX and RX signals are still the same (θ_{t1} and θ_{r1}) since no frequency retune has occurred since collection of the calibration path data was done. This time though, φ_1 is not fixed, rather dependent on the motion of the target. We can now account for the added phase component introduced due to the random initial phases of the

TX and RX LOs in the measurement data calculated from the calibration path data. The

calibrated data from the mth frequency of the nth frame can be expressed as:

$$data_{calibrated}(m,n) = data_{meas}(m,n) \times \exp(-i \times \measuredangle(data_{cal}(m,n))) \quad (4.3)$$

where *data$_{meas}$(m,n)* and *data$_{cal}$(m,n)* are the data from the measurement and calibration

path respectively of the corresponding frequency and frame, $\measuredangle$ represents the angle

operator. Figure 4.7 shows a photograph of the complete system including the calibration

scheme.

In order to verify the performance of the calibration scheme, we setup a simple experiment

where the measurement path is through connected by a 3 m long coaxial cable. This closed
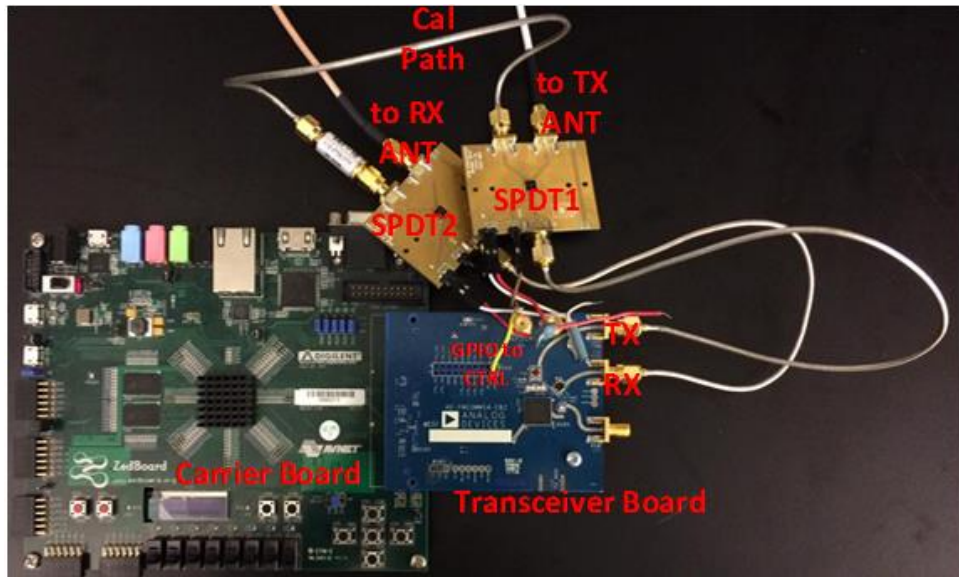
Figure 4.7: SDR system with phase coherence calibration scheme.

loop test demonstrates the effectiveness of the scheme without adding other non-ideal effects like the frequency dispersion effect in the antennas, reflections from unintended targets and so on. We programmed the SDR to step the frequency from 3 GHz to 4 GHz in 20 MHz steps and collect 100 frames. After collection of data, if we compress the pulse by performing an inverse Fourier transform (IFFT) operation across each frame, we should see a strong reflection coming from a particular range bin depending on the size of the cable. Looking at the phases of the measured signal for a particular frequency across all frames without doing the phase compensation, we see that the phase is varying randomly (Figure 4.8), which results in inconsistency in the range profile plot (Figure 4.9 (a)). But after calibration, the phase variation across frames for the same frequency becomes much more consistent which results in the expected range profile plot as shown in Figure 4.9 (b).
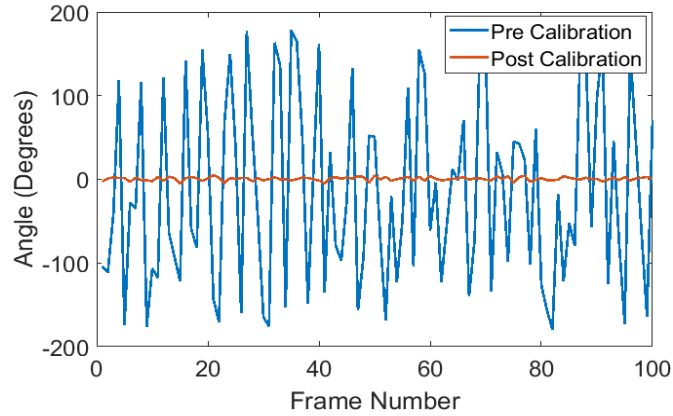
Figure 4.8: Phase of the captured down-converted signal for TX and RX LO at 3 GHz across 100 frames with or without calibration.

70
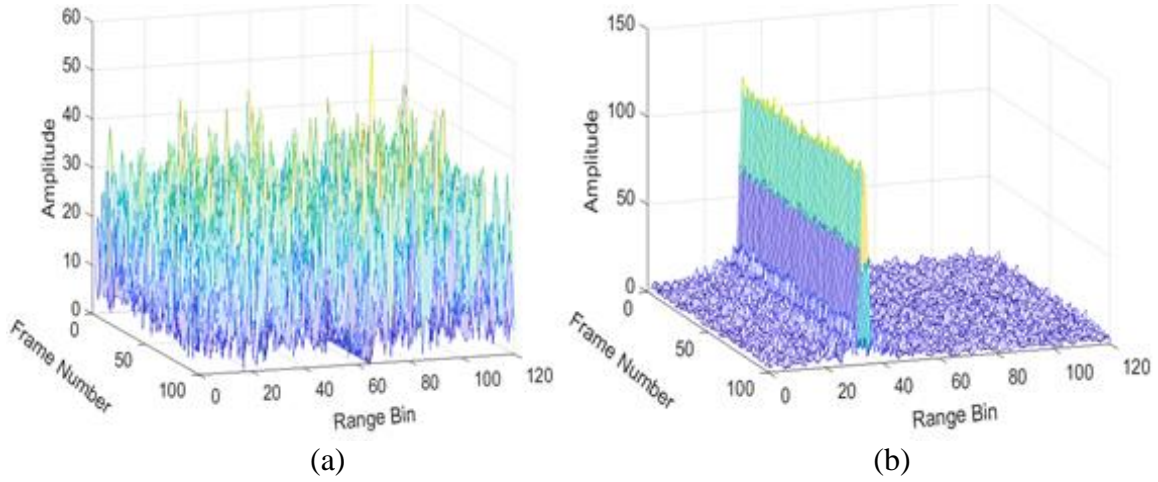
Figure 4.9: Range profile of the captured data (a) without calibration, (b) with calibration.

4.1.4 Limitation

Previously we talked about the VCO calibration and PLL lock time of the SDR which typically results in a frequency retune time of higher than 600 µs. We discussed that using the fastlock profiles we can pre-determine the VCO calibration settings and achieve the retune time around 20 µs. But the problem is the AD9364 chip allows saving only 8 fastlock settings at a time. We can save the settings for more frequencies in the FPGA memory using the 'fastlock save' function. But we would need to utilize the 'fastlock load' function to bring those settings to the AD9364 chip which adds delay in the frequency retuning. And considering we have to perform the loading operation for the TX and RX PLLs separately, it adds a total delay of about 800 µs. Thus, considering the PLL lock time, switching time for calibration and ADC capture time, the total dwell time at each frequency comes out to be about 870 µs. Table 4.3 shows the division of time across the different operations that take place during each frequency dwell.

71

Table 4.3: Time division in the SDR across operations during each frequency dwell.

Operation	VCO Cal.	PLL Lock	Calibration Switching	ADC Capture
Time (µs)	760	40	40	30

Although the achieved dwell time is smaller than the dwell time of our existing PLL based SFCW signal generator (1 ms), it is higher than our targeted frequency retune time of 100 µs and is not adequate to perform gait analysis. We could have utilized only 8 frequency steps to circumvent the fastlock loading problem, which would allow us a frequency retune time of less than 100 µs. But using only 8 frequencies in 20 MHz steps would only allow 140 MHz of bandwidth which would provide a range resolution greater than 1 m with theoretical maximum detectable range of 7.5 m. The use of the more expensive SDR systems like the USRP N210 could provide retune time of about 400 µs according to their technical support engineer, but that would still not be fast enough to detect the motions from a person walking at 1 ms^{-1}. But, we can still use the CW mode of our SDR system to perform gait analysis while utilizing the SFCW mode for other applications like detecting vital signs.

4.2 Fast Switching PLL

Previous work in our group on SFCW system utilized the HMC833LP6GE PLL from Analog Device [4.7] for the stepped frequency generation. The PLL was a fractional multiplier PLL with integrated VCO covering an RF bandwidth of 25-6000 MHz. While it

provided excellent performance in terms of phase noise (less than -105 dBc/Hz at 100 kHz offset) and wide operating frequency, it was not suitable for fast stepping/sweeping operation. The minimum frequency retune time that we could achieve using the PLL was about 400 µs and although that was sufficient for vital signs detection, it is not acceptable for performing gait analysis.

The ADF4152HV PLL from Analog Device [4.8] appeared as a very attractive solution to this problem. It is a 5 GHz fractional/integer multiplier PLL synthesizer with lock times below 50 µs. Although it does not come with an integrated VCO, the evaluation board carries the footprint to place an external VCO on the board. Unlike the evaluation board of the HMC833LP6GE, the ADF4152HV evaluation board contains the USB interface, so no additional UWB interface boards are required for configuring the board. In addition, the cost of the evaluation board is also cheaper compared to the previous PLL ($150 vs $369) and the other fast PLLs listed in Table 3.1. But we did have to make some modifications to the evaluation board to make it suitable for our application. The modifications are discussed below:

4.2.1 Replacement of VCO

The VCO that comes by default with the evaluation board is a 1-2 GHz chip DCYS100200-12 from Synergy Microwave Corporation [4.9]. It provides excellent phase noise characteristics (-105 dBc/Hz at 10 kHz offset) and needs a supply voltage of 12 V and a tuning voltage range of 0.5-28 V. Since our intended range of operation is 2-4 GHz, we needed to choose a different VCO. We chose another Synergy chip DCYS200400-5 [4.10]

73

which covers the 2-4 GHz range and has the same PCB footprint and pin configuration. This chip has a phase noise of -90 dBc/Hz at 10 kHz offset due to its higher frequency of operation and larger operating range. The tuning voltage range of this chip is 0.5-16 V and the required supply voltage is 5 V. The tuning voltage is controlled by the on-chip charge pump inside the ADF4152HV PLL and the range is defined by the supply voltage for the charge pump. The supply voltage to the VCO and the charge pump are both generated from on-board adjustable voltage regulators. Thus, after swapping the VCO chips, the voltage regulators were adjusted to get the correct supply voltages.

4.2.2 Reference Signal Routing

As mentioned earlier, we use a DDS driven PLL structure where the stepped reference signal generated by the DDS is multiplied by the PLL to get the RF output. The evaluation board actually has a fixed reference signal provided by an on-board 25 MHz crystal oscillator (Y1 in Figure 4.10). The board does provide a port (REFIN) for using an external reference signal which in our case comes from one of the channels of the two-channel DDS board. Thus, we just had to make simple modifications to the evaluation board to route the reference signal from the REFIN port and take R100 off to cut the supply voltage to the crystal oscillator and R101 off to disconnect that routing path.
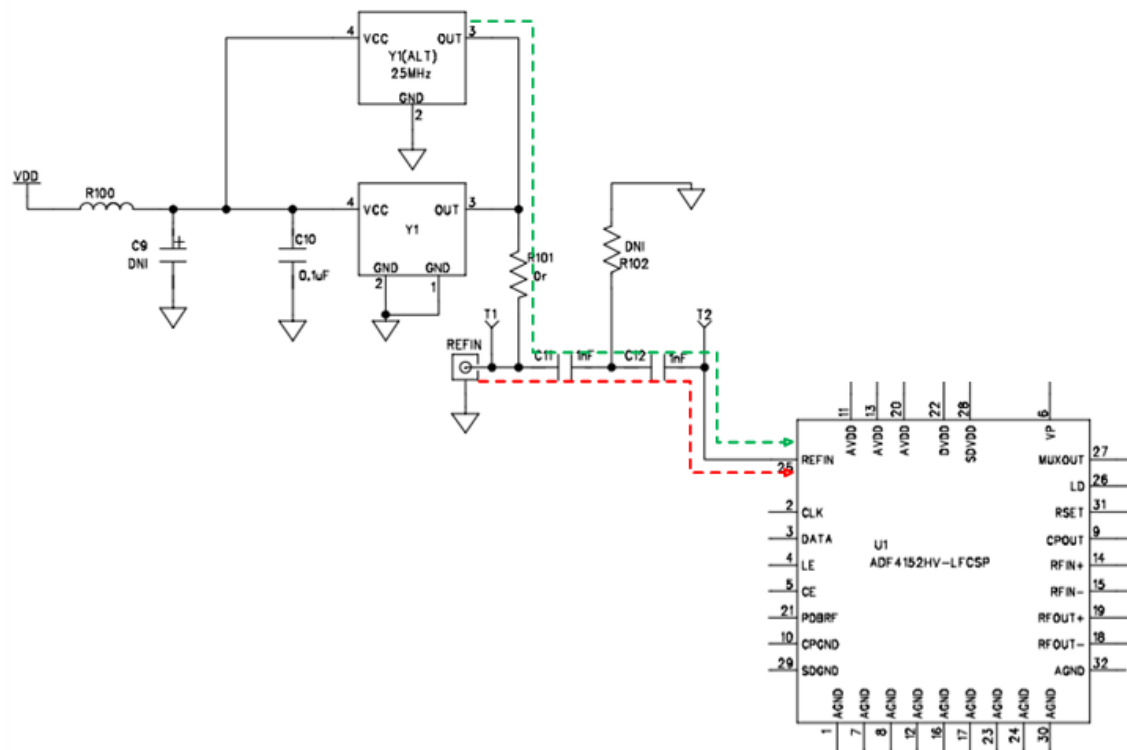
Figure 4.10: Reference signal routing in the PLL evaluation board. Green path shows the

default path and red denotes the intended path.

4.2.3 PLL Loop Filter Configuration

Our goal is to achieve a step frequency dwell time of 100 μs and PLL lock time of around 50 μs. Although the ADF4152HV is capable of achieving similar times, it does not mean that it can do so for any configuration. The lock time and stability performance of the PLL is dependent on the loop filter configuration. Figure 4.11 depicts the basic PLL model showing its components inside the feedback loop.

The feedback loop consists of a phase detector, a charge pump, a loop filter, a VCO and a frequency divider. The feedback system forces the error signal to approach zero to maintain phase and frequency lock. The error signal is detected by the phase detector which drives the charge pump that generates the tuning voltage of the VCO. The higher frequency contents of the error signal are filtered by the loop filter which is basically a low pass filter.
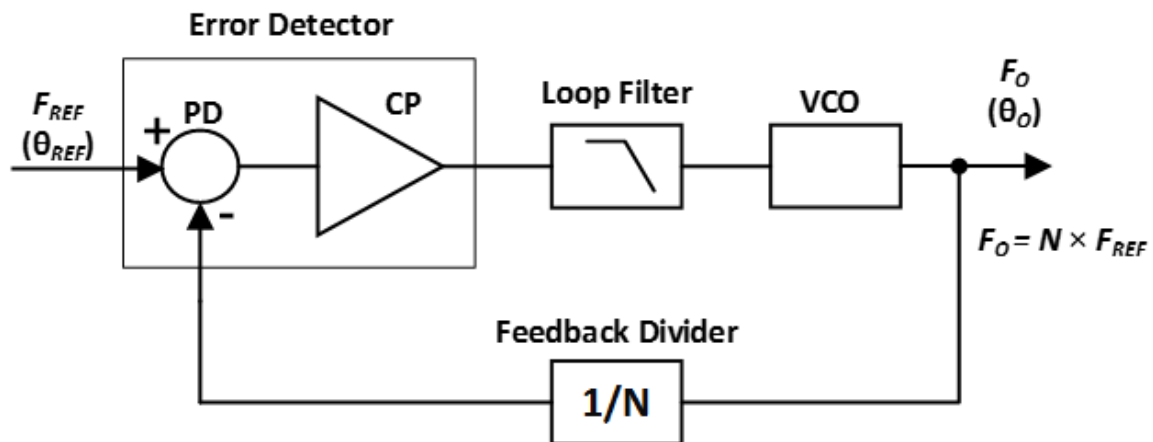
Figure 4.11: Basic PLL block diagram where PD and CP represent the phase detector and charge pump respectively.

There is a tradeoff between the lock time and stability that depends on the loop bandwidth of the feedback path which is set by the cutoff frequency of the loop filter. A larger loop bandwidth helps in settling to the lock condition faster, but makes the stability of the system worse while a small loop bandwidth makes the lock time longer. For best lock time performance, we want to maximize the loop filter bandwidth while keeping the phase margin of the system close to 48 degrees [4.11, 4.12].

In order to obtain an optimum loop filter configuration, we utilized the ADIsimPLL software from Analog Device [4.13]. The software helps in designing the loop filter by modifying parameters such as loop bandwidth, phase margin, VCO sensitivity, and component values and allows the user to easily optimize the design for specific requirements. Using the software, we can construct a PLL system by specifying the frequency requirements of the PLL, and then choosing from a library of PLL chips, library or custom VCO, and a loop filter from a range of topologies. When we run the analysis on the software for the PLL with the new VCO model and the evaluation board's default loop filter settings, we see that the loop bandwidth is 18.3 kHz, phase margin is 45.4° and the lock time is close to 2 ms as shown in Figure 4.12. But after changing the loop filter configuration, we were able to get the loop bandwidth to 150 kHz with phase margin of 48.3° which helped in achieving a lock time of about 50 µs as shown in Figure 4.13. We then implemented the new loop filter on the evaluation board to complete the PLL system with a fast switching capability.
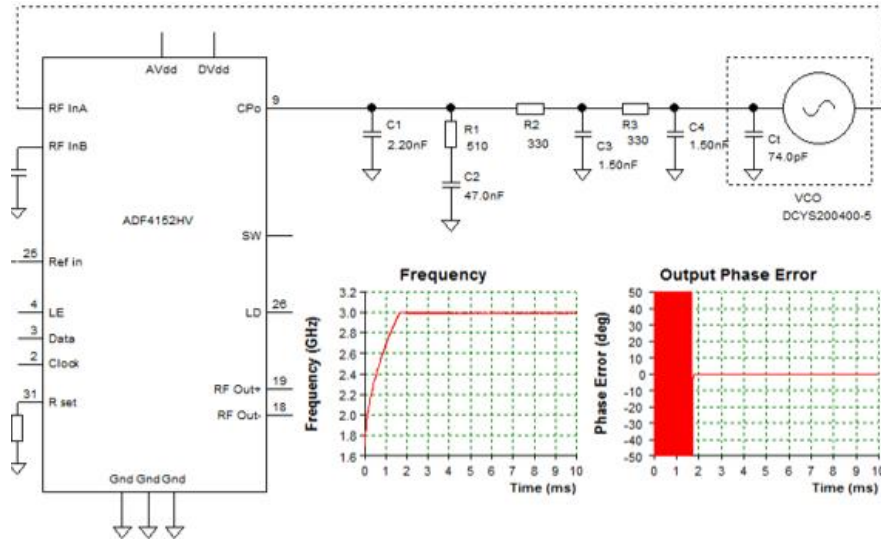
Figure: 4.12: PLL loop schematic with original loop filter configuration showing frequency and phase lock time.
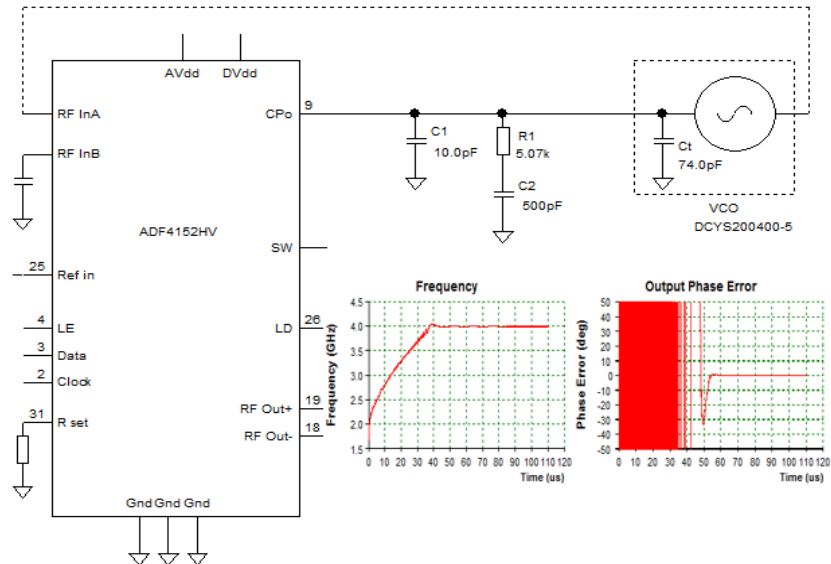
Figure: 4.13: PLL loop schematic with new loop filter configuration showing frequency and phase lock time.

78

We then utilize the USB-205 multi-channel 12-bit ADC from Measurement Computing and collect 5 samples at each frequency step at 20 µs intervals (50 kHz sampling rate). Each 12-bit sample is saved to the computer through USB immediately before the next sampling is done, thus saving additional data transfer time required by the previously reported equivalent time sampling method [2.9, 2.10]. After the capture is complete, we use the proprietary decimation algorithm from our collaborator MaXentric Technologies to choose the correct frequency sample from each step when the PLL is settled at that frequency and perform subsequent signal processing. The comparison of a frame capture duration of this SFCW system and the previous UWB-IR system is presented in Table 4.4. The block diagram of the complete SFCW system is presented in Figure 4.14 whereas Table 4.5 compares the performance of our PLL based and SDR radar systems with different SFCW radar systems reported in literature.

Table 4.4: Timing comparison of the SFCW system and previous UWB-IR system.

Parameter	This Work (SFCW)	UWB-IR [2.9, 2.10]
Pulse Rate	200 Hz	10 MHz
Samples per Pulse	5 (samples/freq.) × 50 (freq./pulse) = 250	100e9 (sample/sec) × 100 nsec/pulse × 8 (channel) = 80000
Pulse Sampling Time	250 (sample/pulse) / 50,000 (sample/sec) = 5 msec	80000 (sample/pulse) / 150e6 (sample/sec) = 0.53 msec
Data Size per Pulse	250 (sample/pulse) × 12 (bits/sample) × 2 (I & Q) = 750 Byte	80000 (sample/pulse) × 16 (bits/sample) × 2 (I & Q) = 320000 Byte
Data Transfer Time	-	320000 (Byte) / 25 (MB/sec: USB 2.0 speed)= 12.8 msec
PRF	1/(5 msec) = 200 Hz	1/(.53 + 12.8 msec) = 75 Hz*

* This is for 8 channels, but for one channel PRF would be 75 × 8 = 600 Hz.
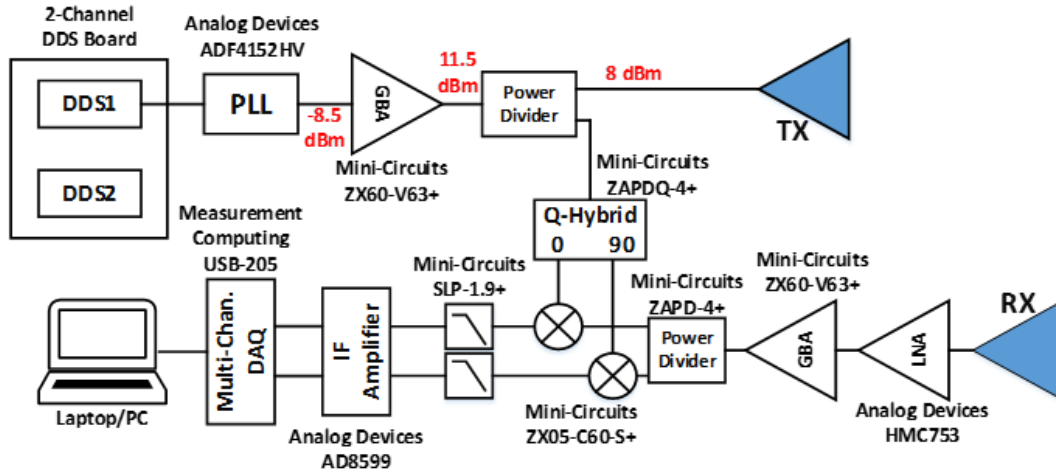
Figure 4.14: Block diagram of the implemented radar system with the power levels in the TX chain labeled.

Table 4.5: Performance comparison of the proposed SFCW radar systems implemented utilizing SDR and PLL with existing works in literature.

[Ref]	Frequency Range (GHz)	Step Freq. (MHz)	No. of Channels	PRF (Hz)	RX Noise Fig. (dB)	TX Power (dBm)
[2.18]	1.0-2.0	2	4	11.1	-	-
[2.19]	8.9-9.4	10	1	20	-	-
[2.55]	1.2-2.14	10	1	1.65	3.5	-20
[2.61]	0.75-2.0	2.4	1	30	-	17
[4.14]	0.3-1.3	5	1	4	-	-
[3.12]	6.0-7.0	25	1	500	-	2
[3.5]	2.0-3.0	20	1	20	2	8
This work (SDR)	2.0-3.0	20	1	23	2.5	12
This work (PLL)	2.0-3.0	20	1	200	1.8	8

4.3 Conclusion

This chapter discussed the hardware implementation for the gait analysis radar system using commercially available components. We discussed the implementation of a software defined radar that can function in both CW and SFCW mode using a transceiver chip from Analog Device. After investigation, we found that the target PRF of 200 Hz was not achievable from the SDR-SFCW system. But we could still utilize the CW mode for gait analysis while using the SFCW mode for detecting vital signs. We then implemented the fast switching SFCW signal generator using a new PLL and making modifications to the evaluation board in the VCO, the loop filter and reference signal routing scheme. Using the modified signal generator, we were able to achieve our targeted PRF of 200 Hz which would be suitable for the detection of our targeted maximum Doppler frequency of $\pm$ 100 Hz. But the PLL based SFCW system still remains bulky due to the use of discrete radar front-end components. In the next chapter, we will highlight the implementation of the radar front-end using custom designed integrated circuits.

CHAPTER FIVE

HARDWARE IMPLEMENTATION: CUSTOM FRONT-END IC

The discussions on the previous chapter shows the implementation of a fast switching PLL that will act as the signal generator of a SFCW radar system. For the radar front-end itself, we can use the commercial discrete components to implement the system as previously reported from our group [3.4, 3.5, 5.1]. These previous works demonstrated excellent performance for vital signs detection, target identification and ranging from the SFCW radar implemented using discrete components. But one of the main problems of those systems was their lack of portability due to their bulky sizes. Benefiting from the rapid developments of semiconductor technologies, significant advancements in hardware miniaturization have taken place in recent years. Advanced CMOS/SiGe/GaN/GaAs technologies, and systems have enabled the minimization of tracking and localization radars and significantly enhanced their portability while broadening their operation frequency range [5.2, 5.3]. In this research, efforts have been invested to the implementation of a compact radar system by designing the radar front-end components as integrated circuits (ICs), which should be considered as the first step in developing a full radar system on chip.

5.1 Fabrication Process

CMOS (Complementary Metal-Oxide-Semiconductor) process technologies have been ubiquitous in commercial and research applications due to their well-established

fabrication facilities, lower cost process and low-power operation capabilities. But they do suffer from drawbacks such as higher leakage, higher noise and limitations in high-power handling capabilities due to lower breakdown voltages. HBTs (Hetero-Junction Bipolar Transistors), on the other hand, offer low base resistance and low forward transit time due to much higher base doping and thus offer higher cut-off frequency. They also demonstrate very low collector to substrate capacitance due to the semi-insulating substrate. HEMTs (High Electron Mobility Transistor) also exhibit excellent performance in terms of minimal source resistance and high output resistance, high gain-bandwidth product due to the high electron velocity in large electric fields, high transconductance due to small gate to channel separation and very low noise figure. For all these advantages, HBTs and HEMTs are being regularly used in designing a multitude of components in commercial, military and consumer applications despite the expensiveness of these processes and that is what we have chosen as our fabrication process in this research. The radar front-end components consist of gain block amplifier, mixer, power divider and a low noise amplifier. All the components except for the LNA was designed using Qorvo's internal proprietary HBT process whereas the LNA was designed using Qorvo's in-house HEMT process.

5.2 Design Details

The block diagram of the implemented system is given in Figure 5.1. Each component was designed to cover at least the 3-4 GHz band which is the intended frequency of operation of the radar system. After fabrication, the bare dies are wirebonded on individual evaluation boards fabricated on a 31-mil thick RO4350B substrate for the purpose of testing. Other
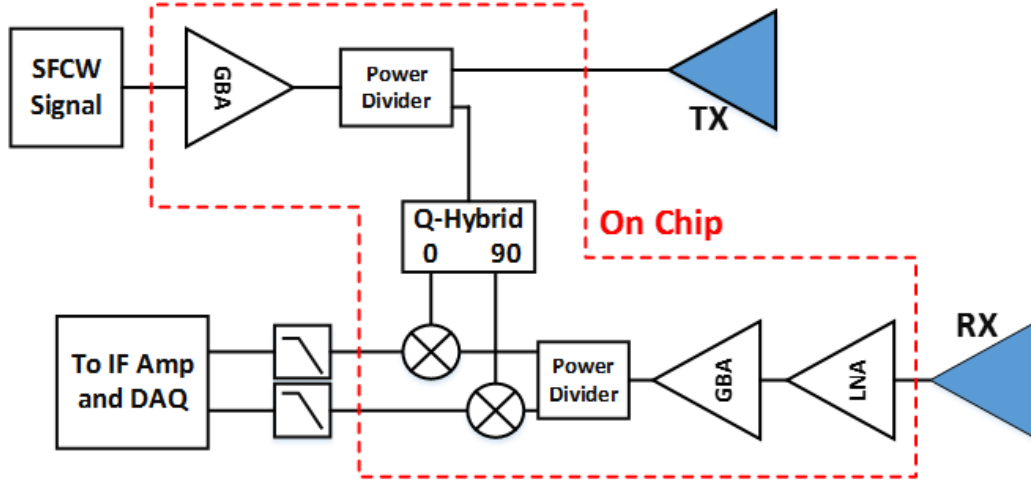
Figure 5.1: Block diagram of the proposed hybrid SFCW radar system showing the on chip components.

parts, such as the RF choke inductors and DC coupling capacitors for the amplifiers and the lumped components for the IF filter for the mixers were also placed on the respective evaluation boards. In this section, the design details of each individual components are presented.

5.2.1 Gain Block Amplifier

The Gain Block Amplifier is a two-stage CE-CE amplifier designed using the HBT process to operate within the 2-4 GHz band. Inter-stage matching network along with input and output matching are utilized to achieve good matching and flat gain performance. The output stage is divided into four transistors to ensure the current through each transistor was within the allowed limit. Extensive EM analysis is performed using ADS Momentum RF to establish proper functionality. After fabrication, the amplifier demonstrated 17 dB

gain with ±1 dB variation across the band when mounted on the evaluation board with the associated biasing components. The DC power consumption of the amplifier is about 0.4 W with a minimum of +15.5 dBm output 1dB compression point. The schematic and the fabricated die photos are shown in Figure 5.2 whereas the simulated and measured S-parameters of the amplifier are shown in Figure 5.3.

5.2.2 Power Dividers

The radar system requires two different power dividers: one in-phase divider, and another quadrature phase divider. The designed in-phase divider is a classical 3-stage Wilkinson power divider. The transmission lines are replaced by lumped components to maintain acceptable die size. The schematic and the chip micrograph are shown in Figure 5.4 whereas Figure 5.5 shows the S-parameter results. The power divider shows better than -15 dB input and output return loss with maximum insertion loss of 3.8 dB for the two-way splitter and a minimum of 16.3 dB isolation within the 3-4GHz band.

The quadrature phase power divider is required to extract the in phase and quadrature phase LO signals for the I-Q mixer. A two-stage quadrature divider with transmission lines is first designed to achieve the required wide bandwidth. Then the transmission lines are replaced by lumped pi-networks with series capacitance and shunt inductances. This particular choice allows the shunt inductances of the middle branch to be combined in parallel which helped reducing the chip area since the inductances typically occupy the largest area. Since we do not need to have access to the isolation port, it is terminated by a

(a)

750 μm × 1450 μm
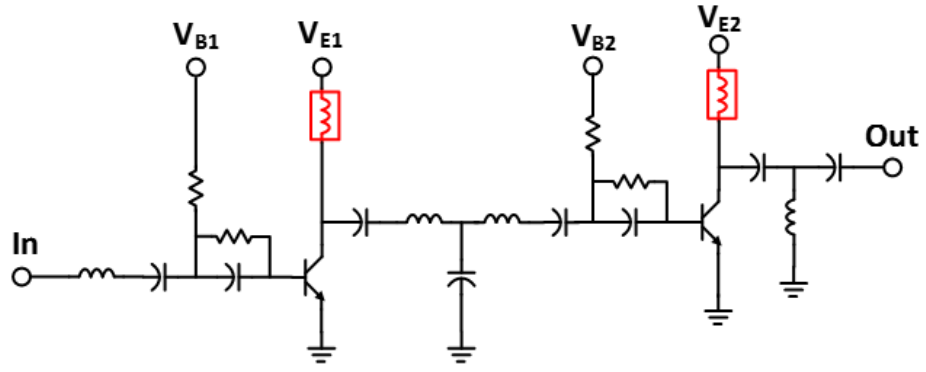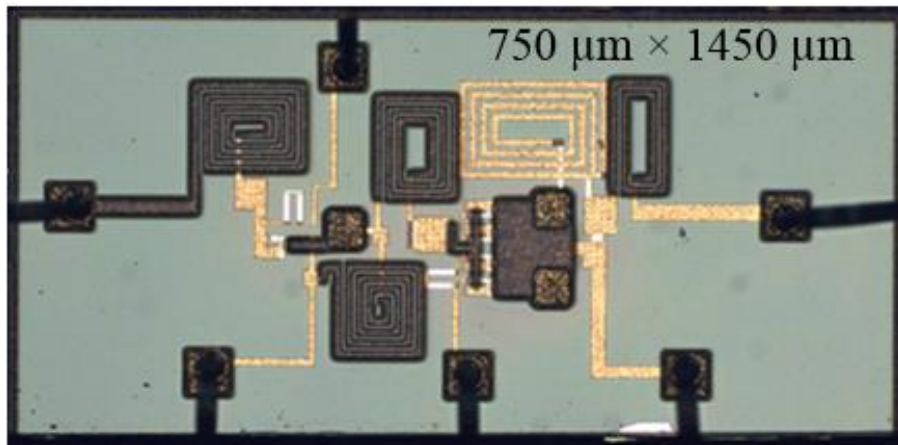
(b)

Figure 5.2: (a) Schematic of the designed GBA where the red components are off-chip RF choke inductors, (b) Micrograph of the fabricated die with 750 μm × 1450 μm size.
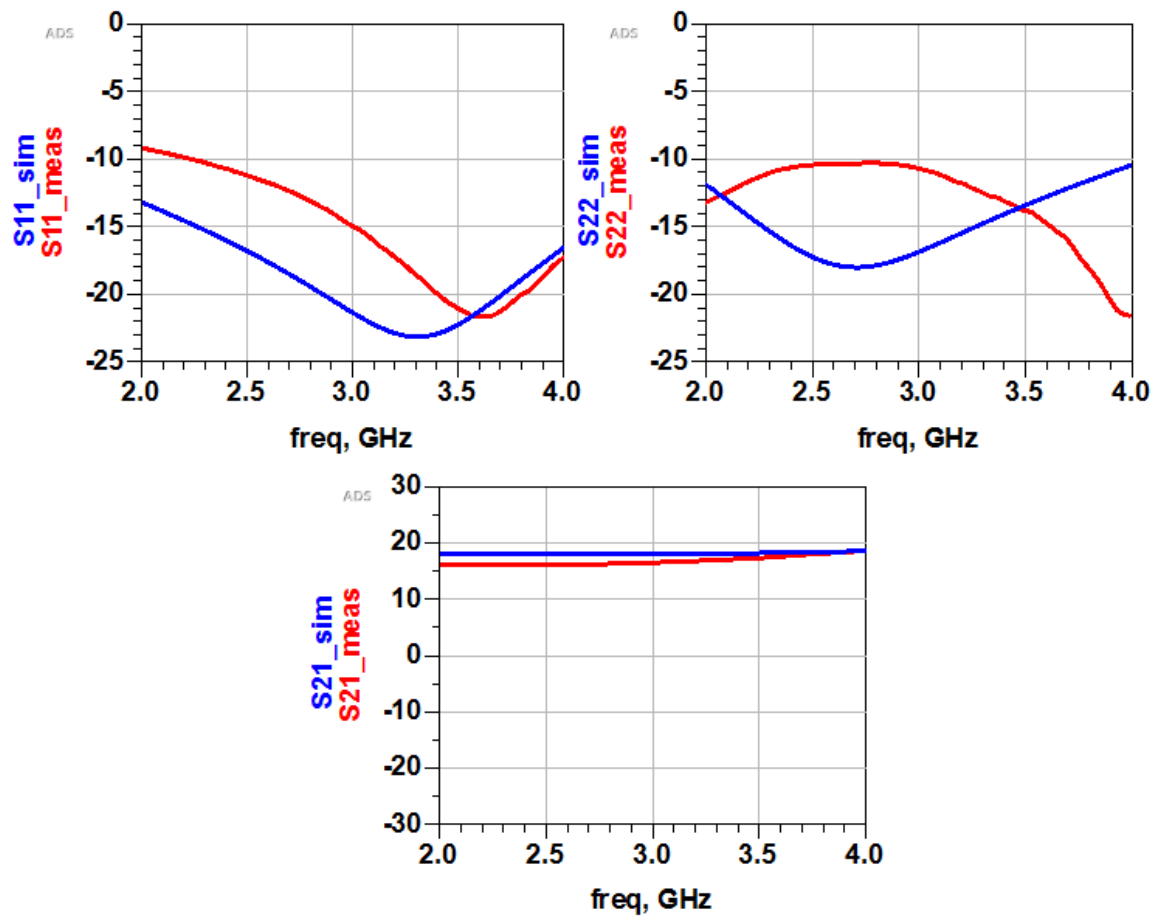
Figure 5.3: EM Simulated and measured S-parameters of the GBA.
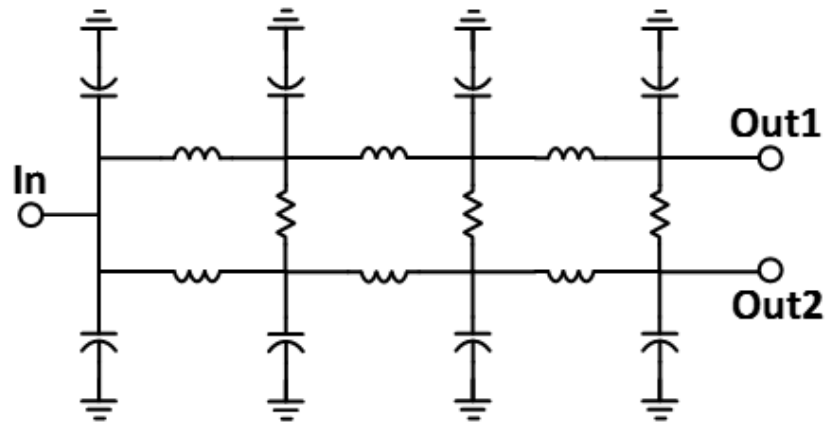
(a)
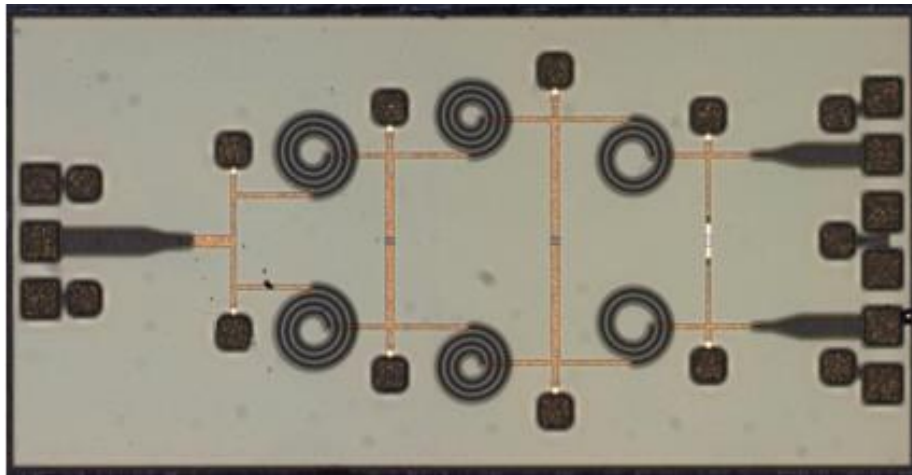
(b)

Figure 5.4: (a) Schematic of the designed Wilkinson power divider, (b) Micrograph of the fabricated die.
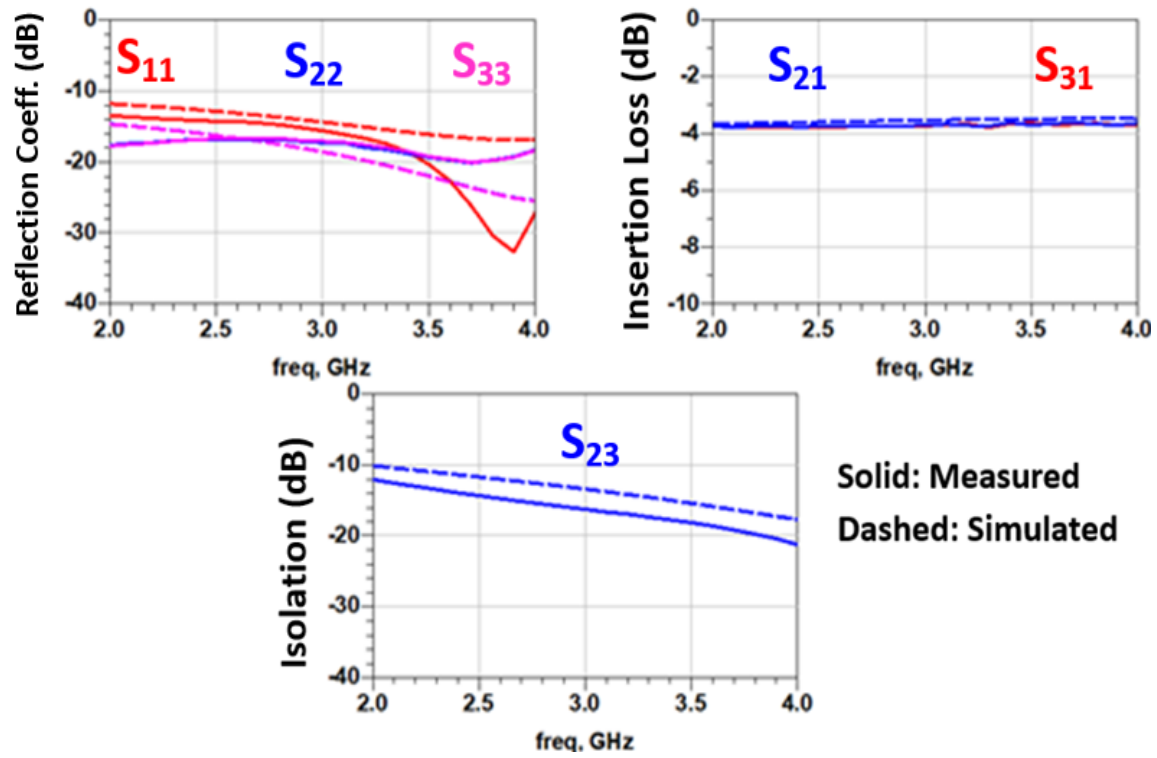
Figure 5.5: EM Simulated and measured S-parameters of the Wilkinson power divider.

50 ohm resistance inside the chip. The schematic and the chip micrograph of the fabricated Q-Hybrid is shown in Figure 5.6 and the S-parameters are shown in Figure 5.7. As it can be seen, the fabricated Q-Hybrid has better than -11 dB return loss with at least 16.5 dB isolation between the in-phase and quadrature phase ports. The maximum insertion loss is 6.7 dB with maximum 1.1 dB amplitude imbalance between the ports. The maximum deviation of phase the phase difference between the ports was 5.5° from the desired 90°.

5.2.3 Mixer

The design goals for the down-conversion mixer was 3-4 GHz RF and LO frequency with 0-20 MHz IF. For the design, a single balanced passive mixer based on two single-ended mixers represented by diodes combined with a quadrature hybrid junction. Even though passive mixers provide conversion loss during mixing operation, the particular topology was chosen due to its no DC power consumption requirement, good RF input match and RF-LO isolation capabilities. At the IF port, the low-pass filter was not integrated in the mixer MMIC because the component values were prohibitively large for the desired IF band. Therefore, an external 2nd order low-pass filter was utilized in the mixer evaluation board to provide the RF-IF and LO-IF isolation. The schematic of the mixer and the fabricated die photo are presented in Figure 5.8 (a) and (b) respectively. For an LO drive power of 5 dBm and RF input power of -5 dBm, the designed mixer provides a maximum 9.8 dB conversion loss across the 3-4 GHz band with at least 15 dB LO-RF isolation and maximum simulated 2.1 VSWR at the LO and RF ports as shown in Figure 5.9.
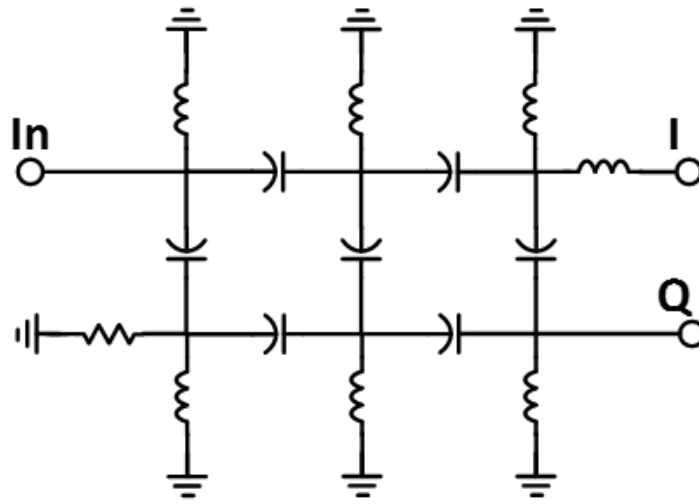
(a)
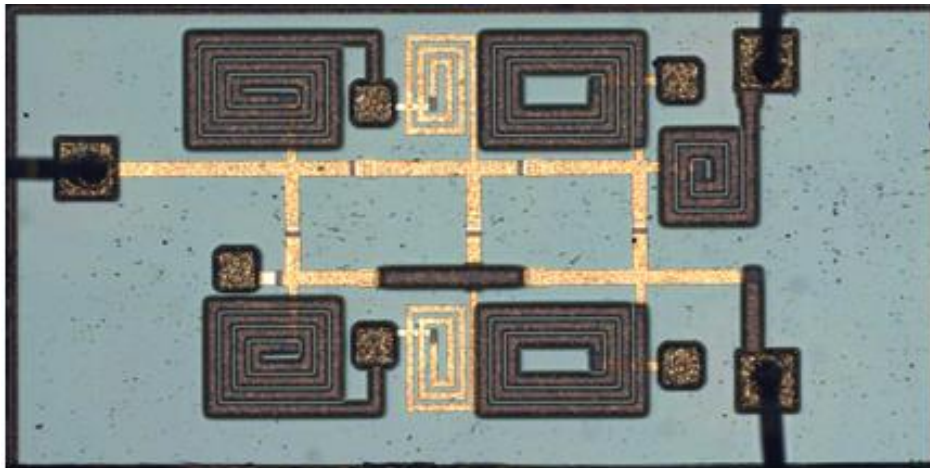
(b)

Figure 5.6: (a) Schematic of the designed Quadrature hybrid, (b) Micrograph of the fabricated die with 750 µm × 1450 µm size.
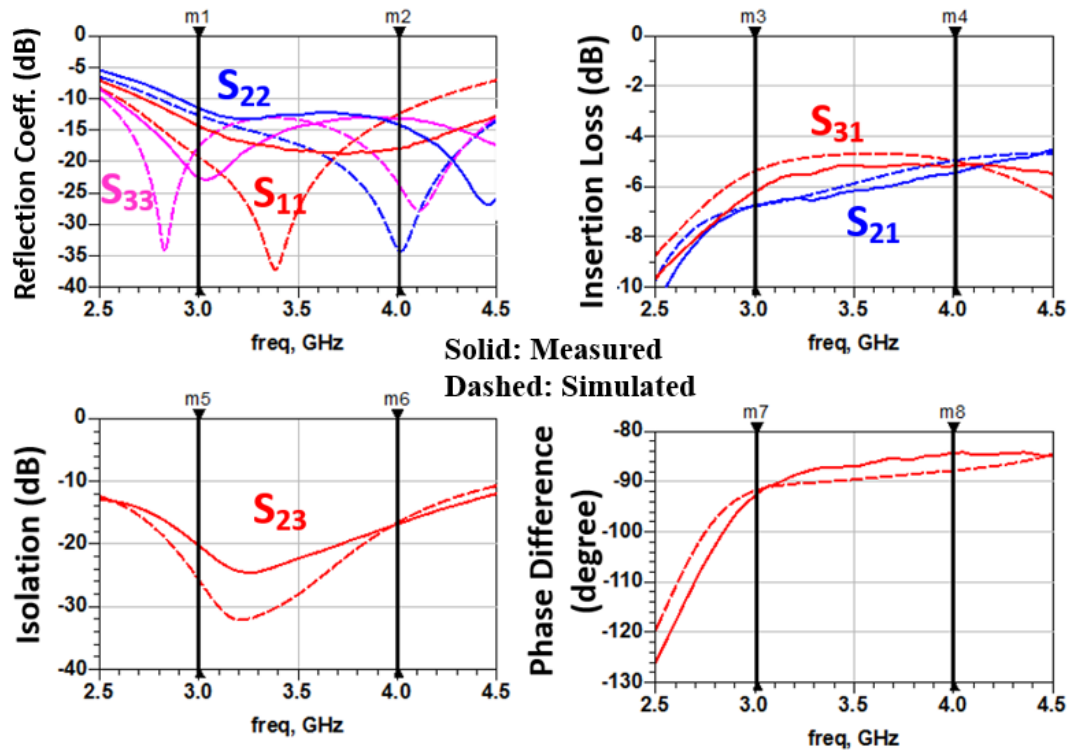
Figure 5.7: EM Simulated (dashed) and measured (solid) S-parameters of the quadrature hybrid.

(a)

(b)
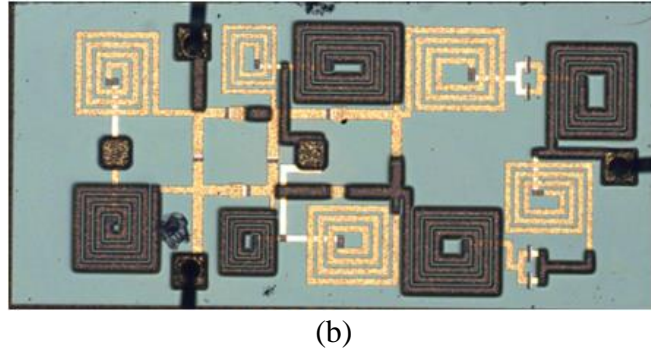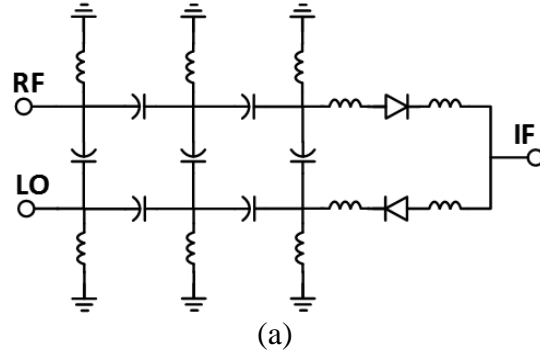
Figure 5.8: (a) Schematic of the single balanced passive mixer, (b) Micrograph of the fabricated die with 750 µm × 1450 µm size.

(a)

(b)

(c)
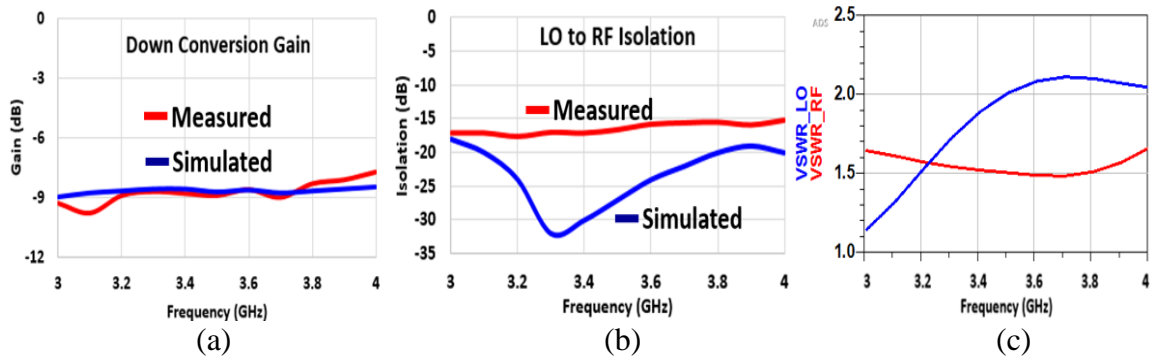
Figure 5.9: For LO = 5 dBm and RF = -5 dBm (a) the down-conversion gain, (b) the LO-RF isolation and (c) the simulated LO & RF VSWR of the designed mixer.

5.2.4 Low Noise Amplifier

The HBT process was not suitable for designing a low-noise amplifier because the process is not optimized for low-noise transistors. Therefore, the LNA is designed in Qorvo's internal pHEMT process. The LNA was a two-stage amplifier with inductive degeneration at the source. The first stage is implemented using a cascode structure with a large resistive feedback from the gate to the drain. This helps in broadening the input bandwidth by decreasing the quality factor (Q) of the input [5.4]. Also, the size of the first stage transistor was determined in a way to provide minimum average noise figure over the 3-4 GHz band for the DC bias current [5.5]. The LNA consumes 0.2 W of DC power from a power supply of 3.5 V. Figure 5.10 (a) shows the schematic of the LNA with the fabricated die photo shown in Figure 5.10 (b). The measured S-parameters and the noise figure of the LNA are shown in Figure 5.11. The LNA demonstrates an average small signal gain of 20 dB with about ±2 dB variation. The maximum measured noise figure of the LNA is 1.5 dB (at 4 GHz) which includes the losses of the evaluation board.

After the successful evaluation of the individual components, the complete radar system was implemented by connecting the individual evaluation boards through coaxial wires and connectors. A photograph of the system is shown in Figure 5.12 and the performance comparison with other radar systems is presented in Table 5.1. As we can see, although there is a room for improvement in the DC power consumption, the designed system provides the best performance in terms of the noise figure of the system. The motion analysis performance of the implemented system will be demonstrated in Chapter 7.
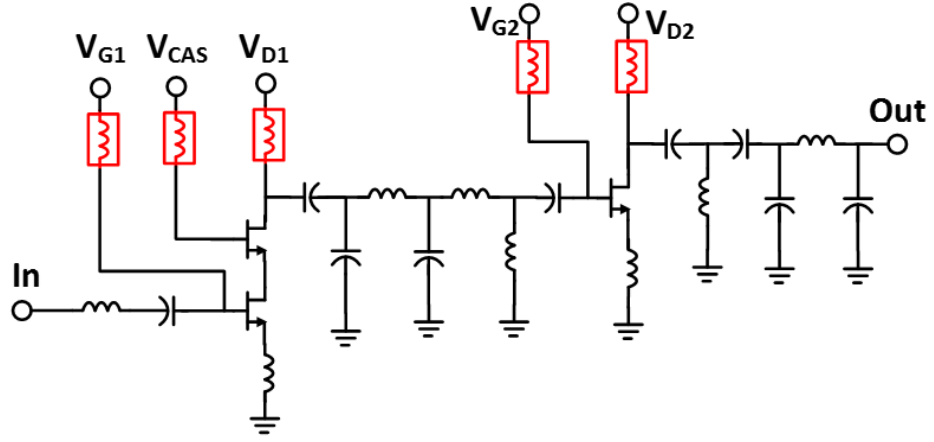
(a)
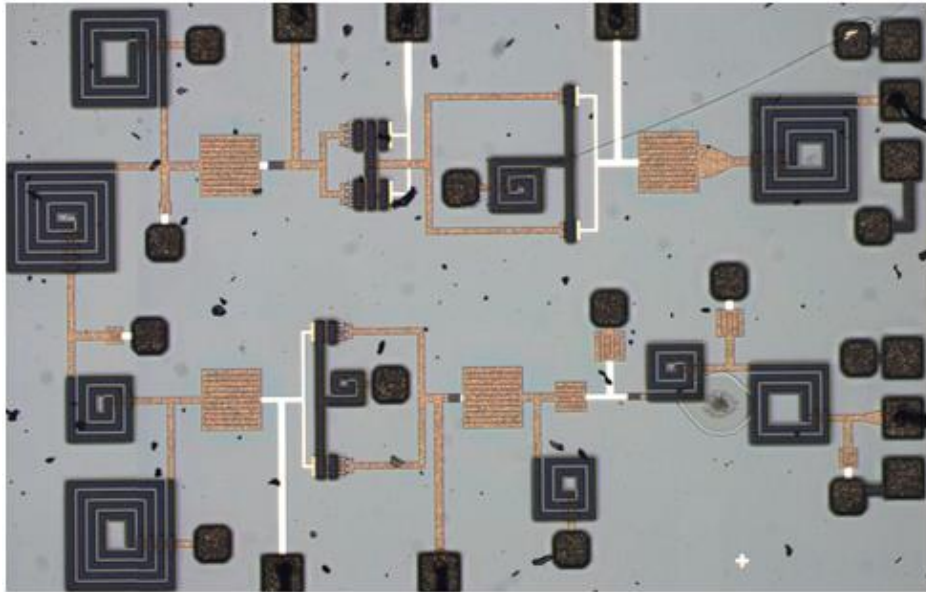
(b)

Figure 5.10: (a) Schematic of the LNA where the red components are off-chip RF choke inductors, (b) Micrograph of the fabricated die with 2500 µm × 1500 µm size.
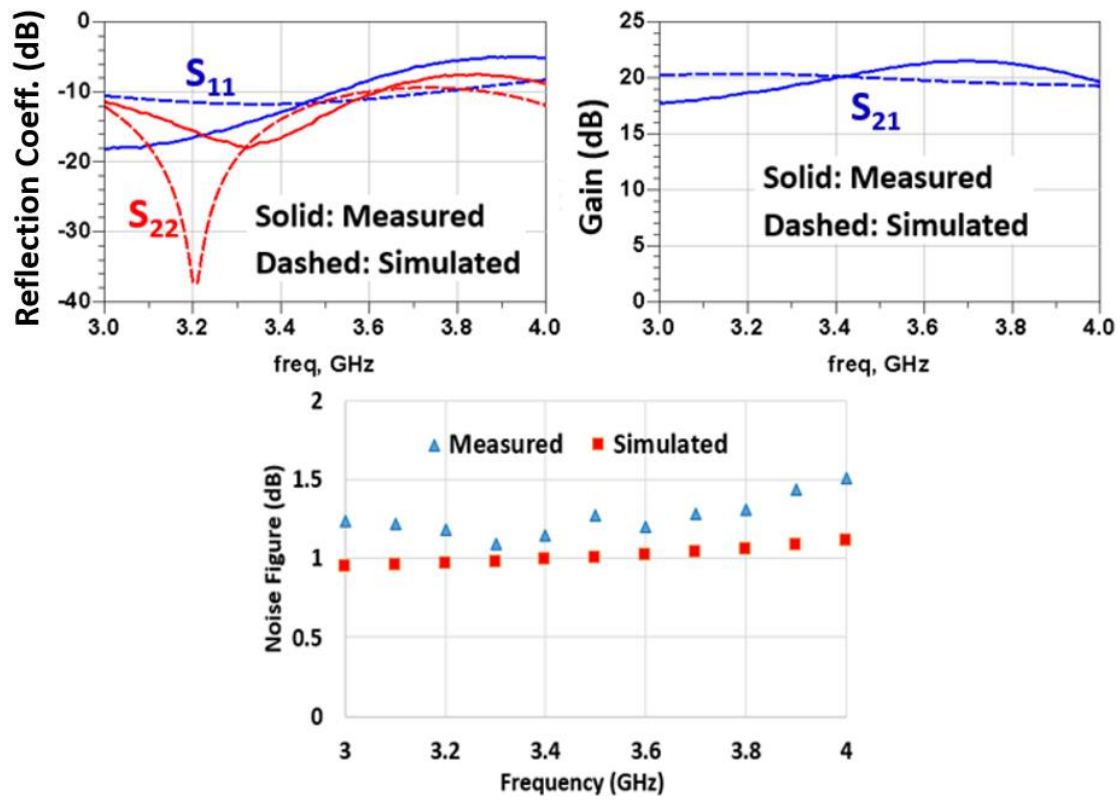
Figure 5.11: (a) EM simulated and measured S-parameters of the LNA, (b) Measured noise

figure including the board losses.
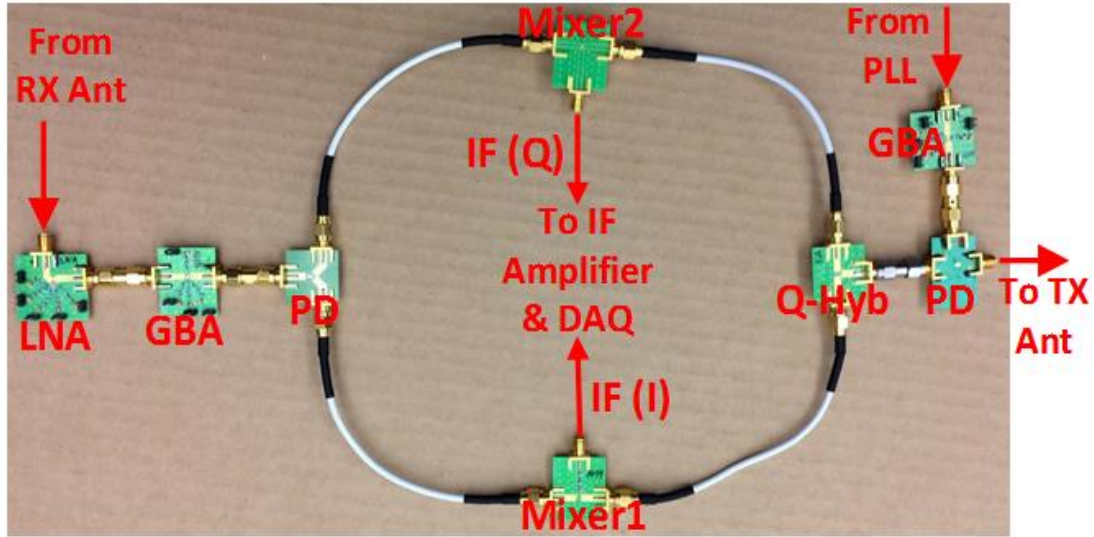
Figure 5.12: Implemented hybrid SFCW radar system using the designed front end ICs.

5.3 Conclusion

In this chapter, we discussed the design of integrated circuit components of the SFCW radar systems with a view to the implementation of a portable radar system. Compared to other reported works the designed system demonstrates excellent noise figure performance. It also provides better noise performance compared to the system that we implemented using the commercially available discrete components. Although the proposed system is still not integrated, it is certainly an important initial step towards the implementation of the whole system on a single printed circuit board and eventually a single IC.

Table 5.1: Performance comparison of the implemented hybrid radar with other wideband biomedical radar systems operating below 10 GHz.

Ref. (Year)	Process/Technique	Radar Type	Application	Freq. (GHz)	Tx Power (dBm)	Rx NF (dB)	P_{DC} (W)
[3.6] (2015)	65nm CMOS	SFCW	Med. Imaging	2-16	-14	5.4-8.4	0.204
[3.7] (2017)	65nm CMOS	Pulsed	Vital Signs	3-5	-	6-10*	0.017
[3.8] (2008)	180nm CMOS	Tunable CW	Vital Signs	Tunable 4.6-5.7	-6.1 to -12.5	-	0.042
[3.9] (2009)	130nm CMOS	Tunable CW Receiver	Vital Signs	Tunable 5.3-6.3		2.2*	0.022
[3.10] (2014)	130nm SiGe BiCMOS	FMCW	-	8-9	-	4.5*S	0.66
[3.11] (2017)	Hybrid	FMCW + CW	Localization & Vital Signs	5.64-5.96	8	-	-
[3.12] (2013)	Hybrid	SFCW	Fall Detection	5.8-7	2	-	-
This work (Discrete)	Discrete	SFCW	Human Sensing	2-3	8	1.8	1.04
This work	III-V HBT and HEMT	SFCW	Human Sensing	3-4	12	1.1-1.5*	1.0

S: Simulated, *: LNA Only

CHAPTER SIX
SIGNAL PROCESSING ALGORITHM AND MOTION MODELING

After developing the hardware platform for a non-contact gait analysis system, it is important to establish a signal processing algorithm to extract the features of individual limb joints using the data collected by the radar. Again, our goal is to utilize an algorithm that can distinctly track human limb joints such as the hands, legs and torso for complex motions using either a simple Doppler radar or a UWB radar operating in a typical laboratory environment. With that in mind, we utilize the 1-D block technique, which is a robust algorithm for extracting signal components from complex targets that depict non-linear motions corrupted with noise. We also introduce our motion modeling efforts that provide repeatable and realistic reference data which when coupled with the signal processing technique can be useful for obtaining a full understanding of human limb joint motion analysis.

6.1 1-D Block Processing Algorithm

The algorithm was first proposed by Dr. K. Naishadham and Dr. J. E. Piou in [6.1], from MIT Lincoln Laboratory. This method was previously utilized for vital signs detection using UWB impulse radar [6.2], and for system identification [6.3]. We extended this method for gait analysis using either CW or UWB radar which can be vitally important in applications such as treating patients with joint problems, athlete performance analysis, motion classification, and so on. The algorithm development is independent of the type of

radar used apart from differences in the dimensions of some of the intermediate variables due to the difference of dimensions in the data from CW and UWB radar. The algorithm development and those differences are discussed below:

6.1.1 UWB Data Usage

This discussion follows the development of the algorithm for UWB radar that was presented previously in [6.1] and [6.2]. It is assumed that the 2-D data collected from a UWB radar data collected on a human subject and corrupted with white Gaussian noise *w(m,n)* can be defined by the samples *y(m,n)* according to:

$$y(m,n) = \sum_{i=1}^{P} a_i s_i^m p_i^n + w(m,n), \quad m = 1, \ldots, L, \ldots, M \ and \ n = 1, \ldots, K, \ldots, N \quad (6.1)$$

where *P* denotes the number of signals that compose the data, which is termed as the order of the signal. *M* is the total number of frequencies and *N* is the number of time acquisitions. The spectral model of the ith body movement from a human subject is associated with the pole pair (s_i, p_i) and the complex amplitude a_i is defined by

$$a_i = |a_i| e^{j\varphi_i} \qquad (6.2)$$

where φ_i denotes the phase. The poles s_i and p_i yield the frequencies that describe the limb movements of a human subject in range and Doppler, respectively. These frequencies can be estimated according to

$$r_i = \frac{\theta_i}{2\pi} \ and \ f_i = \frac{\beta_i}{2\pi} \tag{6.3}$$

where θ_i and $\boldsymbol{\beta}_i$ refer to the phase angles associated with s_i and p_i respectively.

The 1-D block processing technique based on the state space method provides poles (or frequencies) in one direction of the human body movements (i.e., either r_i or f_i in Eq. 6.3) from the eigenvalues of the state transition matrix, A_r, to be defined shortly. These poles are representative of the entire data set, as no samples are discarded in constructing the block enhanced Hankel matrix leading to A_r. Further operations on the enhanced block Hankel matrix result in a robust state-space model for human motion. By processing overlapped blocks of pulses (which represent sliding time windows) sequentially, the torso, arm, elbow, knee, ankle, toe, etc. movements from a human subject can be detected and tracked over time.

Based on the 2-D data formulation in Eq. 6.1, the matrix notation of $M \times N$ acquisition time measurements may be written as:

$$Y = \begin{bmatrix} y(1,1) & L & y(1,N) \\ y(2,1) & L & y(2,N) \\ M & L & M \\ y(M-1,1) & L & y(M-1,N) \\ y(M,1) & L & y(M,N) \end{bmatrix} \tag{6.4}$$

One can form Hankel (or forward-prediction) matrices with every row or column of the data matrix defined in Eq. 6.4. For example, the Hankel matrices of the mth row and n^{th} column, respectively, are given by Eq. 6.5 and 6.6 below:

$$H_m^{row} = \begin{bmatrix} y(m,1) & L & y(m,L) \\ y(m,2) & L & y(m,L+1) \\ M & L & M \\ y(m,N-L+1) & L & y(m,N) \end{bmatrix} \qquad (6.5)$$

$$H_n^{col} = \begin{bmatrix} y(1,n) & L & y(J,n) \\ y(2,n) & L & y(J+1,n) \\ M & L & M \\ y(M-J+1,n) & L & y(M,n) \end{bmatrix} \qquad (6.6)$$

The parameters L and J that appear in Eq. 6.5 and 6.6 denote the lengths of the correlation windows in column and row directions, respectively. They are heuristically chosen to be L = [N/2] and J = [M/2], where the brackets denote the smallest integer less than or equal to the inserted quantity. The primary interest in this section is modeling 2-D vital sign data by using one set of complex matrices. This set is derived from state-space operations carried out on a *row-enhanced* data matrix, obtained by stacking the M Hankel matrices described by Eq. 6.5 into a column vector such that:

$$H^{row} = [H_1^{row} \ H_2^{row} \ L \ H_M^{row}]^T \qquad (6.7)$$

An autoregressive moving average (ARMA) model is now derived from the enhanced data matrix defined in Eq. 6.7. The proposed 1-D block-processing state-space system relates the input, consisting of an impulse matrix W_k^r to the output H_k^{row} and is characterized by the following equations:

$$X_{k+1}^r = A_r X_k^r + B_r W_k^r \qquad (6.8)$$

$$H_k^{row} = C_r X_k^r \qquad (6.9)$$

where $X_k^r \in \pounds^{P \times L}$ is the state, and $W_k^r \in \pounds^{L \times L}$ denotes the input with Dirac functions on its main diagonal and zero elsewhere. $A_r \in \pounds^{P \times P}, B_r \in \pounds^{P \times L}$ and $C_r \in \pounds^{(N-L+1) \times P}$ are coefficient matrices. It follows from Eq. 6.8 and 6.9 that:

$$H_k^{row} = C_r A_r^{k-1} B_r, k = 1, 2, \ldots, M \tag{6.10}$$

Eq. 6.10 indicates that an enhanced Hankel matrix H_e^{row} formed from a sequence of impulse responses such that:

$$H_e^{row} = \begin{bmatrix} H_1^{row} & H_2^{row} & .. & H_J^{row} \\ H_2^{row} & H_3^{row} & .. & H_{J+1}^{row} \\ \vdots & \vdots & .. & \vdots \\ H_{M-J+1}^{row} & H_{M-J+2}^{row} & .. & H_M^{row} \end{bmatrix} \tag{6.11}$$

can be factored. The decomposition of H_e^{row} into a product of two matrices is given by

$$H_e^{row} = \Omega \Gamma \tag{6.12}$$

where Ω and Γ denote the observability and controllability matrices, respectively, and are given by:

$$\Omega = \begin{bmatrix} C_r & C_r A_r & \ldots & C_r A_r^{M-J} \end{bmatrix}^T \tag{6.13}$$

$$\Gamma = \begin{bmatrix} B_r & A_r B_r & \ldots & A_r^{J-1} B_r \end{bmatrix} \tag{6.14}$$

By computing the singular value decomposition of the enhanced Hankel matrix, H_e^{row} and performing a P rank reduction, one obtains

$$H^{row} = U_{sn} \Sigma_{sn} V_{sn}^* \tag{6.15}$$

103

where U_{sn} denotes the signal components of the left-unitary matrix, $\sum_{sn}$ is a diagonal matrix with dominant signal singular values of H_e^{row} arranged in decreasing order, V_{sn} is the signal component of the right-unitary matrix and $*$ denotes the Hermitian operator. Therefore, the observability and controllability matrices, respectively, are given by:

$$\Omega = U_{sn}\Sigma_{sn}^{1/2} \tag{6.16}$$

$$\Gamma = \Sigma_{sn}^{1/2}V_{sn}{}^* \tag{6.17}$$

As reported in [6.4], the state-space matrices (A_r, B_r, C_r) described by (6.8) and (6.9) may be derived from Ω and are given by

$$A_r = \left(\Omega_{-rf}{}^*\Omega_{-rl}\right)^{-1}\Omega_{-rl}{}^*\Omega_{-rf} \tag{6.18}$$

$$B_r = (\Omega_M{}^*\Omega_M)^{-1}\Omega_M{}^*H^{row} \tag{6.19}$$

$$C_r = \Omega(1:N-L+1,:) \tag{6.20}$$

where H^{row} is defined by Eq. 6.7, and

$$\Omega_{-rf} = \Omega(N-L+2:(M-J+1)(N-L+1),:) \tag{6.21}$$

$$\Omega_{-rl} = \Omega(1:(M-J)(N-L+1),:) \tag{6.22}$$

and Ω_M is given by Eq. 6.13 with $J = 1$. In Eq. 6.21 and 6.22, $\Omega(k{:}l,:)$ denotes the matrix obtained by retaining rows k to l of Ω. Once the state-space matrices are obtained, Eq. (6.18) can be used to compute the frequencies that are associated with the limb motions of the human subject. An eigenvalue-eigenvector decomposition carried out on A_r defined by Eq. (6.18) allows the following derivation:

$$A_r = M_r \Lambda_r M_r^{-1} \qquad\qquad (6.23)$$

where Λ_r is a diagonal matrix with the eigenvalues $\lambda_i\{A_r\} = [\lambda_1,\ L,\ \lambda_P]$ (or the state-space poles) as the diagonal entries, M_r is the matrix of eigenvectors with column vectors $[v_1,\ L,\ v_P]$ associated with their corresponding eigenvalues. Thus, the eigenvalues λ_i yield the damping factors α_i and the frequencies f_i

$$\alpha_i = \frac{log|\lambda_i|}{\Delta t},\ \ f_i = \frac{angle(\lambda_i)}{2\pi\Delta t}, \qquad i = 1, ..., K, ...P \quad (6.24)$$

Based on Eq. 6.10, it is not difficult to model the data matrix or fit of the kth pulse from the ith eigenvalue λ_i:

$$F(k,:,i) = [D(1,:,i)\ \ D(2:N-L+1,B,i)^T] \qquad\qquad (6.25)$$

where N-L+1 denotes the number of rows in the matrix C_r and B is the number of columns in the matrix B_r. The matrix D is given by:

$$D(:,:,i) = G(:,i)\lambda_i^{k-1}Q(i,:) \qquad\qquad (6.26)$$

where the matrices G and Q are defined by:

$$G = C_r M_r\ and\ Q = M_r^{-1}B_r \qquad\qquad (6.27)$$

where C_r, B_r and M_r are previously reported.

For complex motions like human walking, the radar returns from some limb joints are much stronger than others. For example, the lower leg and torso have typically much stronger returns compared to upper legs and hands. Thus, it becomes very difficult to simultaneously track these parts in the presence of the strong returns from the lower legs and torso. In such scenarios, we have adopted a residual superposition approach in which the stronger and weaker joints are tracked in multiple steps. In this method, the algorithm is first run to extract the trajectories of the limb joints with stronger reflections and the data fit according to Eq. 6.25 is generated from the associated poles and amplitudes. Next, the data fit is subtracted from the original data to obtain a residual signal that corresponds to the scattered signals from the weaker joints. Thus, the residual is passed through the 1-D block processing algorithm again and the steps are repeated until all the desired joint trajectories are extracted.

6.1.2 Using CW Data

The formulation of the CW data is obtained by collapsing the range dimension of the UWB data utilized before in [6.2]. Then the signal from a CW radar can be defined by:

$$y(n) = \sum_{i=1}^{P} a_i p_i^n + w(n), \quad n = 1, \dots., K, \dots., N \tag{6.28}$$

where P again denotes the number of signals that compose the data, N is the number of time samples and the body movement is related to the pole p_i. For the CW radar, we do not have range information, thus the poles related to range (s_i) and the associated frequencies (r_i) are absent in this case.

106

Following the 1-D signal model defined by Eq. 6.28, the vector notation of N acquisition time measurements may be written as:

$$Y = [y(1) \quad y(2) \quad K \quad y(N)] \tag{6.29}$$

Thus, the Hankel (or forward-prediction) matrix from the data vector defined in Eq. 6.28 may be considered as the first row of the data matrix in Eq. 6.5 and can be computed according to:

$$H_1^{row} = \begin{bmatrix} y(1) & K & y(L) \\ y(2) & K & y(L+1) \\ K & K & K \\ y(N-L+1) & K & y(N) \end{bmatrix} \tag{6.30}$$

where L is still $[N/2]$. Note that, since the data Y is now a vector instead of a matrix like the UWB case, the analysis is equivalent to having $M = 1$ and $J = 1$ from the previous section. Thus, the row enhanced data matrix H_1^{row} defined in Eq. 6.11 boils down to:

$$H_e^{row} = H_1^{row} = \Omega \Gamma \tag{6.31}$$

where observability and controllability matrices still have the same definitions as presented in Eq. 6.16 and 6.17. The state-transition matrix A_r can also be calculated using Eq. 6.18 although the definition of Ω_{-r1} and Ω_{-rl} are different due to the absence of the second dimension of the data:

$$\Omega_{-r1} = \Omega(2:N-L+1,:) \text{ and } \Omega_{-rl} = \Omega(1:N-L,:) \tag{6.32}$$

The eigenvalues can be calculated in the same technique like the UWB case and the data vector or fit from the ith eigenvalue λ_i can be modeled according to:

$$F(k, i) = \alpha_i \lambda_i^{k-1}, \qquad k = 1, ..., K, ... N \qquad (6.33)$$

In general, the state transition matrix computed from the row/column enhanced Hankel matrix exhibits high smoothing due to its large number of row and column entries and provides more accurate frequency estimates than those computed from the state transition matrix of ST-SSM that is carried out from a simple Hankel matrix [2.10]. Because of the structure inherent of the 1-D block processing, in the case of a single tone, the state transition matrix carried out from the observability Gramian can better capture the dynamics and the nonlinearity of the weak scatterers than the state transition matrix computed from ST-SSM. This feature allows the 1-D block method to successfully extract the features using not only UWB radar data, but also CW data as well.

6.1.3 Steps for Gait Analysis Using 1-D Block Method

Below the steps to track limb joints using the 1-D block processing algorithm from radar data are summarized:

1) Select a model order or number of poles that represents the number of signals or joints to track, P in the formula. There are many techniques to get an initial estimate of the model order. The technique that we employ is to look for a knee in the plot of the singular values computed from the singular value decomposition (SVD) of the Hankel matrix. The singular value matrix Σ carried out on the block Hankel matrix defined by Eq. 6.11 for UWB or Eq.

6.31 for CW can be used to estimate the model order, i.e., the number of signals associated with the key joins or limb components that give rise to the data. The large singular values in Σ are attributed to strong signal components, while the smaller values are associated generally with noise. For low noise levels, one can expect a sharp transition or knee between the large and small singular values, i.e., it provides a separation between the signal space and the noise space. Therefore, this transition point or knee can be used as an estimate of the number of signals embedded in the data as known as model order. Typically, this number is smaller than the number of desired joints to track. Examples of this technique being implemented are shown in the next chapter.

2) Due to the non-linearity of the data, choose the block size or the sliding time window to lie over a fraction of one normal motion period of a human gait to achieve adequate timing and frequency resolution. For example, if a particular motion lasts for 0.6 s in one direction, start with a time window size of half that period and decrease the window size gradually if required.

3) Form the Hankel matrix and compute the state transition matrix, A_r.

4) Compute the eigenvalue decomposition of A_r to obtain the damping factors α_i and frequencies f_i.

5) Use Eq. 6.25 for UWB or Eq. 6.33 for CW to model the data vector or fit from the λ_i computed from the radar data for all the eigenvalues.

6) For complex motions where tracking of many signals may be needed, the model order can be chosen to capture the stronger signals first. Next a data residual is extracted by subtracting the fit (derived from the poles or eigenvalues and amplitudes of the stronger signals) from the original data then repeat steps 3-5 with appropriate model order.

7) Repeat step 6 until all the desired limb joints are identified.

8) Since there will be more extracted features than the desired number of joints to track, identify the appropriate features by comparing the extracted results with the reference motion model described in the next section.

A flowchart of the method is presented in Figure 6.1 and the extracted results using the method on both CW and UWB radar data are presented in Chapter 7.

6.2 Motion Modeling

A big hurdle in gait analysis is data variability, inaccuracy, and repeatability that make interpreting the data an exhaustive task. Electromagnetic modeling could provide the means to minimize gait analysis interpretation efforts and enhance its value by isolating the effects from individual components in the scene and enabling a completely repeatable system to fine tune signal processing algorithms. Thus, we utilized a Full wave electromagnetic (EM) model that our collaborators from Catholic University of America (CUA) created. The model is based on a mechanical Boulic model [6.5] where the motion
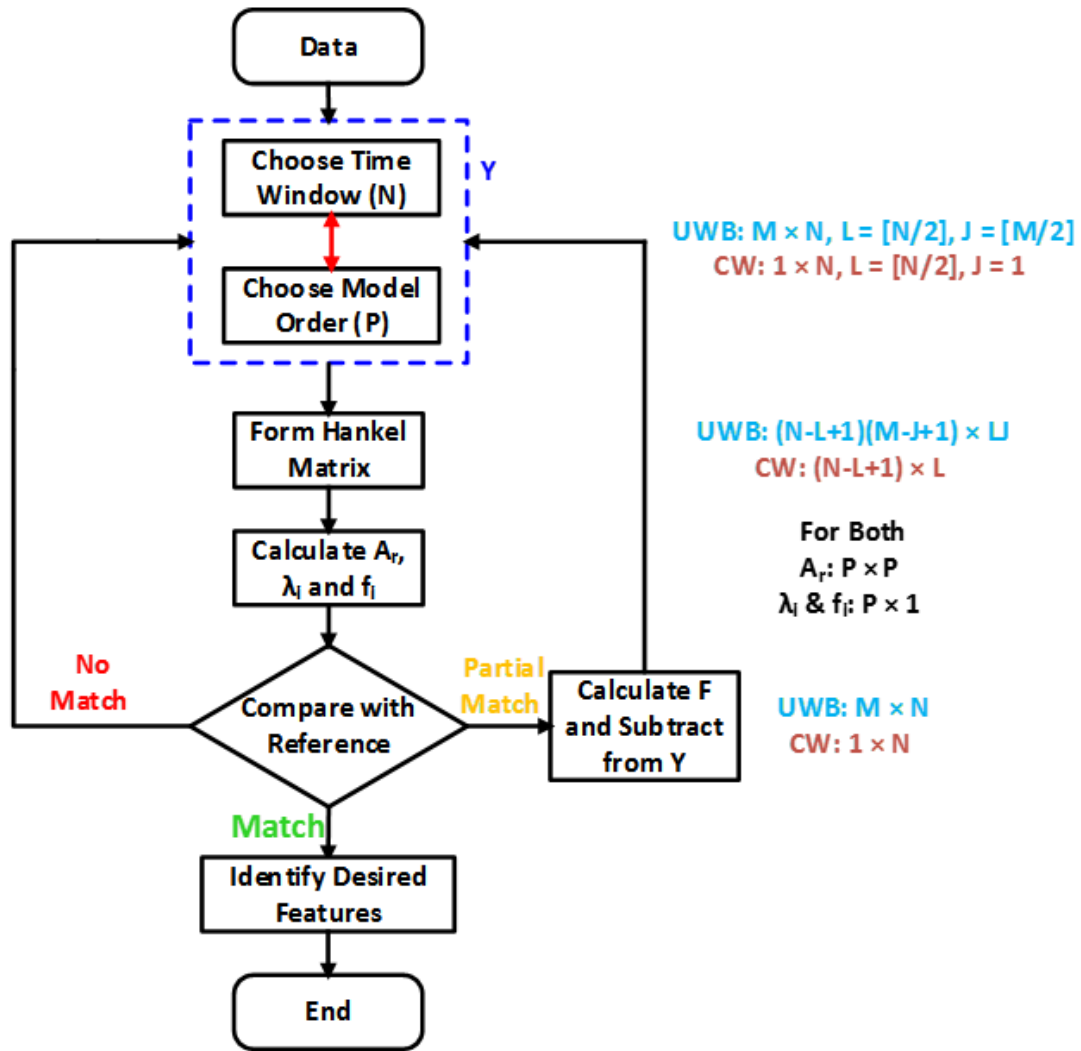
Figure: 6.1: Gait analysis flowchart using the 1-D block algorithm where the dimensions of the different variables are presented on the right side.

is emulated based on detailed video tracked motion scenarios. The body schematic model from Boulic is used to build a more realistic human body model that is used as an object for the radar EM model. The emulated EM model can be useful for obtaining a clean set of repeatable reference data that can take different realistic settings into account that the mechanical Boulic model cannot, such as body shape and material, noise, ground reflection, and parts interference.

We developed human motion models for simple scenarios like a human standing and swinging the right hand only, a human sitting and swinging his/her right foot only, and a human walking without hand motion for electromagnetic analysis. Using full wave EM analysis, the resulting scattered fields from the scene are calculated for each transmitted plane wave CW signal. Details of the developed human activity models are described in the following section:

6.2.1 Human Motion Model

First, based on the input of the height of the human subject, a human skeleton is created using 16 joints (e.g. shoulders, hips, knees, ankles, etc.) connecting the head and the rest of the human body parts. Ellipsoids with appropriate semi-axes lengths corresponding to reasonable dimensions [6.6] of the associated body parts are used to model the human body parts and the head is represented by a sphere. Next, the kinematics of various human motions such as a human standing with right hand swinging and a human sitting with right foot swinging are modeled to demonstrate the range of our EM modeling capabilities. These motions are deduced by adapting the conventional Boulic model to match the video

tracking data from a real motion scene. In the empirical Boulic model [6.5], a human subject is walking with a certain velocity and it needs two inputs to model the forward human walking: velocity and height of the human. Some temporal and spatial motion characteristics are defined based on the velocity of the human such as the duration and the length of a walking cycle. Using these motion characteristics, the position of every joint in a human body is defined at every frame based on analytical expressions to compute the rotation and translation of joints. More detailed and specific examples of CUA's work can be found in [6.7-6.8].

In CUA's modified model for the one hand or one leg swinging case, all the body parts are stationary except for the right hand or the right foot. In the right hand swing case, the rotational angles of the right shoulder and right elbow from the Boulic model are modified to match the video tracker data extracted from a real scene. Similarly, the rotational angles of the right knee are also tweaked to emulate the real video recorded motions. CUA also modified the Boulic model to create the walking without moving hands motion. In this case, the rotational angles of both shoulders and elbows are fixed to a crossed arm position, but the rest of the limbs move in its usual motion. Figure 6.2 shows the three different motion characteristics considered for EM analysis. The left side samples the human motions at five instances within one cycle of the human motions. Figure 6.2 (a) depicts a human standing with the right hand swinging, Figure 6.2 (b) corresponds to a human sitting and swinging the right foot, while Figure 6.2 (c) shows the motion where the subject is walking without hand movement. The right-hand side of Figure 6.2 shows the velocities of the different body parts for each of these scenarios.

113
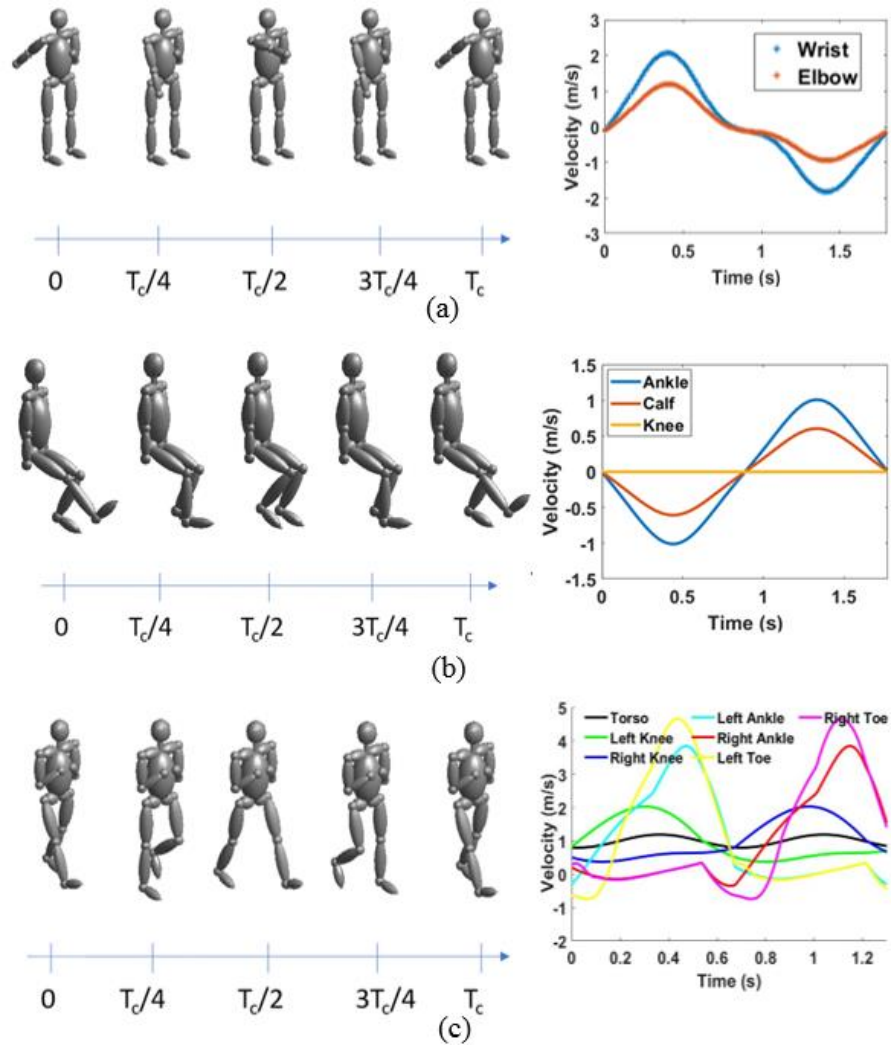
Figure 6.2: Human motion model and velocity comparisons, (a) human standing with swinging right hand only, (b) human sitting with swinging right foot only and (c) human walking without moving hands.

6.2.2 EM Scattering Model Implementation

The Method of Moments (MoM) enhanced with Multilevel Fast Multipole Algorithm (MLFMA) is implemented not only to speed up the computation but also to conserve memory resources. CUA utilized the EM simulator FEKO tool [6.9] from Altair Engineering for the analysis where the human body is meshed with a fine mesh of about $\lambda/10$ to fully incorporate the mutual coupling between human body parts. MLFMA is based on a grouping concept that helps in speeding up the iterative solution of the $ZI = V$ linear equation system of the conventional MoM [6.10], where Z represents the impedance matrix, I is the unknown currents, and V is dependent on the incident field. The first step for implementing this grouping concept of MLFMA is meshing of the surface of the given structure into M edges, which are then categorized into an N-level tree structure that connects groups of different sizes from the finest to the coarsest level for a spherical object. The next step involves splitting the impedance matrix Z into near (Z_{near}) and far (Z_{far}) matrices. After this, with the Z matrix known, the unknown values of the current (I) can be solved iteratively according to [6.11-6.12].

In order to limit the prohibitively long computation time of this large problem, CUA accelerate the computations on our GPU cluster by parallelizing the MLFMA. A uniform workload allocation is achieved by distributing the computations among the available computing nodes. The message passing interface (MPI) library along with CUDA programming model is utilized to distribute computations among various GPU nodes. Further details of CUA's previous efforts on hardware accelerated EM modeling along with their MLFMA implementation on GPU clusters can be found in [6.13].

6.3 Conclusion

In this chapter, we focused on the 1-D block algorithm development for individual limb joint tracking, which was originally proposed by our collaborators at MIT Lincoln Laboratory. Due to its signal development, the algorithm provides the capability to track the desired features for data obtained from either CW or UWB radar. We also discussed the general steps of using the algorithm for gait analysis including the choice of initial parameters. The application of this algorithm will be shown in the next chapter. We also described the development of accurate EM models for different motions for initial investigation of the signal processing algorithm and hardware prototyping. During EM analysis, we can model the effects of noise, ground reflection, interference of other surrounding objects and the interference between different body joints in motion. A combination of all these capabilities allows the EM analysis to provide a realistic, repeatable reference data for any given scenario which can be utilized as the ground truth for the user.

CHAPTER SEVEN
RESULTS

In this chapter we will investigate the gait analysis results using the hardware and software methods discussed in the previous chapters. We have divided the results into two sections: the first section discusses the findings from the SDR based CW radar whereas the second section presents the results from the SFCW radar. We then present a discussion on the results by first showing side by side comparison of our results with other published results and then highlighting some limitations of our method. Finally, we report the suitability of our hardware system for vital signs (respiration and heart rate) detection as well.

7.1 CW Radar

We utilized the software-defined radar (SDRadar) running with the MATLAB platform for these experiments. A 2.45 GHz CW signal is generated using the SDRadar and the TX port in connected to a horn antenna, which has a gain of about 9.5 dB. The maximum range utilized in these experiments is 4.5 m and the reflected signal captured by the receiving horn antenna which is similar to the TX antenna from a subject at that maximum distance away from the antennas is -41 dBm, which was 20 dB higher than the minimum detectable signal by the receiver. Both the TX and RX horn antennas had a 3-dB beamwidth of $\pm 20°$ in the vertical and horizontal directions. The data was captured at a rate of 1 MHz, which was later decimated to a rate of 200 Hz which was enough to capture a Doppler frequency of ± 100 Hz. We began the investigation with performing the simple short-term Fourier

transform (STFT) previously used by many researchers [2.1, 2.2, 2.6, 2.9, 2.20-2.28] as reported in Chapter 2. STFT is an easy and convenient way to look at the combined time-frequency spectrogram to validate our hardware system and the EM modeling. Then we moved onto using the more sophisticated 1-D block method to extract the features of individual limb joints. Below the results from the two methods are presented:

7.1.1 STFT Results

We utilize the previously described spectrogram function in MATLAB to perform the STFT analysis. For the first experiment, a subject stood stationary 1.5 m away from the radar and swung his right-hand back and forth. The idea is to create a simple periodic motion using the hands and track the elbow and the wrist trajectories. The same motion was initially modeled using the Boulic model and then an EM simulation was performed with identical radar parameters where the motion details were video recorded and utilized to develop the EM model. In the second experiment a similar scenario was repeated where the subject sat on a chair 1.5 m away from the radar and swung his right leg while keeping the knee joint position fixed. Figure 7.1 shows the results of these two motions using both EM simulated and experimental data.

Note that the results from the simulation correspond very well with the measured results in terms of the shape of the spectrograms and the velocity values. Although the intensities of the signals are different since the simulated results do not encounter any interference from unwanted targets and uses a plane wave assumption which is not the case for measured results.

118
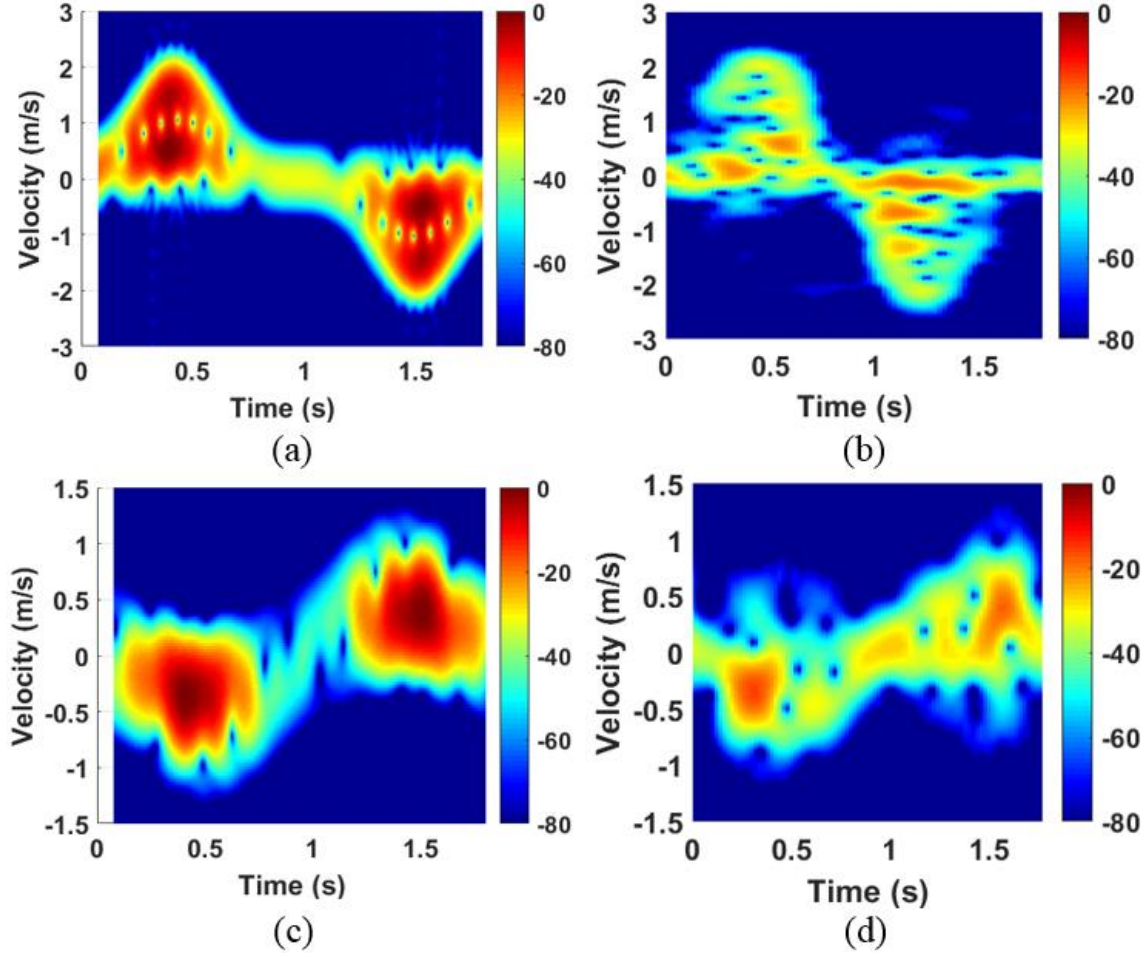
Figure 7.1: STFT results for a subject standing and swinging one hand only (a) from EM simulated data, (b) from measured data. STFT spectrograms for a subject sitting and swinging one leg only (c) from EM simulated data, and (d) measured data. In all cases, the STFT is run with *fs* = 200, *window* = 64, *noverlap* = 60. The Doppler frequencies are converted into velocities according to the 2.45 GHz radar operating frequency.

Next, the complexity of the motion was slightly increased by having the subject walk without any hand motion. The scenario was intended for tracking the lower body parts (toes, ankles, knees) and the torso. In the Boulic based EM model, the subject walks towards the radar at a velocity of 1 ms^{-1} with a regular leg motion but without swinging the hand. In the measurement scenario, the subject started 4.5 m away from the radar and walked with a similar motion and it was ensured that the transmitting and receiving antennas illuminated the whole body. With the antennas placed 0.9 m above the ground, a subject with a 1.8 m height will be within the 3 dB beamwidth of the antenna at any distance greater than 2.47 m. Figure 7.2 shows the experiment scenario whereas Figure 7.3 shows the STFT results with the simulated and measured results. Again, it can be observed that the general shapes of the two plots and the Doppler velocity values correspond well to each other from the simulated and experimental results. From both plots, we observe that the highest velocity components are generated during the steps when the leg is moving. Also, if we think about a walking human subject in front of a radar, it is reasonable to assume that the strongest radar returns will come from the torso of the subject. The torso of the walking subject moves at almost constant velocity during the walking cycle. And in Figure 7.3, we do observe the highest intensity of signals around the 1 ms^{-1} velocity for both simulated and experimental data. Note that since there is no hand movement, the negative velocity components generated by the hands moving away from the radar are also absent.
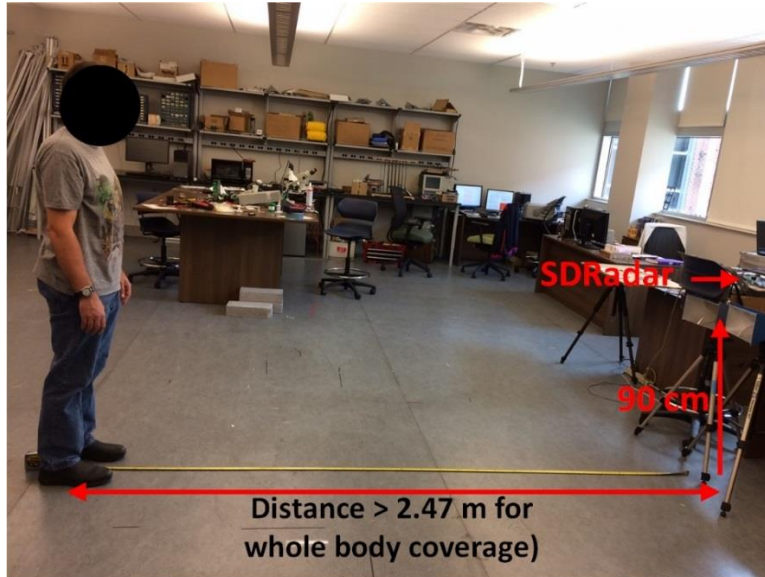
Figure 7.2: Gait analysis experiment setup with SDRadar for walking subject ensuring full-body coverage.
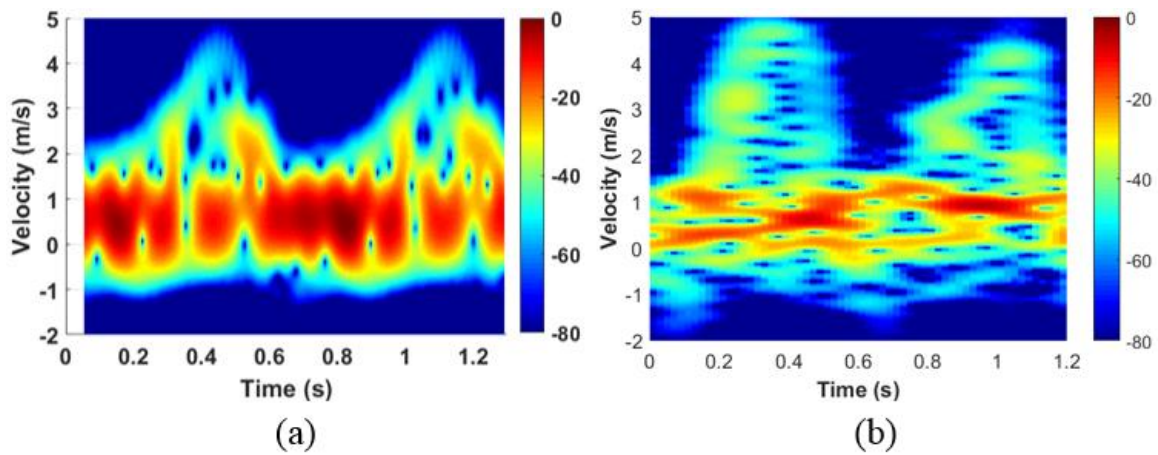
Figure 7.3: STFT spectrogram for a walking subject without moving hands (a) for EM simulated data, (b) measured data.

The next step is to add the effect of hand swinging in the motion by having the subject first walk with only the right-hand swinging and then with both hands swinging. Again, the subject started walking towards the radar from a 4.5 m distance away from the radar with a velocity of about 1 ms^{-1}. Figure 7.4 shows the STFT spectrograms from measured data for these two scenarios. Firstly, comparing the STFT spectrogram for walking with both arms swinging presented in Figure 7.4 (b) shows consistency with previously published research [2.1, 2.2, 2.20, 7.1], which is encouraging. We again observe that the strongest reflection component is around 1 ms^{-1} which represents the walking velocity. For one hand moving, we observe the negative velocity components during one step only, during the second step around 0.8 s to 1.1 s in Figure 7.4 (a). But for the walking with both hands moving case, we observe the negative Doppler frequencies generated by the two hands during both steps as we would expect.
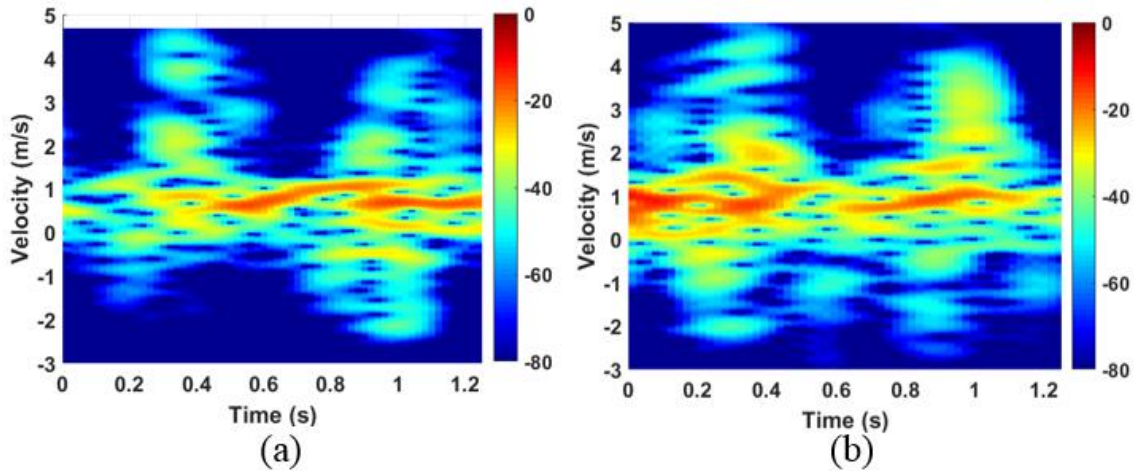
Figure 7.4: STFT spectrogram from measured data for a walking subject (a) with moving only one hand, (b) moving both hands.

122

7.1.2 1-D Block Results

Although we obtained the expected results from the STFT which provides us with some basic information about the motion, we cannot identify/track individual limb joints using the method. We utilized the 1-D block method described in the previous chapter to extract the individual limb velocities during motion for the same scenarios described above.

For the first scenario where the subject stood still and moved only one hand, we are interested in tracking the elbow and wrist trajectories from the simple periodic motion of the hand moving backward and forward. The degrees of freedom that we have are the sliding time window size and the order number. One of the limitations of the 1-D block method here is the difficulty in choosing these two parameters for optimum results. For initial estimation of the time window size, we can consider the half period of a particular motion in one direction. For example, if we look at the Boulic model results for moving hand scenario presented in Figure 7.5 (a), we observe that the elbow and wrist components have positive velocities for about 0.9 s and negative velocities for the remaining half of the total period. Thus, we initially start with a sliding time window of about 0.45 s and decrease them gradually as required. But at the same time, we need to estimate an initial value of the model order as well. In order to get that initial estimate, we can observe the plot of the singular values computed from the singular value decomposition (SVD) of the Hankel matrix for all time windows and identify a general knee of the composite plots. For low noise levels (as in the case of simulation), we can expect a sharp transition between the large and small singular values which provides a separation between the signal space and the noise space. Therefore, this transition point or knee can be used as a minimum estimate

123
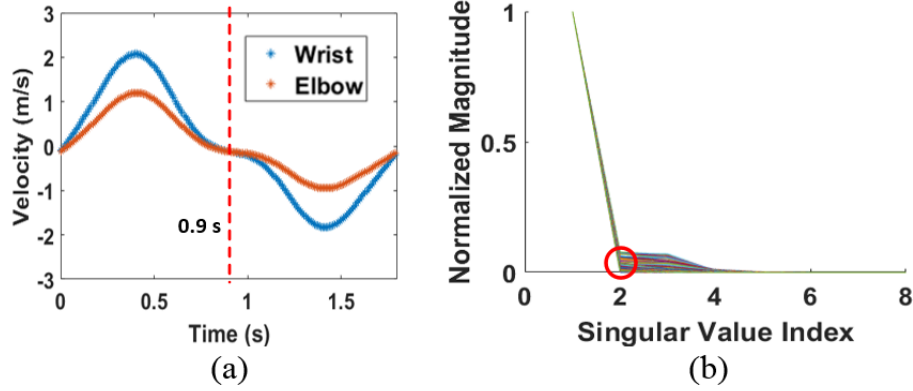
Figure 7.5: (a) Initial sliding time window size estimation by looking at the period of the limb motion in one direction and using half of that period. (b) Model order estimation using the singular value plots where the sharp transition is observed in index = 2.

of the number of signals embedded in the data known as the model order. For measured data, the noise levels can be high and the separation between weak signal and noise spaces may not be as well-defined as in a high SNR case making the model order estimation more difficult. Figure 7.5 (b) shows the singular value plots for the simulated data of the scenario. Considering the plots for all sliding windows, it can be observed that the knee is approximately located around index 2 which we use as the initial estimate.

Thus, we started the analysis with the respective sliding time window = 0.45 s and order = 2, decreased the time window gradually and incrementing the order by one at a time trying to attain good correspondence with the results from the Boulic model. Eventually the EM simulation and measurement data were both processed with model order = 4 and sliding time window of about 0.22 s in both cases. Each order (which represents a pole)

continuously and automatically tracks the same scatterer during the observed window, even when it intersects with other scatterers represented by other poles. For the hand swinging case, we are only interested in tracking the arm and the wrist, but the 1-D block was run with model order = 4. Thus, out of the 4 extracted features, the desired two trajectories need to be identified by observing the reference Boulic model motion of the limb joints being tracked. Figure 7.6 (a) and (b) show all the features extracted by the 1-D block method from simulated and measured data for the one hand swinging case. By observing the motion of the arm and wrist from the Boulic model given in Figure 7.5 (a), we can choose the extracted features that lie close to the Boulic model features, which in this case corresponds to order 1 and 2 only from the 1-D block results. Figure 7.7 shows the final results for the scenario with the results from Boulic model for side by side comparison.

(a)   (b)
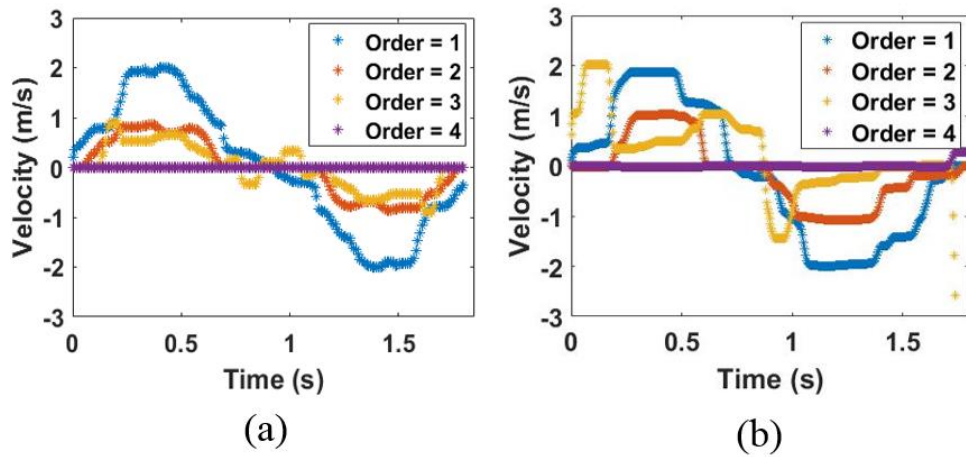
Figure 7.6: All four features extracted by the 1-D block method run with model order = 4 for right hand swinging case from (a) simulated, (b) measured data where the only features that correspond to the desired features from the Boulic model are given by order 1 and 2.
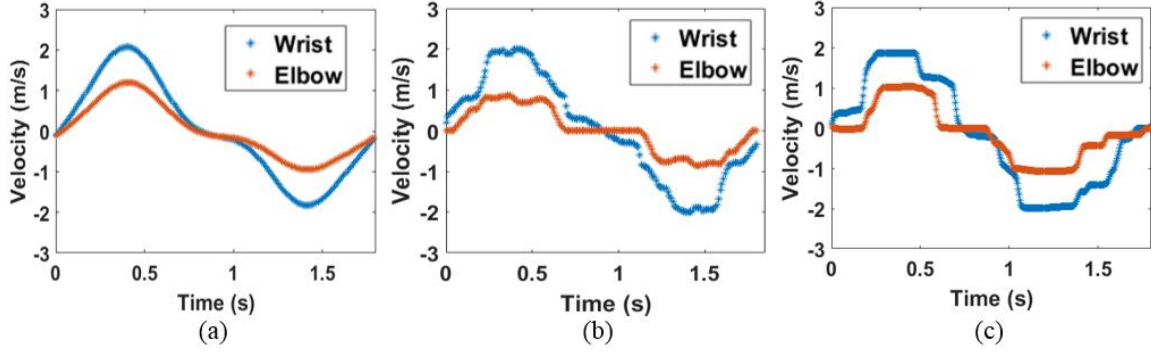
Figure 7.7: Final results of the one hand swinging case showing arm and wrist trajectories from (a) Boulic model, (b) 1-D block applied to EM simulated data, (c) 1-D block applied to measured data.

The next scenario was very similar where the subject sat on a chair and swung one leg while keeping the knee stationary with a view to track the ankle and calf. The initial estimation of the time window size and the order number was performed in a similar manner. The singular value plots for the EM simulated data for this scenario shows a knee at index $= 3$ as shown in Figure 7.8 (a). After starting with a time window of 0.45 s and order $= 3$, the optimized results were obtained for time window $= 0.2$ s and order $= 4$. Figure 7.8 (b-d) show the final results for this scenario extracted from 1-D block along with the Boulic model results. As it can be seen from Figures 7.7 and 7.8, there is a very good agreement between the two scenarios in terms of the extracted trajectories and velocities of the limb joints tracked.

The next scenario was a more complex case: walking without moving hands intended for tracking the lower body parts (toes, ankles, knees) and the torso. We initially looked at the
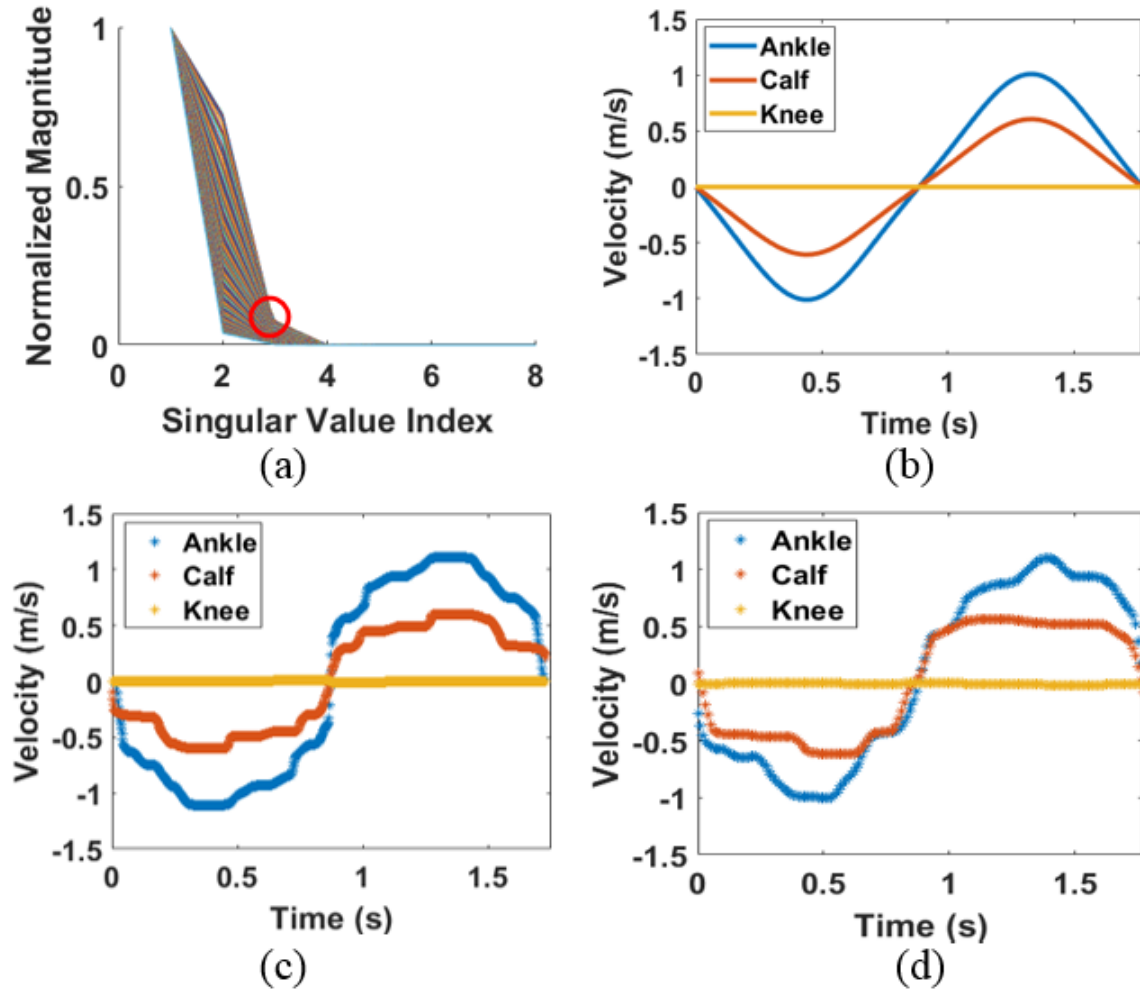
Figure 7.8: (a) Singular value plot from EM simulated data for swinging one leg showing knee at index = 3, (b) Boulic model for the scenario, (c) extracted results using 1-D block from simulated data, (d) 1-D block results for measured data.

Boulic model results as shown in Figure 7.9 (a) and chose a time window of 0.25 s according to the half period of one step in the motion. For the initial estimation of the model order, we again used the singular value plot using the simulated data and the knee was observed at index = 3 as seen in Figure 7.9 (b). But in this case, the total number of joints of interest was larger, so the model order was increased gradually to 6 to capture all the targeted joints and obtain a better match with the Boulic model trajectories. For the simulated data, only one superposition iteration was enough to extract all the desired trajectories with model order = 6 and time window of 0.18 s. However, for the experimental data, three superposition iterations were required, and the singular value plot method was not feasible to use here. The first iteration was for extracting the torso with model order = 3, second one for the toes and the ankles with model order = 10 and the final one for the knees with model order = 6, all with a time window of 0.18 s.
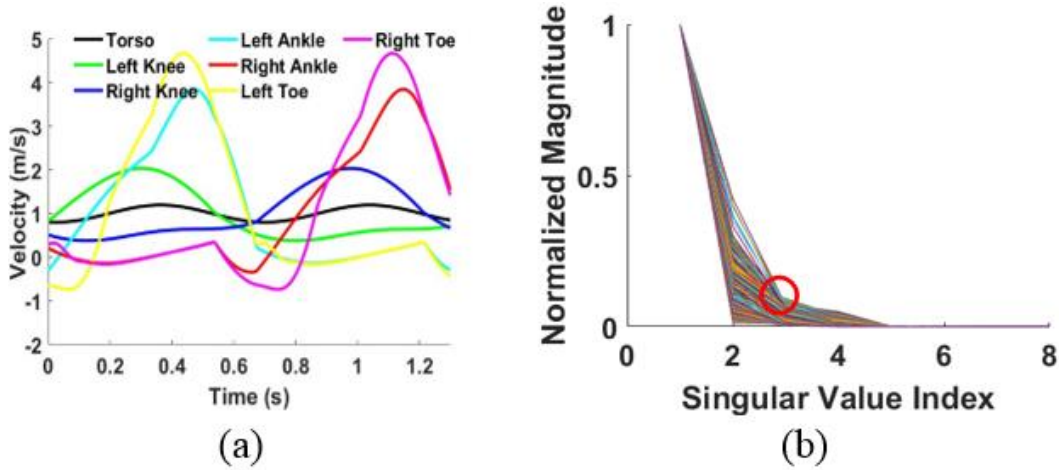
Figure 7.9: (a) Boulic model results for a walking subject with 1ms^{-1} velocity, (b) Singular value plot from EM simulated data for the same scenario showing a knee at index = 3.

Because the corresponding joints for both legs move with identical motion, the joints from one leg remain almost stationary, while the other leg moves and vice versa. The 1-D block processing method identifies each particular joint from both legs with one pole during motion. Thus, after identifying the features by comparing the motion features to the reference Boulic model motion, the left and right leg components can be separated as well. Figure 7.10 shows an example of this separation for the simulated data where the toes and ankles from both legs are identified by the 1-D block processing method with model orders 1 and 2, respectively. Since one leg is almost stationary while a dismount is in motion, the first half cycles of these motions are attributed to one leg movement whereas the second halves correspond to the other. Thus, we can separate the two leg components accordingly and identify them as left and right depending on the knowledge of the starting step. And since one leg moves while the other stays almost stationary, it is not necessary to track both legs at the same time. Figure 7.11 shows the simulated and measured results for the
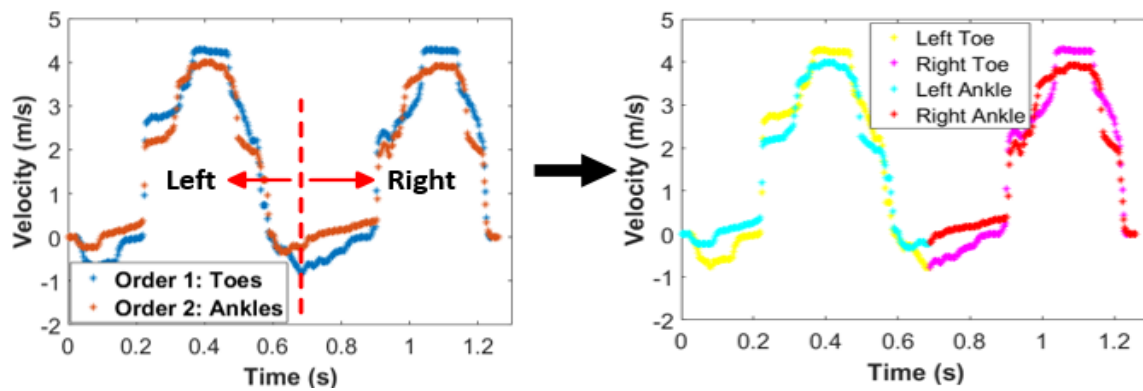
Figure 7.10: Left and right leg joints separation from the extracted features using simulated radar data.

129
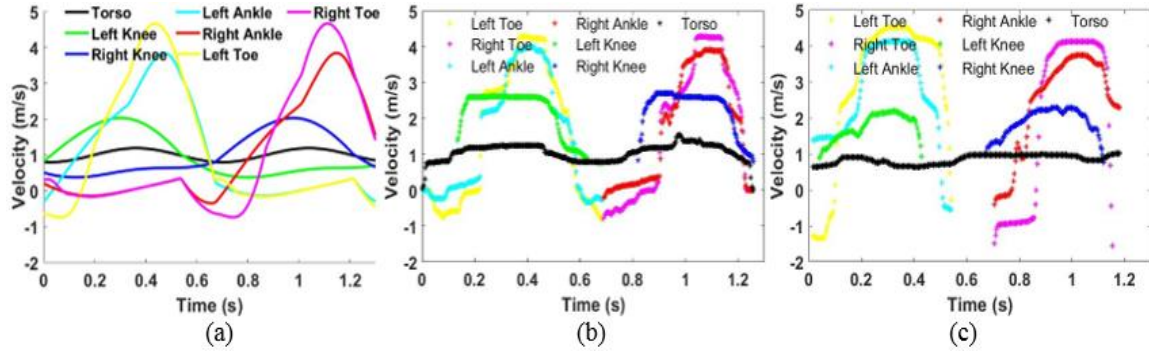
Figure 7.11: Tracking torso, toes, ankles and knees of a subject walking without hand motion (a) Boulic model, (b) extracted features using 1-D block with EM simulation data, and (c) extracted features using 1-D block with measured radar data.

scenario showing all the joints. Again, it can be observed that we can clearly track the desired limb joints both from the simulated and measured radar data.

The next step is to add the effect of hand swinging and investigate the possibility of tracking the feet, knees, hand(s) and the torso. For feature extraction from the measured data in both cases, three superposition iterations were considered to extract all the features from the experimental results. The first iteration gave the torso trajectory (with model order = 3), the second one extracted the feet (with model order = 10) and the third one provided the hand(s) and knee trajectories (with model order = 10), all with a sliding time window of 0.23 s. The left and right leg components can be separated using the approach described in the previous section, given that we do not need to track both legs at the same time due to one being almost stationary while the other moves. However, it is not the same case for the

130

hands. For a dismount walking with both hands swinging, the hands are always moving in opposite directions and have almost opposite motion of each other. As shown in the Boulic model results of this case presented in Figure 7.12 (c), when the right hand is at its maximum velocity point around 0.3 s, the left hand is almost at its minimum velocity point and vice versa. The 1-D block algorithm, thus, identifies the hands separately and extracts the individual motions of both hands throughout the whole walking cycle. Since the motion gets much more complex, it becomes more difficult to individually identify all the components (like the toes, ankles) in addition to the hands. This limitation is not really an outcome of using the superposition approach, but because the approach has been useful in identifying the toes, ankles, and knees separately when the motion does not involve the hands, as presented by Figure 7.11 (c). It can be observed from Figure 7.12 that there is a slight degradation of the tracking performance as the motion complexity increases, especially in tracking the hand motion; which is another limitation of this method. However, we still can clearly identify the trajectories of the limb joints of interest using the 1-D block algorithm and obtain consistent results with other reported works [2.6, 2.19, 2.39, 2.41] for the relative velocities of hands and legs while walking. A summary of the micro-Doppler maximum frequencies of the tracked parts of the proposed method and Boulic model is given in Table 7.1.
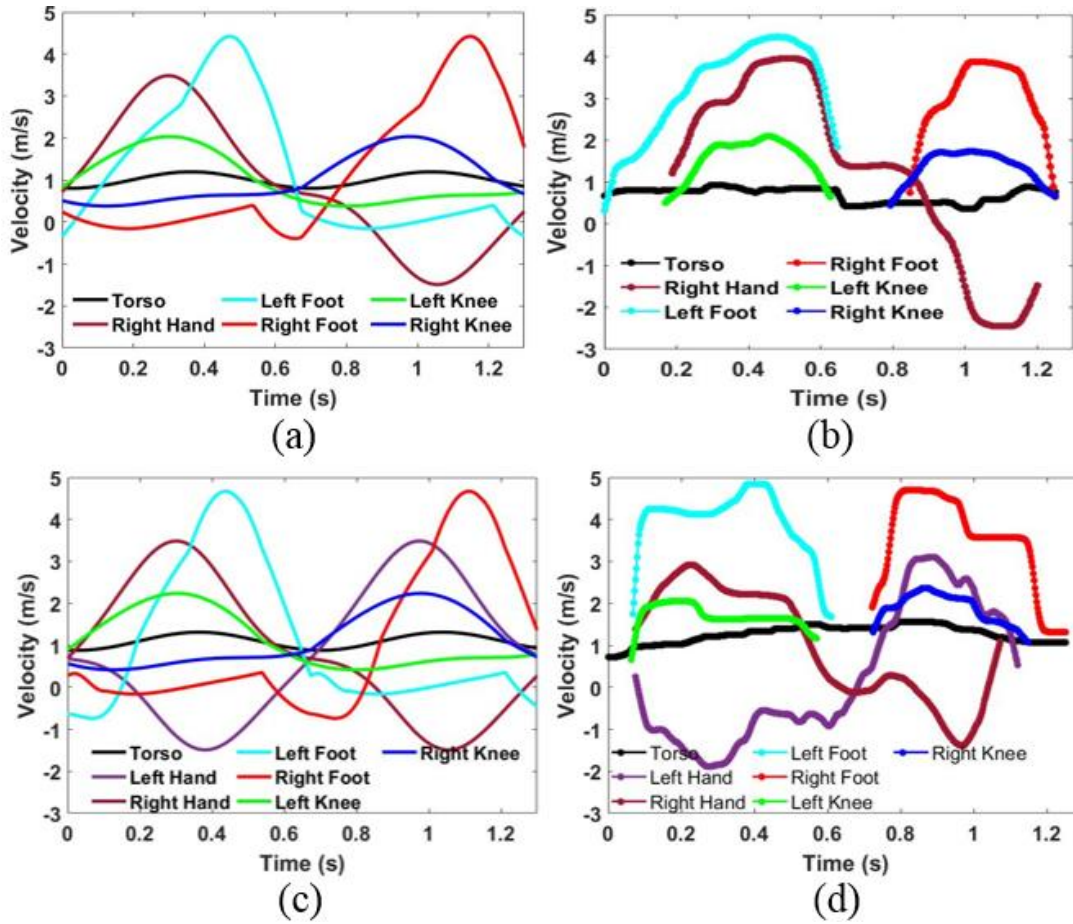
Figure 7.12: Tracking torso, legs and right hand for a subject walking with only right hand swinging (a) Boulic model, (b) extracted limb joint velocities from measured data using 1-D block method. (c) Boulic model, and (d) tracked limb joints from measured data using 1-D block for a subject walking at about 1.1 ms^{-1} with both hands swinging.

Table 7.1: Comparison of maximum velocities of the tracked parts from Boulic model and measured data.

Motion	Tracked Part	Max. Velocity Boulic (ms⁻¹)	Max. Velocity Measured (ms⁻¹)
Hand Swing	Arm	2.05/-2.05	1.90/-1.99
	Wrist	1.18/-1.18	1.04/-1.08
Leg Swing	Ankle	1.0/-1.0	1.1/-1.0
	Calf	0.6/-0.6	0.56/-0.61
Walking without moving hands	Toes	4.67	4.51
	Ankles	3.85	4.12
	Knees	2.04	2.28
	Torso	1.20	1.01
Walking with one hand swinging	Feet	4.43	4.47
	Knees	2.04	2.11
	Torso	1.20	0.93
	Hand	3.48	3.95
Walking with both hands swinging	Feet	4.67	4.84
	Knees	2.24	2.37
	Torso	1.31	1.50
	Hands	3.49	3.11

7.2 SFCW Radar

7.2.1 Results from Discrete Component System

Next, we evaluate the performance of extraction of the features using 1-D block from the data collected by the SFCW radar built using the commercially available components with the fast switching PLL as the signal generator. We utilized stepped frequency from 2-3 GHz with 20 MHz steps that would make the range resolution 15 cm and a maximum unambiguous range of 7.5 m. The transmitted power of the system was 8 dBm. The experiments that we considered were swinging one hand only, walking without moving hands and walking with moving both hands with similar experiment scenarios and maintaining similar velocities. In this case, we did not consider performing the EM simulations anymore. Since the EM analysis has to be performed at every frequency within the range, the already large problem becomes even larger and the computation time becomes proportionally larger. Figures 7.13-15 show the results from the three scenarios along with reporting the 1-D block parameters.

Next, we utilize the available bandwidth and the range resolution capabilities of the SFCW radar to perform a multi-person experiment. The experiment scenario is presented in Figure 7.16 (a) where two subjects are standing in front of the radar, one at 1.2 m distance and the other at 2.0 m distance. The subjects are symmetrically off-centered with respect to the radar boresight direction and the distance between the subjects is 0.6 m. Both subjects stay stationary and swing their right arm and the radar captures the motion from both targets. After collecting data, we can distinguish between the two subjects from the range profile

134
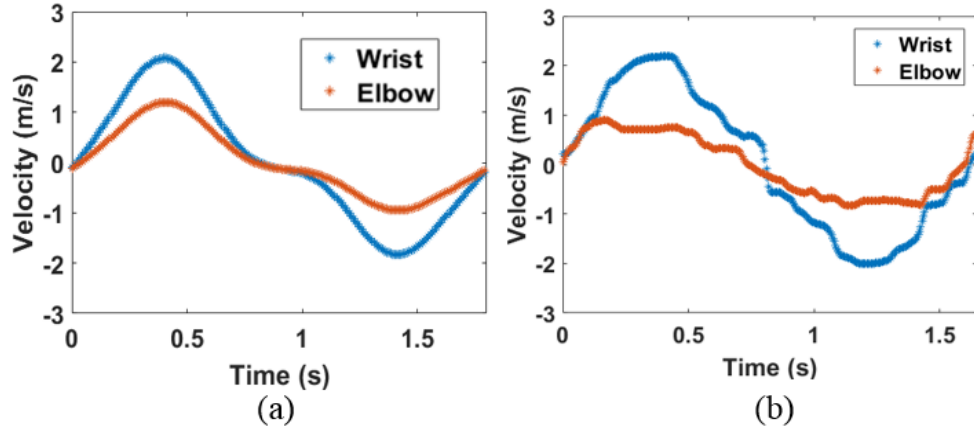
Figure 7.13: Wrist and elbow trajectory tracking for a subject swinging only one hand (a) Boulic model results, (b) results extracted by 1-D block using SFCW data with window size 0.2 s, and model order = 6.
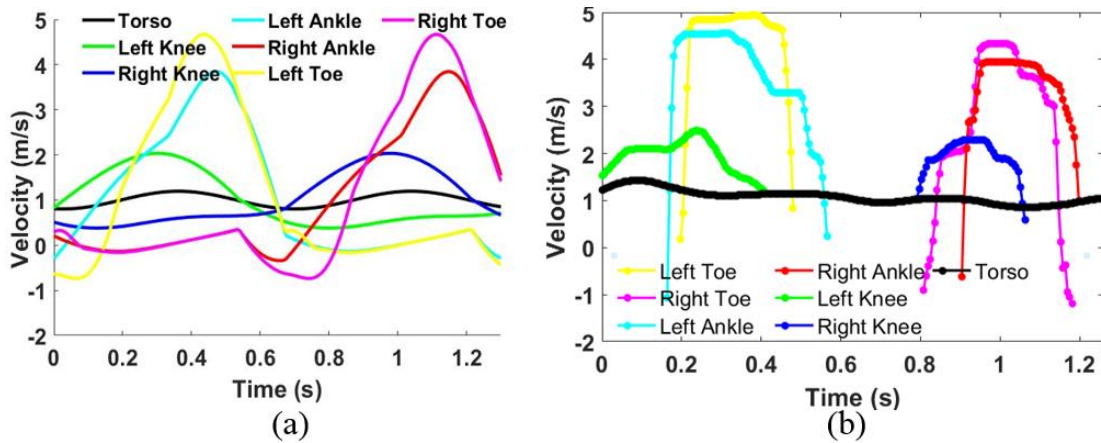
Figure 7.14: Trajectory tracking for a subject walking at 1 ms^{-1} velocity without moving hands (a) Boulic model results, (b) results extracted by 1-D block using SFCW data with window size 0.09 s, and three superposition iterations with order 4, 12 and 16.
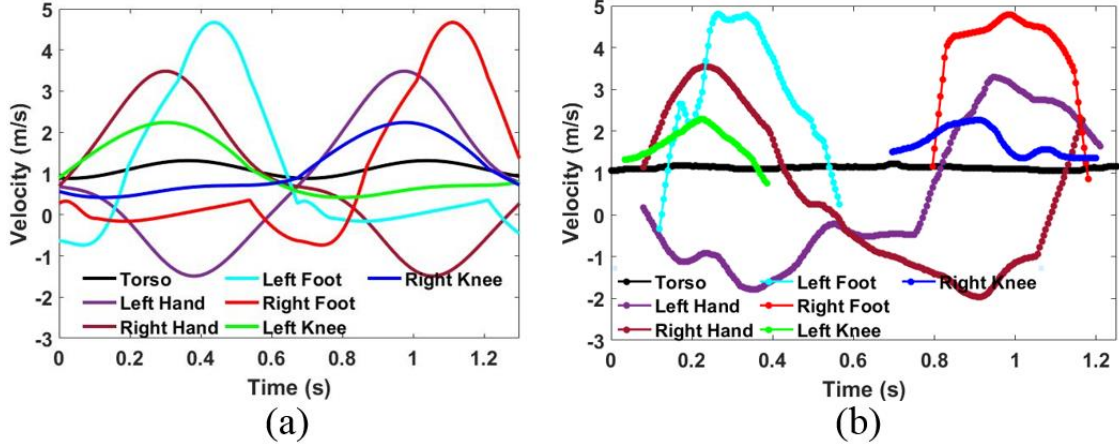
Figure 7.15: Limb joint trajectory tracking results for a subject walking at 1 ms^{-1} velocity while moving both hands (a) Boulic model, (b) extracted by 1-D block using SFCW data with window size 0.08 s, and three superposition iterations with order 4, 13 and 15.

as shown in Figure 7.16 (b). We can identify the range bin spans within which the movements of each subject are limited to and perform the 1-D block analysis using the respective spans. Figure 7.17 shows the extracted movement of the hands for the two subjects. We do observe that the there is some degradation in tracking the hand movement of the two subjects. This can be attributed to the mutual coupling created by the two subjects in the scene, as we observed before for simultaneous vital signs detection of two subjects [3.5]. Also, since we are distinguishing two subjects by the non-overlapping range bins, this method will not work when the two subjects are in the same range bin.
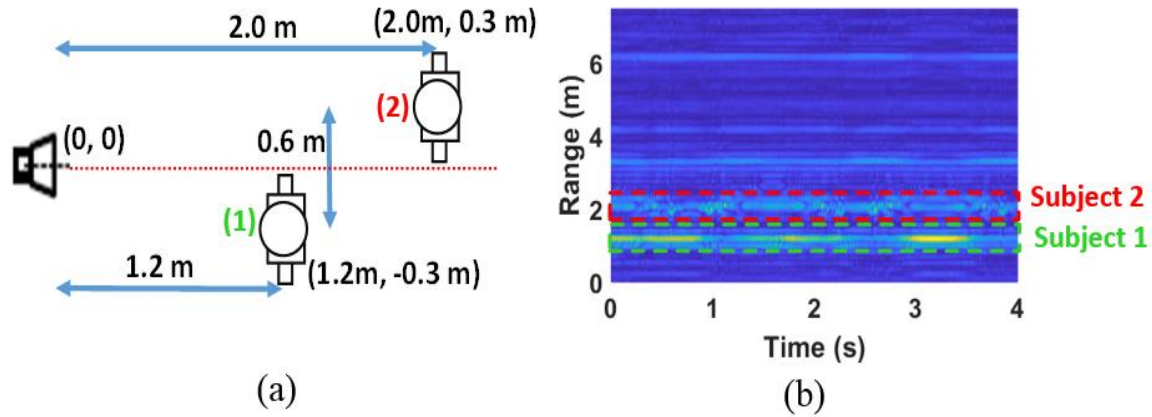
Figure 7.16: (a) Experiment scenario for multi-person motion analysis using SFCW radar system, (b) Extracted range profile identifying the two subjects and their movement ranges.
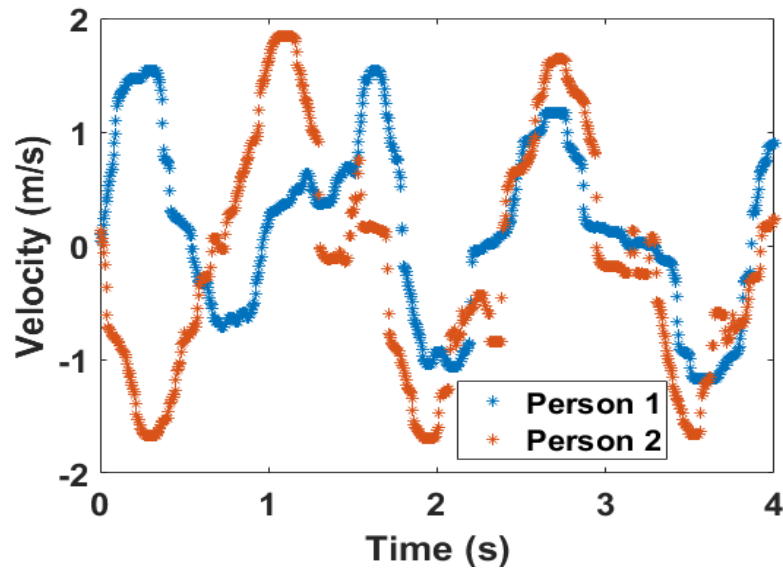
Figure 7.17: Extracted hand motion from 1-D block algorithm for the multi-subject motion analysis experiment.

7.2.2 Results from Hybrid System

We also performed gait analysis experiments with the hybrid system discussed in Chapter 6 using the same PLL system as the signal generator. But since the operating range of the radar front-end in this case was 3-4 GHz, we had to generate that range of frequencies from the PLL by changing the reference input signal to the PLL. Now, as discussed earlier in Chapter 1 and 2, the generated Doppler shift will depend on the radar operating frequency and the maximum velocity that can be detected by a 3-4 GH radar with PRF of 200 Hz is 4.3 ms^{-1}. Thus, for the walking experiment, we utilized a lower walking speed of around 0.8 ms^{-1} so that the maximum velocities generated by the toes are within that limit. Figure 7.18 and 7.19 present the feature extraction results of walking without moving hands and walking with moving both hands respectively.
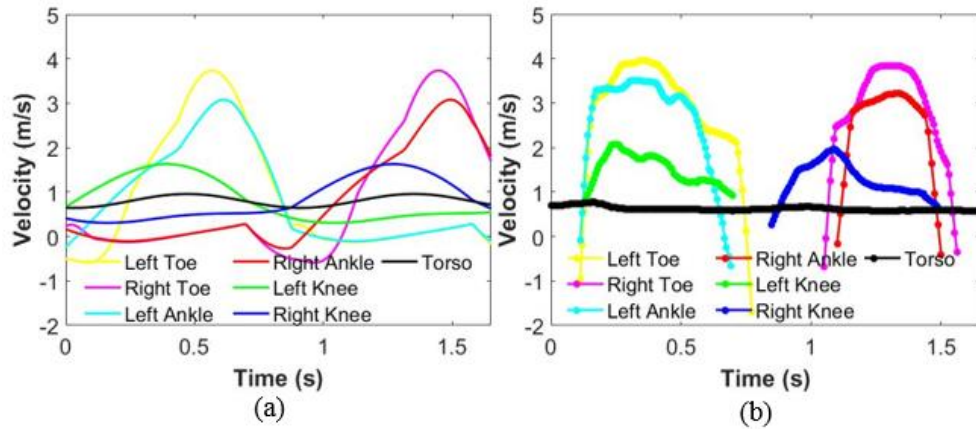
Figure 7.18: Trajectory tracking using the hybrid SFCW system for a subject walking at about 0.8 ms^{-1} velocity without moving hands (a) Boulic model results, (b) results extracted by 1-D block using SFCW data with window size 0.09 s, and three superposition iterations with order 4, 14 and 16.
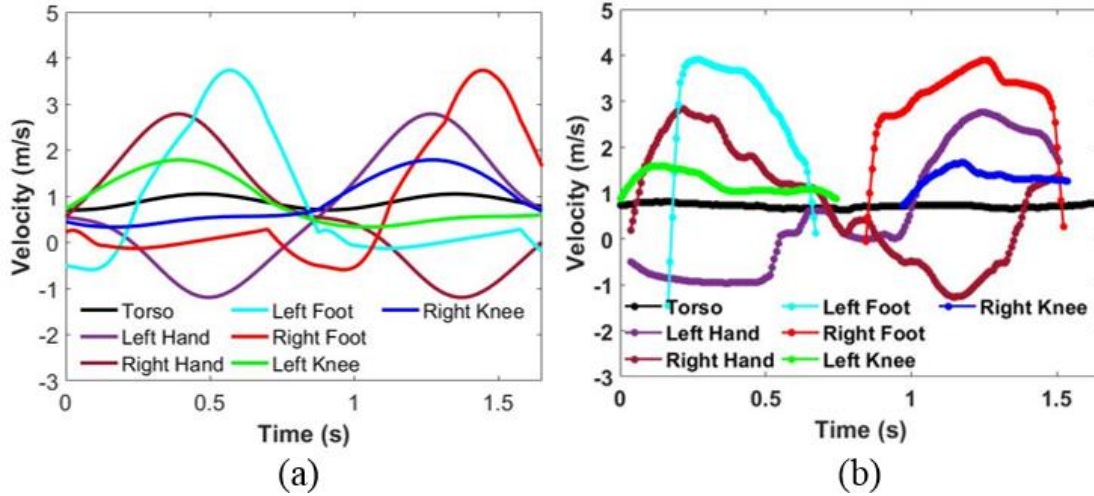
Figure 7.19: Gait analysis using the hybrid SFCW system for a subject walking at about 0.8 ms^{-1} velocity while moving both hands (a) Boulic model results, (b) results extracted by 1-D block using SFCW data with window size 0.09 s, and three superposition iterations with order 3, 13 and 13.

7.3 Discussion on the Gait Analysis Results

As seen from the results reported above, using the 1-D block method, we have been successful in detecting the desired limb joint motions from different simple and complex human motions using both CW and UWB radars. Although there was slight degradation when the walking motion involved the hands, but still we could identify the individual parts from both simulated and measured data from a normal laboratory environment. Figure 7.20 shows the results obtained in this work side by side with other reported work on limb joint tracking for a walking subject.

Figure 7.20: (a) Trajectory tracking results in this work for a walking subject moving at 1 ms^{-1} using CW and SFCW radars. (b) Gait analysis results for a walking subject reported in [2.19] using an 8.9–9.4 GHz SFCW radar where the extraction of the complete hand swing was not possible. (c) Motion analysis results reported in [2.39] where identification was done for the legs, hands and torso trajectories from simulated data of a walking subject, but results from measured data was difficult to interpret. (d) Analysis performed in [2.44] using simulated UWB radar data for identifying only the torso and lower body parts of a walking subject. (e) Gait analysis using UWB-IR radar [2.10] for a walking subject with velocity of 0.33 ms^{-1} showing the extraction of toes and torso only.
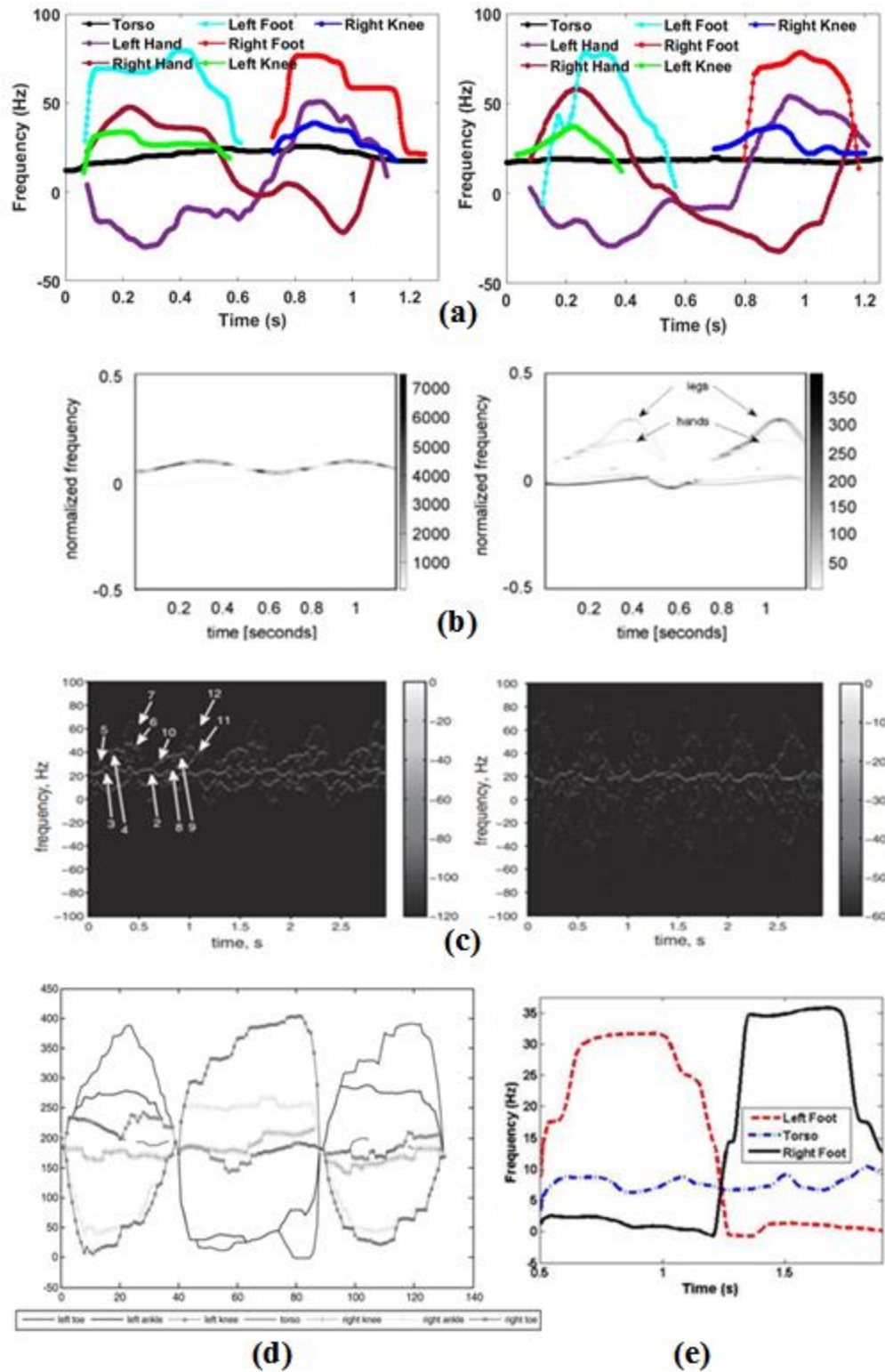
In spite of the success of the 1-D block method in extracting the individual limb-joints from a walking subject, the method does have some limitations. The initial estimation of the model order and the time window size becomes very complicated as the motion becomes more complex. Using the SVD method that we discussed in Chapter 6, we can separate between the signal space and the noise space by looking at the sharp transition in the SVD plots. But this is only true when the noise is low which the case for simulations is. In real experiments, the noise is higher along with external interference, thus the SVD plot cannot successfully separate the noise and the signal in that case.

Once we start with an initial model order, eventually the result is obtained for a model order that is typically larger than the number of limbs that we intend to track. Thus, we have to choose the appropriate features by comparing the extracted result with the reference model as described in previous sections. Although this reference motion can be estimated for typical human motion, in order to analyze a person with abnormal movement or with joint problems, the extracted results can be difficult to interpret. In addition, the algorithm is very sensitive to the model order and the time window and the change in behavior due to the change in these parameters is not always intuitive. This is especially true for the complex motion scenarios like walking. For example, if we go back to the experiment data for walking without moving hands scenario, we utilized three superposition iterations with order 3, 10 and 6 respectively with a time window of 0.18 s. The first iteration extracted the torso, the second provided the toes and ankles while the third extracted the knee trajectories. The results from the three iterations are presented in Figure 7.21 where the desired features from each iteration are highlighted. We have to identify the desired
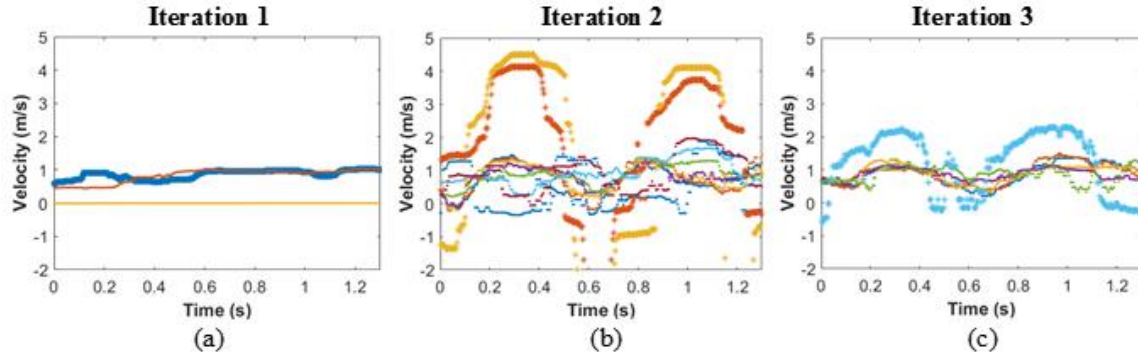
Figure 7.21: 1-D block extraction results from CW radar data for walking without moving hands showing the highlighted desired features along with all other features derived from the three iterations.

motions from each iteration individually which would be difficult without referring to the reference motion.

Now if we change the time window by about ± 10% but keeping the same model orders, the extraction results look very different and does not match well with the reference results as shown in Figure 7.22. Also, if we choose a slightly different model order, for example, 9 or 11 instead of 10 for the second iteration, that also impacts the extraction results from the second and third iteration significantly as shown in Figure 7.23. And this applies to other walking scenarios using both the CW and the SFCW radar data. Thus, we could not find a systematic way to choose the model order and time window for each experiment scenario, rather chose them through trial and error.
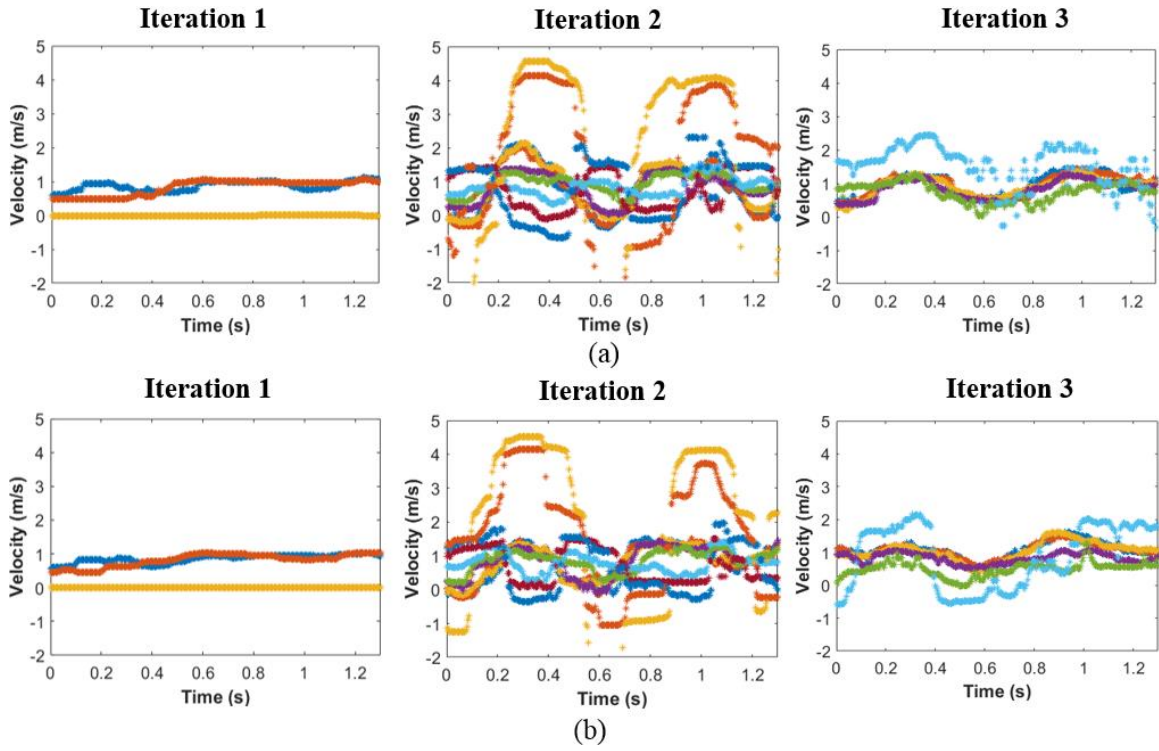
Figure 7.22: Impact of varying the time window size for the same scenario presented in Figure 7.21 with same model orders (3, 10 and 6) but with (a) about 10 % smaller time window (0.16 s) (b) about 10% larger time window (0.2 s).
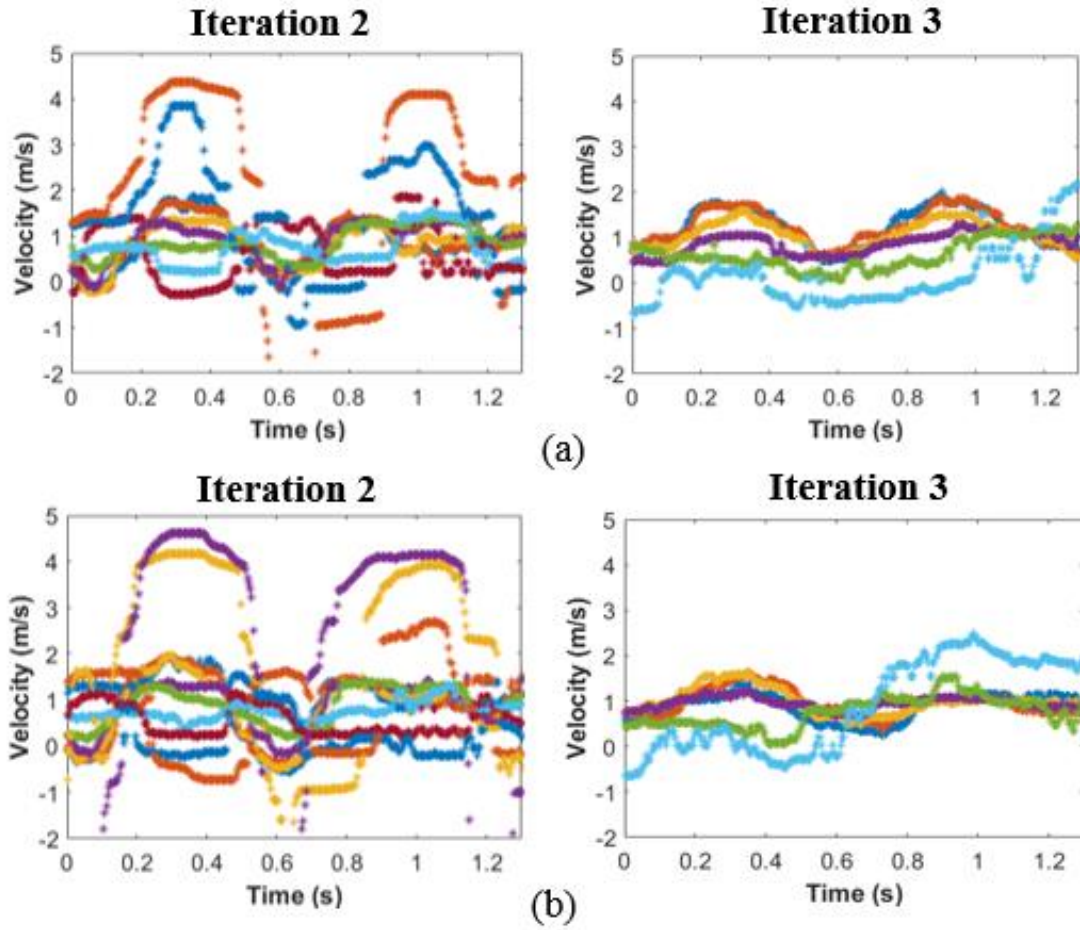
Figure 7.23: Impact of varying the model order for the same scenario presented in Figure 7.21 with same time window (0.18 s) and order = 3 and 6 for first and third iterations respectively but with (a) order = 9 for the second iteration and (b) order = 11 for the second iteration.

7.4 Vital Signs Detection

An added advantage of using radar systems for motion analysis is that it can be used for other applications such as vital signs detection. In that case, we do not really need a high PRF radar since the maximum frequency that we are trying to detect is less than 1.6 Hz which is the maximum range of human heart rate. Typically, we set the data collection period to 10 s to capture at least two cycles of respiration, which is assumed to be around 0.2 Hz. A shorter duration that captures slightly over one respiration cycle could also be adequate. We have successfully utilized the SDR as well as the PLL based system to detect human vital signs.

For the PLL based system, since the DDS has two independently working channels, we can operate the system as a multiple mode radar (MMR) incorporating the functions of both CW and SFCW Doppler radars rather than using separate platforms for each radar type. Use of the SFCW mode allows short-range SAR operation, and multi-subject tracking. Meanwhile, the CW mode based on Doppler operation enables long range remote triage. We implemented the system based on a very simple microcontroller-based approach where the DDS channels were independently configured using two pins on the microcontroller to provide either a CW signal or to step through a certain frequency range for SFCW operation. We even implemented a higher sensitivity mode where the signal to be transmitted is up-converted to higher frequency that would provide better resolution [7.2]. Two SPDT switches on both the transmitting and the receiving sides are used to choose between the up-conversion path or normal transmission path and the switches are

controlled by the microcontroller as well. The MMR system block diagram is shown in Figure 7.24.

For close range detection, we can have channel 1 and channel 2 step through 2-3 GHz and 3-4 GHz respectively with 20 MHz. This is equivalent to a 2 GHz bandwidth UWB SFCW radar and provides the highest available range resolution and precise localization of subjects with maximum unambiguous range of 7.5 m. We illuminate a subject sitting 0.75 m away from the radar with the transmitted signal. For reference, a commercial belt sensor and a pulse sensor were used for respiration and heart rate measurement respectively. As it can be observed from Figure 7.25 (a), even though the conventional system can detect

Figure 7.24: Block diagram of the Multi-Mode Radar showing the (1) signal generator, (2) RF front-end and (3) microcontroller. All the modes and the SPDT switches are controlled by the microcontroller.

147

the respiration rate clearly, there is no distinct peak for the heart rate which is in agreement with the results obtained in [7.3]. The percentage error calculated from the radar data compared to the reference belt sensor was 2.4%. We can operate the MMR in the higher sensitivity mode by controlling the microcontroller unit to switch the signal path and include a mixer for up-conversion to 8 GHz center frequency, as well as, a down-conversion mixer in the receiver chain. Up-converting to an even higher center frequency would allow us to achieve even higher sensitivity, and could be done in multiple conversion steps. Due to the use of the up-converted signal, the higher sensitivity mode is capable of providing distinct peaks for both the respiration rate and heart rate even using the simple conventional FFT algorithm as shown in Figure 7.25 (b). The percentage errors in the respiration and heart rate obtained from the radar were 1.95% and 0.33% respectively.

For long-range vital signs detection, we can switch the radar to operate in CW mode at 2.4 GHz with a transmitted power level of 12 dBm. An experiment was conducted to monitor a sedentary subject 20 m away from radar transceiver. The experiment setup is shown in Figure 7.26 (a). The data collected from the radar was processed and compared with the reference pulse sensor and the results are shown in Figure 7.26 (b). The detected heart rate with CW has an error rate less than 3% when compared with the reference sensor reading.

We have also successfully utilized the SDR system for vital signs experiments behind barriers as well. Since the developed SDR system allows the use of any frequency in its range of operation between 70 MHz to 6 GHz, we utilized it to investigate effect of changing the frequency for through barrier vital signs detection. For this scenario, a
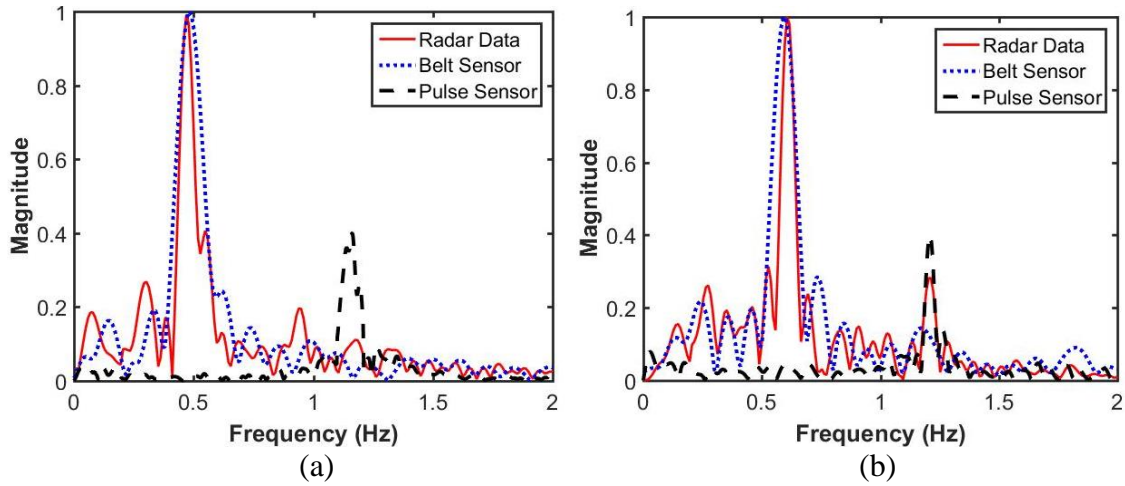
Figure 7.25: (a) Vital signs detection results using the conventional SFCW system operating between 2-4 GHz. (b) Vital signs detection from the same scenario using the up-converted stepped frequency signal of 7.5-8.5 GHz for higher sensitivity.
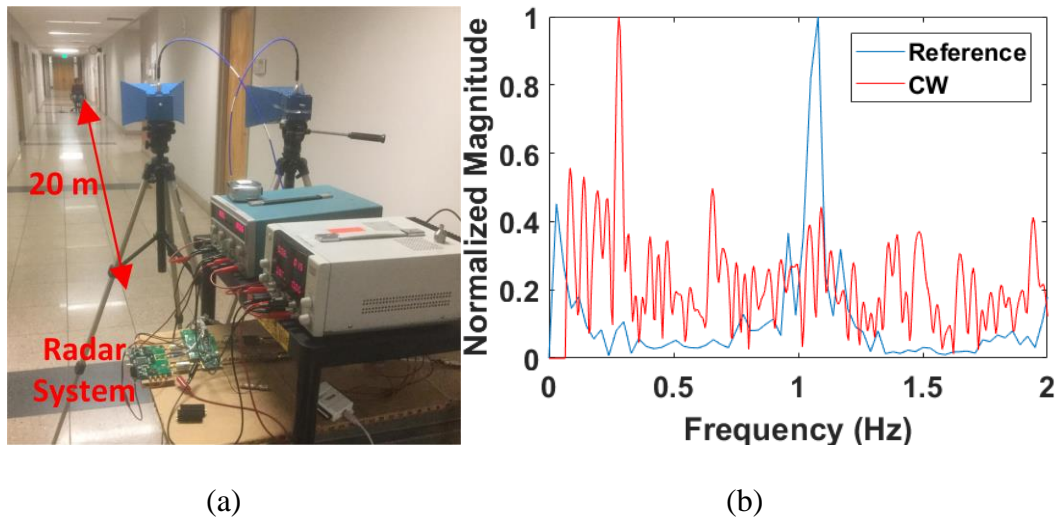
Figure 7.26: Long range vital signs detection using the CW mode (a) experiment setup, (b) vital signs spectrum.

149

subject's vital signs were measured through a barrier to emulate disaster rescue situations when subjects may be buried under rubble. Although the actual rubble in a disaster situation is a complex structure [7.4], for a simple proof of concept experiment, the barrier under which the subject was lying down, was emulated here with a wooden slab. Two horn antennas were pointed downwards from 1 m above, and 1.2 m away from the subject. The analysis was done first with a CW carrier frequency at 2.45 GHz, and later repeated with a lower carrier frequency of 915 MHz. An additional external variable gain amplifier was also used in this experiment to maintain the output power at 12 dBm for the two carrier frequencies. The subject wore two commercial contact sensors: a belt sensor (from NeuLog) for respiration, and a pulse sensor (from pulsesensor.com) for heart rate measurements. Our collaborators at CUA also modeled the entire scene including a human torso model, the infinite ground plane (concrete dielectric constant) and the wood layer. Additionally, the mutual coupling among these objects are accounted for with our full wave technique as mentioned in Chapter 6. Typically, using higher frequencies will lead to higher sensitivity as indicated by [5.1, 7.5]. However, if the subjects are behind a barrier we observed less sensitivity at 2.45 GHz compared to 915 MHz which is related to a relatively higher path attenuation in the presence of the barrier at 2.45 GHz. Figure 7.27 shows simulated and measured results for vital signs detection in the described scenario. As observed in Figure 7.27 (a) and (b), the heart rate peak is relatively stronger for both simulation and measurement in the 915 MHz case.
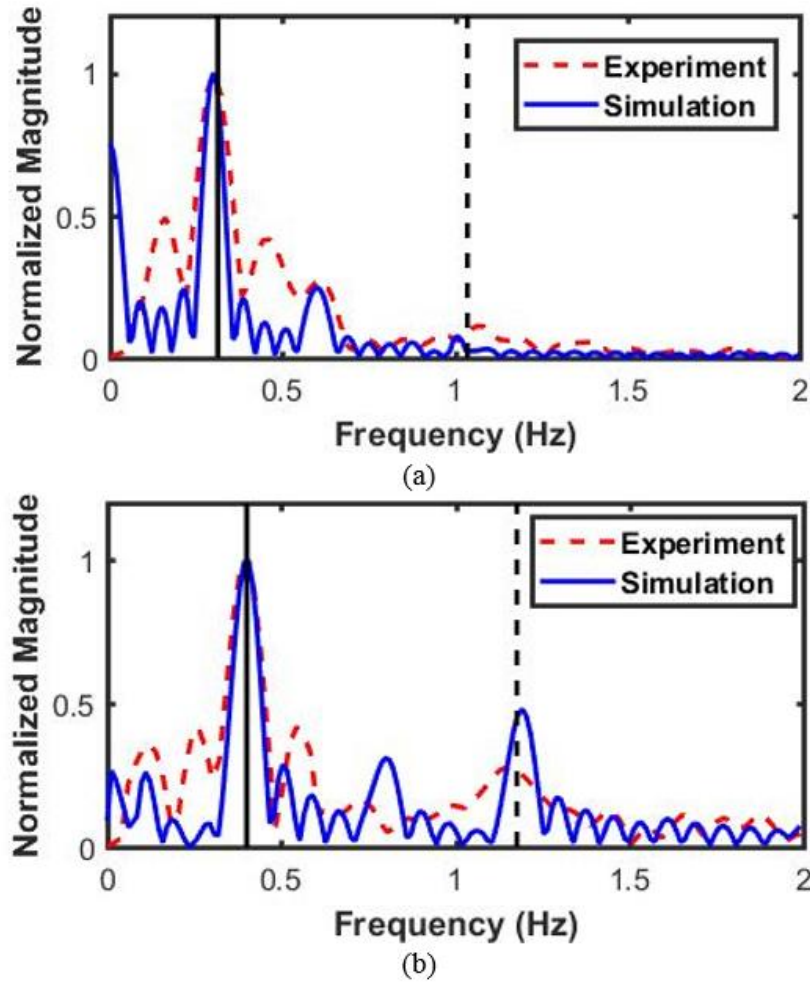
Figure 7.27: Vital signs spectrum for a subject lying under a wooden barrier at CW frequency (a) 2.45 GHz and (b) 915 MHz. The vertical solid and dashed black lines represent the contact sensor data for respiration and heart rate respectively.

7.5 Conclusion

This chapter presented the gait analysis results from the developed CW SDR, SFCW with commercial discrete components and the fast switching PLL and the hybrid SFCW system. The use of 1-D block allowed the extraction of all the desired features for a walking person from each of those systems. Side by side comparison with other previously reported works better performance in terms of tracking all the limb joints from the experimental data. Although the 1-D block method did present some limitations mainly related to the choice of the parameters, it can still be useful in many gait analysis applications such as treating patients with joint problems, motion classification, and so on. In addition to all these, the developed systems provide vital signs detection capabilities with good accuracy as well.

CHAPTER EIGHT
CONCLUSION AND FUTURE WORK

In collaboration with MITLL, CUA, and Lab partners (Farnaz, Ren, Sabikun), we have investigated non-contact human motion using radar techniques in this dissertation, including 1) implementation of fast switching SFCW system capable of performing gait analysis experiments, 2) investigation of use of software defined radars as flexible radar hardware platform, 3) design of radar front-end components on chip with a view to the implementation of an eventual radar system on chip, and 4) use of signal processing algorithm that can track individual limb joints from a human motion. We were eventually successful in implementing a combination of hardware and software methods that was capable of remotely performing gait analysis for simple human motions like swinging one hand or leg as well as complex motions like walking. The accomplishments of this work are summarized below:

8.1 Accomplishments

Firstly a stepped-frequency continuous wave radar with 200 Hz pulse repetition frequency is implemented in collaboration with Farnaz that is capable of unambiguously detecting velocities of up to 6 ms^{-1} operating within the 2-3 GHz band. The system utilized a fast switching PLL scheme to achieve the high PRF while maintaining the implementation cost low.

Next, a thorough investigation is performed to implement a software defined radar system that provides features like frequency tunability, small size, enhanced baseband signal handling capabilities and the lack of need for any external local oscillator signal sources. Using the SDR system, we implemented a tunable CW radar as well as a SFCW radar capable of operating at any frequency range within 70 MHz to 6 GHz. Although we could not make the PRF of the SFCW mode high enough for gait analysis, we were successful in using the platform in the CW mode to perform motion analysis experiments.

With a goal to making an overall compact UWB radar system, we designed the radar front-end components like the amplifier, power divider, mixer on chip using GaAs HBT and HEMT fabrication processes sponsored by Qorvo. The evaluation boards of the individual components were connected using co-axial cables to implement a hybrid radar system capable of operating within 3-4 GHz band, which could be easily integrated into a single printed circuit board.

Use of the full wave electromagnetic (EM) simulated motion model developed by CUA for the validation of initial hardware prototype and signal processing algorithm. The emulated EM model was useful for obtaining a clean set of repeatable reference data that could take different realistic settings into account such as body shape and material, noise, ground reflection, and parts interference.

Utilization of 1-D block method, a signal processing algorithm developed by our collaborators at MITLL to extract the velocities of different limb-joints in motion. Using the algorithm, we were successful in tracking the desired organs using data collected from

154

both CW and UWB system operating in typical non-controlled environment. Capability of utilizing CW radar data could pave the way for the utilization of low cost Doppler radars for performing gait analysis, while use of UWB radars can enable simultaneous multi-person tracking.

In addition to performing gait analysis, we utilized the implemented hardware system to detect human vital signs. The flexible and tunable software-defined radar allowed the investigation of the effect of switching the operating frequency for through barrier vital signs detection. We also implemented a multi-mode radar that can provide high sensitivity and long distance vital signs detection capabilities by switching operating modes and frequencies.

8.2 List of Publications

Journals:

• **F. Quaiyum**, N. Tran, J. E. Piou, O. Kilic, A. E Fathy, "Non-Contact Human Gait Analysis and Limb Joint Tracking Using Doppler Radar", accepted for publication in *IEEE Journal of Electromagnetics, RF, and Microwaves in Medicine and Biology*, November. 2018.

• **F. Quaiyum**, N. Tran, T. Phan, P. Theilmann, A. E. Fathy, O. Kilic, "Electromagnetic Modeling of Vital Sign Detection and Human Motion Sensing Validated by Non-Contact Radar Measurements", *IEEE Journal of Electromagnetics, RF, and Microwaves in Medicine and Biology*, Mar. 2018.

• S. Nahar, T. Phan, **F. Quaiyum**, L. Ren, A. E. Fathy, O. Kilic, "An Electromagnetic Model of Human Vital Signs Detection and Its Experimental Validation", *IEEE Journal on Emerging and Selected Topics in Circuits and Systems*, Jun. 2018.

Conference Paper:

• **F. Quaiyum**, L. Ren, S. Nahar, F. Foroughian, A. E. Fathy, "Development of a Reconfigurable Low Cost Multi-Mode Radar System for Contactless Vital Signs Detection", *2017 International Microwave Symposium (IMS)*, Honolulu, HI, Jun. 2017.

Others:

J: R. Kazemi, J. Palmer, **F. Quaiyum**, A. E. Fathy, "A Steerable Miniaturized Printed Quadrifilar Helical Array Antenna Using Digital Phase Shifters for BGAN/GPS Applications", *IET Microwaves, Antennas & Propagation*, Jan. 2018.

C1: A. E. Fathy, O. Kilic, L. Ren, N. Tran, T. V. Dai, F. F. Foroughian, **F. Quaiyum**, "Continuous Long Term Patient Motion Monitoring Using Ultra Wide Band Radar", 2018 *IEEE International Symposium on APS/URSI*, Boston, MA, Jul. 2018.

C2: F. Quaiyum, R. Kazemi, A. E. Fathy, "Phase Shifter Control Scheme Implementation for Steerable/Adaptive L-Band Phased Arrays", *2017 National Radio Science Meeting*, Boulder, CO, Jan. 2017.

C3: S. Cochran, **F. Quaiyum**, A. E. Fathy, D. Costinett, S. Yang, "A GaN-based Synchronous Rectifier for WPT Receivers with Reduced THD", *IEEE PELS Workshop on Emerging Technologies: Wireless Power*, Oak Ridge, TN, Oct. 2016.

To conclude the work, using the developed software and hardware platform, we were able to remotely analyze the motion of different body parts for different movements. We collected data from three different systems: the SDR operating in CW mode, SFCW implemented using discrete components and hybrid SFCW system using custom-designed circuits and were successful in tracking the desired body parts using each system through the 1-D block algorithm. Monitoring individual parts for simple motions was relatively straightforward, but as the motion got more complicated, i.e. walking while moving hands, it became progressively harder to track, and the parameter selection for the 1-D block method became less intuitive. It was difficult to simultaneously track all limbs, especially the hands in particular. Although the 1-D block method tracked individual scatterers automatically according to the selected order number, it did need to refer to the Boulic/EM model reference data to identify which scatterer represents which limb joint. That reference motion data can be obtained by running EM simulations of the motions or using other sophisticated method like using cameras or other imaging techniques for new "not-so-normal-gait" analysis. The extracted features from the measured data showed some discrepancy in comparison with the results from simulation and Boulic model. But even if the exact joint movements are not available, the method could still be accurate enough so that important changes in repeated measurements can be obtained which can be medically useful. In real scenarios, performing statistical analysis on repetitive measurements can help achieve more accurate results. Side by side comparison with previously published work demonstrated improved organ tracking performance for a walking human from both

157

our CW and UWB system. We also demonstrated the suitability of the developed hardware systems for another relevant application: vital signs detection.

8.3 Direction of Future Work

1. Although we were able to implement a SFCW system using the SDR platform, it could not provide high enough pulse repetition frequency to be suitable for use in gait analysis. Thus, there is scope of research for investigating other SDR techniques for fast frequency switching that can realize a flexible, portable and self-contained system that can operate in both CW and SFCW mode for gait analysis.

2. We implemented a hybrid radar system using custom designed components but the system was not an integrated solution. The immediate next step can be populating all the individual ICs in a single printed circuit board whereas the final step will be the integration of all the components into a single chip.

3. We faced some issues in choosing the optimum parameters for the 1-D block algorithm while analyzing walking motion. Further optimization of the algorithm along with integrating capabilities such as machine learning techniques and pattern recognition can be very useful for analyzing these motion in a more automatic manner without requiring user inputs.

4. For the multi-person experiments, we currently distinguish the subjects according to the respective range bins and perform the analysis individually. But we did not perform

158

any experiments where the subjects overlap in the range direction or their elapsed ranges cross over. Thus, there is scope of research in such experiments as well to make the system truly suitable for any multi-person scenario.

5. Analysis of faster moving objects like a subject running or jogging on a treadmill is still an open question. Such analysis can extend the application of this research for athlete performance evaluation as well.

LIST OF REFERENCES

[1.1]   J. K. Aggarwal, Q. Cai, "Human Motion Analysis: A Review," Computer Vision and Image Understanding, vol. 73, no. 3, 1999, pp 428-440.

[1.2]   D. Gouwanda, et al., "Emerging Trends of Body-Mounted Sensors in Sports and Human Gait Analysis," in 4th Kuala Lumpur International Conference on Biomedical Engineering, 2008, IFMBE Proceedings, vol. 21, pp. 715-718.

[1.3]   D. H. Sutherland, "The evolution of clinical gait analysis part I: Kinesiological EMG," Gait Posture, vol. 14, no. 1, 2001, pp. 61–70.

[1.4]   D. H. Sutherland, "The evolution of clinical gait analysis Part II kinematics," Gait Posture, vol. 16, no. 2, 2002, pp. 159–179.

[1.5]   D. H. Sutherland, "The evolution of clinical gait analysis part III—kinetics and energy assessment," Gait Posture, vol. 21, no. 4, 2005, pp. 447–461.

[1.6]   L. Wang, et al., "Silhouette analysis-based gait recognition for human identification," IEEE Trans. Pattern Anal. Mach. Intell., vol. 25, no. 12, 2003, pp. 1505–1518.

[1.7]   B. Najafi, et al., "Ambulatory system for human motion analysis using a kinematic sensor: monitoring of daily physical activity in the elderly," IEEE Trans. Biomed. Eng., vol. 50, no. 6, pp. 711-723, June 2003.

[1.8]   D.M Gavrila, "The Visual Analysis of Human Movement: A Survey," Computer Vision and Image Understanding, vol. 73, no. 1, 1999, pp 82-98.

[1.9]   Z. Yu, Y. Nakamura, "Smart Meeting Systems: A Survey of State-of-the-Art and Open Issues," ACM Computing Surveys, vol. 42, no. 2, pp. 8, 2010.

[1.10] Y. Wahab, N. A. Bakar, "Gait Analysis Measurement for Sport Application Based on Ultrasonic System," Proceedings of 2011 IEEE 15th International Symposium on Consumer Electronics (ISCE), Singapore, June 2011, pp. 20–24.

[1.11] L. Middleton, et al., "A Floor Sensor System for Gait Recognition," Proceedings of 2005 4th IEEE Workshop on Automatic Identification Advanced Technologies, Buffalo, NY, USA, October 2005, pp. 171–176.

[1.12] W. Kusakunniran, et al., "Support Vector Regression for Multi-View Gait Recognition Based on Local Motion Feature Selection," Proceedings of 2010 IEEE Conference on Computer Vision and Pattern Recognition (CVPR), San Francisco, CA, USA, June 2010, pp. 974–981.

[1.13] A. M. Howell, "Kinetic gait analysis using a low-cost insole," IEEE Trans. Biomed. Eng., vol. 60, no. 12, 2013, pp. 3284–3290.

[1.14] A. Salarian, et al., "Gait assessment in Parkinson's disease: Toward an ambulatory system for long-term monitoring," IEEE Trans. Biomed. Eng. vol. 51, no. 8, pp. 1434–1443, Aug. 2004.

[1.15] M. Whittle, "Gait analysis: An introduction" Edinburgh: Butterworth-Heinemann, 2007.

[1.16]   A. Muro-de-la-Herran, B. Garcia-Zapirain, A. Mendez-Zorrilla, "Gait analysis methods: an overview of wearable and non-wearable systems, highlighting clinical applications" Sensors (Basel, Switzerland), 2014, 14(2), pp. 3362-3394.

[1.17] A. N. M. Gomatam, S. Sasi, "Multimodal gait recognition based on stereo vision and 3D template matching" CISST, 2004, pp. 405–410.

[1.18] S. C. White, D. A. Winter, "Predicting muscle forces in gait from EMG signals and musculotendon kinematics" J. Electromyogr. Kinesiol, 1992, vol. 2, pp. 217–231.

[1.19] D. C. Kerrigan, M. K. Todd, U. D, Croce, L. A. Lipsitz, J. J. Collins, "Biomechanical gait alterations independent of speed in the healthy elderly: Evidence for specific limiting impairments" Arch. Phys. Med. Rehabil. 1998, vol. 79, pp. 317–322.

[1.20] H. Stolze, S. Klebe, G. Petersen, J. Raethjen, R. Wenzelburger, K. Witt, G. Deuschl, "Typical features of cerebellar ataxic gait" J. Neurol. Neurosurg. Psychiatry, 2002, vol. 73, pp. 310–312.

[1.21] J. M. Garcia-Rubia, O. Kilic, V. Dang, Q. M. Nguyen, and N. Tran, "Analysis of Moving Human Micro-Doppler Signature in Forest Environments," Progress In Electromagnetics Research, Vol. 148, 1-14, 2014.

[1.22] M. I. Skolnik, "Introduction to Radar Systems" McGraw-Hill, 1981. Pages 11, 56.

[1.23] M. Mercuri, D. Schreurs and P. Leroux, "SFCW microwave radar for in-door fall detection" 2012 IEEE Topical Conference on Biomedical Wireless Technologies, Networks, and Sensing Systems (BioWireleSS), Santa Clara, CA, 2012, pp. 53-56.

[1.24] J. D. Taylor, "Ultra-wideband Radar Technology" CRC Press, 2000. Pages 17.

[1.25] M. Mercuri, "Development of Contactless Health Monitoring Sensors and Integration in Wireless Sensor Networks," Ph.D. Dissertation, KU Leuven, 2015.

[2.1] J. L. Geisheimer, W. S. Marshall and E. Greneker, "A continuous-wave (CW) radar for gait analysis," Conference Record of Thirty-Fifth Asilomar Conference on Signals, Systems and Computers (Cat.No.01CH37256), Pacific Grove, CA, USA, 2001, pp. 834-838, vol.1.

[2.2] M. Otero, "Application of a continuous wave radar for human gait recognition," in Proc. SPIE, 2005, pp. 538-548.

[2.3] J. M. Muñoz-Ferreras, Z. Peng, Y. Tang, R. Gómez-García, D. Liang and C. Li, "Short-Range Doppler-Radar Signatures from Industrial Wind Turbines: Theory, Simulations, and Measurements," in IEEE Transactions on Instrumentation and Measurement, vol. 65, no. 9, pp. 2108-2119, Sept. 2016.

[2.4] A. Zhu et al., "Indoor Localization for Passive Moving Objects Based on a Redundant SIMO Radar Sensor," in IEEE Journal on Emerging and Selected Topics in Circuits and Systems, vol. 8, no. 2, pp. 271-279, June 2018.

[2.5] Q. Lv et al., "High Dynamic-Range Motion Imaging Based on Linearized Doppler Radar Sensor," in IEEE Transactions on Microwave Theory and Techniques, vol. 62, no. 9, pp. 1837-1846, Sept. 2014.

[2.6] V. C. Chen, "Detection and analysis of human motion by radar," in IEEE Radar Conference, Rome, Italy, 2008.

[2.7] C. Gu, et al., "Accurate Respiration Measurement using DC-coupled Continuous-wave Radar Sensor for Motion-adaptive Cancer Radiotherapy," IEEE Trans. Biomed. Eng., vol. 59, no. 11, pp. 3117-3123, Nov. 2012.

[2.8] A. Singh et al. "Data-based Quadrature Imbalance Compensation for a CW Doppler Radar System," IEEE Trans. Microw. Theory Techn., vol. 61, no. 4, pp. 1718-1724, Apr. 2013.

[2.9] Y. Wang, Q. Liu, and A. E. Fathy, "CW and pulse–Doppler radar processing based on FPGA for human sensing applications," IEEE Transactions on Geoscience and Remote Sensing, vol. 51, no. 5, pp. 3097-3107, 2013.

[2.10] L. Ren et al., "Short-Time State-Space Method for Micro-Doppler Identification of Walking Subject Using UWB Impulse Doppler Radar," in IEEE Transactions on Microwave Theory and Techniques, doi: 10.1109/TMTT.2018.2829523.

[2.11] Y. Tang, J. Wang and C. Li, "Short-range indoor localization using a hybrid doppler-UWB system," 2017 IEEE MTT-S International Microwave Symposium (IMS), Honolulu, HI, 2017, pp. 1011-1014.

[2.12] DWM1000 datasheet from DecaWave.

[2.13] IPS-154_V4.4 datasheet from InnoSenT.

[2.14] N. Maaref, et al., "A Study of UWB FM-CW Radar for the Detection of Human Beings in Motion Inside a Building," IEEE Transactions on Geoscience and Remote Sensing, vol. 47, no. 5, pp. 1297-1300, May 2009.

[2.15] G. Wang, et al., "A hybrid FMCW-interferometry radar for indoor precise positioning and versatile life activity monitoring," IEEE Transactions on Microwave Theory and Techniques, vol. 62, no. 11, pp. 2812-2822, 2014.

[2.16] G. Greneker, "Very low cost stand-off suicide bomber detection system using human gait analysis to screen potential bomb carrying individuals," Proc. SPIE, Radar Sensor Technology IX, May 2005.

[2.17] Z. Peng, C. Li, J. M. Muñoz-Ferreras and R. Gómez-García, "An FMCW radar sensor for human gesture recognition in the presence of multiple targets," 2017 First IEEE MTT-S International Microwave Bio Conference (IMBIOC), Gothenburg, 2017, pp. 1-3.

[2.18] B. Lu, Q. Song, Z. Zhou and H. Wang, "A SFCW radar for through wall imaging and motion detection," 2011 8th European Radar Conference, Manchester, 2011, pp. 325-328.

[2.19] T. Thayaparan, L. Stanković, and I. Djurović, "Micro-Doppler-based target detection and feature extraction in indoor and outdoor environments," Journal of the Franklin Institute, vol. 345, no. 6, pp. 700-722, 2008.

[2.20] V. C. Chen, et al., "Micro-Doppler effect in radar: phenomenon, model, and simulation study," IEEE Transactions on Aerospace and Electronic Systems, vol. 42, no. 1, pp. 2-21, Jan. 2006.

[2.21] F. Quaiyum, et al., "Electromagnetic Modeling of Vital Sign Detection and Human Motion Sensing Validated by Noncontact Radar Measurements," in IEEE Journal of Electromagnetics, RF and Microwaves in Medicine and Biology, vol. 2, no. 1, pp. 40-47, March 2018.

[2.22] D. Tahmoush and J. Silvious, "Radar micro-doppler for long range front-view gait recognition," in IEEE 3rd International Conference on Biometrics: Theory, Applications, and Systems (BTAS'09), 2009, pp. 1-6.

[2.23] A. Ghaleb, L. Vignaud, and J. Nicolas, "Micro-Doppler analysis of wheels and pedestrians in ISAR imaging," IET Signal Processing, vol. 2, no. 3, pp. 301-311, 2008.

[2.24] Y. S. Koo, et al., "UWB Micro-Doppler Radar for human Gait analysis, tracking more than one person, and vital sign detection of moving persons," in IEEE MTT-S International Microwave Symposium (IMS) Digest, 2013, pp. 1-4.

[2.25] V. C. Chen, et al., "Analysis of micro-Doppler signatures," IEEE Proceedings - Radar, Sonar and Navigation, vol. 150, no. 4, pp. 271-276, 2003.

[2.26] L. Stankovic, et al., "Micro-Doppler removal in the radar imaging analysis," IEEE Transactions on Aerospace and Electronic Systems, vol. 49, no. 2, pp. 1234-1250, 2013.

[2.27] A. Balleri, K. Chetty, and K. Woodbridge, "Classification of personnel targets by acoustic micro-Doppler signatures," IET Radar, Sonar & Navigation, vol. 5, no. 9, pp. 943-951, 2011.

[2.28] Y. Kim and H. Ling, "Human activity classification based on micro-Doppler signatures using a support vector machine," IEEE Transactions on Geoscience and Remote Sensing, vol. 47, no. 5, pp. 1328-1337, 2009.

[2.29] L. Stankovic, et al., "Inverse radon transform–based micro-doppler analysis from a reduced set of observations," in IEEE Transactions on Aerospace and Electronic Systems, vol. 51, no. 2, pp. 1155-1169, April 2015.

[2.30] J. Niu, et al., "Weighted average frequency algorithm for Hilbert–Huang spectrum and its application to micro-Doppler estimation," IET Radar, Sonar & Navigation, vol. 6, no. 7, pp. 595-602, 2012.

[2.31] B. Godana, A. Barroso and G. Leus, "Estimating Human Movement Parameters Using a Software Radio-based Radar," International Journal on Advances in Systems and Measurements, vol. 4, no. 1 & 2, pp. 20-31, 2011.

[2.32] T. Thayaparan, et al., "Analysis of radar micro-Doppler signatures from experimental helicopter and human data," IET Radar, Sonar & Navigation, vol. 1, no. 4, pp. 289-299, 2007.

[2.33] Y. Kim and H. Ling, "Through-wall human tracking with multiple Doppler sensors using an artificial neural network," IEEE Transactions on Antennas and Propagation, vol. 57, no. 7, pp. 2116-2122, 2009.

[2.34] J. Zhang, "Analysis of Human Gait Radar Signal Using Reassigned WVD," Physics Procedia, vol. 24, Part C, 2012, pp. 1607-1614.

[2.35] L. Du, et al., "Noise-robust classification of ground moving targets based on time-frequency feature from micro-Doppler signature," IEEE Sensors Journal, vol. 14, no. 8, pp. 2672-2682, 2014.

[2.36] D. P. Fairchild and R. M. Narayanan, "Classification of human motions using empirical mode decomposition of human micro-Doppler signatures," IET Radar, Sonar & Navigation, vol. 8, no. 5, pp. 425-434, 2014.

[2.37] T. K. Sarkar and O. Pereira, "Using the matrix pencil method to estimate the parameters of a sum of complex exponentials," in IEEE Antennas and Propagation Magazine, vol. 37, no. 1, pp. 48-55, Feb. 1995.

[2.38] R. Roy, T. Kailath, "ESPRIT – Estimation of Signal Parameters via Rotational Invariance Techniques," IEEE Transactions on Acoustics, Speech, and Signal Processing, Vol. ASSP–37, 1989, pp. 984–995.

[2.39] L. Du, et al., "Doppler spectrogram analysis of human gait via iterative adaptive approach," Electronics letters, vol. 45, no. 3, pp. 186-188, 2009.

[2.40] O. R. Fogle and B. D. Rigling, "Micro-range/micro-Doppler decomposition of human radar signatures," IEEE Transactions on Aerospace and Electronic Systems, vol. 48, no. 4, pp. 3058-3072, 2012.

[2.41] Y. Ding and J. Tang, "Micro-Doppler trajectory estimation of pedestrians using a continuous-wave radar," IEEE Transactions on Geoscience and Remote Sensing, vol. 52, no. 9, pp. 5807-5819, 2014.

[2.42] J. Tsao and B. D. Dteinberg, "Reduction of sidelobe and speckle artifacts in microwave imaging: The CLEAN technique," IEEE Trans. Antennas Propag., vol. 36, no. 4, pp. 543–556, Apr. 1988.

[2.43] S. Abdulatif, et al., "Real-time capable micro-Doppler signature decomposition of walking human limbs," in IEEE Radar Conference (RadarConf), pp. 1093–1098, 2017.

[2.44] R. G. Raj, V. C. Chen and R. Lipps, "Analysis of radar human gait signatures," in IET Signal Processing, vol. 4, no. 3, pp. 234-244, June 2010.

[2.45] I. Orovic, et al., "Multiwindow S-method for instantaneous frequency estimation and its application in radar signal analysis," IET Signal Processing, vol. 4, no. 4, pp. 363-370, 2010.

[2.46] P. Johnson, "New research Lab Leads to a Unique Radio Receiver," E-Systems Team, vol. 5, no. 4, pp. 6-7, 1985.

[2.47] J. Mitola, "The Software Radio," IEEE National Telesystems Conference, 1992.

[2.48] J. Ralston and C. Hargrave, "Software defined radar: An open source platform for prototype GPR development," in Proc. 14th Int. Ground Penetrating Radar Conf., Shanghai, China, Jun. 2012, pp. 172–177.

[2.49] J. Colorado, M. Perez, I. Mondragon, D. Mendez, C. Parra, C. Devia, J. Martinez-Moritz & L. Neira, "An integrated aerial system for landmine detection: SDR-based Ground Penetrating Radar onboard an autonomous drone", Advanced Robotics, 31:15, 791-808, 2017.

[2.50] https://www.ettus.com/product/details/UB210-KIT

[2.51] H. Zhang, L. Li, K. Wu, "24 GHz software-defined radar system for automotive applications", Proc. 10th Eur. Conf. Wireless Technol., pp. 138-141, Oct. 2007.

[2.52] S. Costanzo, et al. "High resolution software defined radar system for target detection," J. Electr. Comput. Eng., vol. 2013, pp. 1–7, Aug. 2013.

[2.53] http://www.ni.com/en-us/support/model.usrp-2920.html

[2.54] H. Zhang, L. Li, and K. Wu, "Software-defined six-port radar technique for precision range measurements," IEEE Sensors J., vol. 8, no. 10, pp. 1745–1751, Sep. 2008.

[2.55] J. Marimuthu, K.S. Bialkowski, A. Abbosh, "Software-Defined Radar for Medical Imaging," IEEE Trans. Microwave Theory and Techn., vol. 64, no. 2, pp. 643-652, Feb. 2016.

[2.56] http://www.limemicro.com/products/field-programmable-rf-ics-lms6002d/

[2.57] M. Frankford, "Exploration of MIMO radar techniques with a software defined radar," Ph.D. Dissertation, The Ohio State University, 2011.

[2.58] J. Park et al., "Software defined radar studies of human motion signatures," in Proc. IEEE Radar Conf., Atlanta, GA, USA, May 2012, pp. 596–601.

[2.59] B. Liu, R. Chen, "Software-defined radar and waveforms for studying micro-Doppler signatures", Proc. SPIE 9077, Radar Sensor Technology XVIII, 907718, May 2014.

[2.60] https://www.ettus.com/product/details/UN210-KIT

[2.61] A. R. Hunt, "Use of a Frequency-Hopping Radar for Imaging and Motion Detection Through Walls," in IEEE Transactions on Geoscience and Remote Sensing, vol. 47, no. 5, pp. 1402-1408, May 2009.

[3.1] https://www.mathworks.com/help/signal/ref/spectrogram.html

[3.2] Y. Wang, "UWB Pulse Radar for Human Imaging and Doppler Detection Applications," PhD Dissertation, University of Tennessee, May 2012.

[3.3] E. A. Elkhouly, "UWB Precise Indoor Localization System Performance, Limitations and its Integration," PhD Dissertation, University of Tennessee, Knoxville, Dec.2014.

[3.4] H. Wang et al., "An elegant solution: An alternative ultra-wideband transceiver based on stepped-frequency continuous-wave operation and compressive sensing," IEEE Microw. Mag., vol. 17, no. 7, pp. 53–63, Jul. 2016.

[3.5] S. Nahar, T. Phan, F. Quaiyum, L. Ren, A. E. Fathy, O. Kilic, "An Electromagnetic Model of Human Vital Signs Detection and Its Experimental Validation", IEEE Journal on Emerging and Selected Topics in Circuits and Systems, vol. 8, no. 2, pp. 338-349, Jun. 2018.

[3.6] M. Caruso, M. Bassi, A. Bevilacqua and A. Neviani, "A 2–16 GHz 65 nm CMOS Stepped-Frequency Radar Transmitter with Harmonic Rejection for High-Resolution Medical Imaging Applications," in IEEE Transactions on Circuits and Systems I: Regular Papers, vol. 62, no. 2, pp. 413-422, Feb. 2015.

[3.7] X. Chen, Y. Shen, Z. Wang, W. Rhee and Z. Wang, "A 17 mW 3-to-5 GHz Duty-Cycled Vital Sign Detection Radar Transceiver With Frequency Hopping and Time-Domain Oversampling," in IEEE Transactions on Circuits and Systems I: Regular Papers, vol. 64, no. 4, pp. 969-980, April 2017.

[3.8] C. Li, Y. Xiao and J. Lin, "A 5GHz Double-Sideband Radar Sensor Chip in 0.18 µm CMOS for Non-Contact Vital Sign Detection," in IEEE Microwave and Wireless Components Letters, vol. 18, no. 7, pp. 494-496, July 2008.

[3.9] C. Li, X. Yu, D. Li, L. Ran and J. Lin, "Software configurable 5.8 GHz radar sensor receiver chip in 0.13 µm CMOS for non-contact vital sign detection," 2009 IEEE Radio Frequency Integrated Circuits Symposium, Boston, MA, 2009, pp. 97-100.

[3.10] J. Yu et al., "An X-Band Radar Transceiver MMIC with Bandwidth Reduction in 0.13 µm SiGe Technology," in IEEE Journal of Solid-State Circuits, vol. 49, no. 9, pp. 1905-1915, Sept. 2014.

[3.11] Z. Peng et al., "A Portable FMCW Interferometry Radar With Programmable Low-IF Architecture for Localization, ISAR Imaging, and Vital Sign Tracking," in IEEE Transactions on Microwave Theory and Techniques, vol. 65, no. 4, pp. 1334-1344, April 2017.

[3.12] M. Mercuri et al., "Analysis of an Indoor Biomedical Radar-Based System for Health Monitoring," in IEEE Transactions on Microwave Theory and Techniques, vol. 61, no. 5, pp. 2061-2068, May 2013.

[4.1] RF Agile Transceiver AD9364 Datasheet from Analog Devices. Link:http://www.analog.com/media/en/technical-documentation/data-sheets/AD9364.pdf

[4.2] RF Agile Transceiver AD9364 Reference Manual from Analog Devices. Link: https://www.analog.com/media/cn/technical-documentation/user-guides/ad9364_reference_manual_ug-673.pdf

[4.3] https://www.mathworks.com/hardware-support/zynq-sdr.html

[4.4] https://github.com/analogdevicesinc/no-OS/tree/master/ad9361/sw

[4.5] https://github.com/analogdevicesinc/no-OS/tree/master/ad9361/scripts

[4.6] https://wiki.analog.com/resources/eval/user-guides/ad-fmcomms2-ebz/software/no-os-setup

[4.7] HMC833LP6GE PLL Datasheet from Analog Device. Link: https://www.analog.com/media/en/technical-documentation/data-sheets/hmc833.pdf

[4.8] ADF4152HV PLL Datasheet from Analog Device. Link: https://www.analog.com/media/en/technical-documentation/data-sheets/ADF4152HV.pdf

[4.9] DCYS100200-12 VCO Datasheet from Synergy Microwave Corporations. Link: https://synergymwave.com/products/vco/datasheet/DCYS100200-12.pdf

[4.10] DCYS200400-5 VCO Datasheet from Synergy Microwave Corporations. Link: https://synergymwave.com/products/vco/datasheet/DCYS200400-5.pdf

[4.11] D. Banerjee, "PLL Fundamentals, Part 2: PLL Behavior", Texas Instruments Literature Number: SNAP002.

[4.12] D. Banerjee, "PLL Fundamentals, Part 3: PLL Design", Texas Instruments Literature Number: SNAP003.

[4.13] https://form.analog.com/Form_Pages/RFComms/ADISimPll.aspx

[4.14] L. Liu and S. Liu, "Remote Detection of Human Vital Sign With Stepped-Frequency Continuous Wave Radar," in IEEE Journal of Selected Topics in Applied Earth Observations and Remote Sensing, vol. 7, no. 3, pp. 775-782, March 2014.

[5.1] F. Quaiyum, L. Ren, S. Nahar, F. Foroughian and A. E. Fathy, "Development of a reconfigurable low cost multi-mode radar system for contactless vital signs detection," 2017 IEEE MTT-S International Microwave Symposium (IMS), Honolulu, HI, 2017, pp. 1245-1247.

[5.2] T. Jaeschke, C. Bredendiek, and N. Pohl, "A 240 GHz ultra-wideband FMCW radar system with on-chip antennas for high resolution radar imaging," in IEEE MTT-S Int. Microw. Symp. Dig., Jun. 2013, pp. 1–4.

[5.3] N. Pohl et al., "Radar measurements with micrometer accuracy and nanometer stability using an ultra-wideband 80 GHz radar system," in Proc. IEEE Top. Conf. Wireless Sensors Sensor Netw. (WiSNet), Jan. 2013, pp. 31–33.

[5.4] Y. Lu, R. Krithivasan, W. M. L. Kuo and J. D. Cressler, "A 1.8-3.1 dB noise figure (3-10 GHz) SiGe HBT LNA for UWB applications," IEEE Radio Frequency Integrated Circuits (RFIC) Symposium, 2006, San Francisco, CA, 2006, pp. 4.

[5.5] A. Bevilacqua and A. M. Niknejad, "An ultrawideband CMOS low-noise amplifier for 3.1-10.6-GHz wireless receivers," IEEE Journal of Solid-State Circuits, vol. 39, no. 12, pp. 2259-2268, Dec. 2004.

[6.1] K. Naishadham and J.E. Piou, "A Novel 1-D Block Processing Approach to 2-D NMR Spectroscopy," Proceedings of the 2007 IEEE International Symposium on Biomedical Imaging: From Nano to Micro, Washington, D.C., April 2007.

[6.2] J. E. Piou, K. Naishadham and A. E. Fathy, "A 1-D Block Processing for Non-Invasive Detection of 2-D Cardiac and Respiratory Rates," 2018 IEEE Radar Conference (Radarconf'18), Oklahoma City, OK, 2018.

[6.3] J. E. Piou, "System realization using 2-D output measurements," Proceedings of the 2004 American Control Conference, 2840-2845, Boston, MA, USA, Jun. 2004.

[6.4] J. E. Piou, "A state identification method for 1-D measurements with spectral gaps," in Proc. AIAA Guidance Navigation and Control Conf., San Francisco, CA, USA, Aug. 2005, 2005-5943.

[6.5] R. Boulic, N. M. Thalmann, "A global human walking model with real-time kinematic personification," The visual computer, pp. 344-358, 1990.

[6.6] C Gabriel, S Gabriel and E Corhout, "The dielectric properties of biological tissues: I. Literature survey," in Phys. Med. Biol, vol 41, pp.2231 – 2249, UK, 1996.

[6.7] J. M. Garcia-Rubia, O. Kilic, V. Dang, Q. Nguyen and N. Tran, "Analysis of moving human micro-Doppler signature in forest environments," Progress In Electromagnetics Research, vol. 148, 1-14, 2014.

[6.8] O. Kilic , J.M. Garcia-Rubia, N. Tran, V. Dang, and Q. Nguyen, "Detection of moving human micro-Doppler signature in forest environments with swaying tree components by wind," Radio Science, pp. 238-248, 2015.

[6.9] https://altairhyperworks.com/product/FEKO

[6.10] S. M. Rao, D. R. Wilton, and A. W. Glisson, "Electromagnetic scattering by surfaces of arbitrary shape," IEEE Trans. Antennas Propagat., vol. 30, no. 3, pp. 409-418, 1982.

[6.11] J. Song, C. Lu, W. C. Chew, "Multilevel fast multipole algorithm for electromagnetic scattering by large complex objects," IEEE Trans. Antennas. Propag., vol. 45, no. 10, pp. 1488-1493, 1997.

[6.12] O. Ergul and L. Gurel, "The multilevel fast multipole algorithm (MLFMA) for solving large-scale computational electromagnetics problems," John Wiley & Sons, 2014.

[6.13] N. Tran, T. Phan, O. Kilic, "CUDA-MPI Implementation of Fast Multipole Method On GPU Clusters For Solving Dielectric Objects," ACES Express, vol. 1, no. 6, pp. 185-189, 2016.

[7.1]   R. M. Narayanan and M. Zenaldin, "Radar micro-Doppler signatures of various human activities," in IET Radar, Sonar & Navigation, vol. 9, no. 9, pp. 1205-1215, December 2015.

[7.2]   C. Li, Y. Xiao, and J. Lin, "Experiment and Spectral Analysis of a Low-power Ka-band Heartbeat Detector Measuring from Four Sides of a Human Body," IEEE Trans. Microw. Theory Tech., vol. 54, no. 12, pp. 4464-4471, Dec. 2006.

[7.3] L. Ren, H. Wang, K. Naishadham, Q. Liu, A. E. Fathy, "Non-Invasive Detection of Cardiac and Respiratory Rates from Stepped Frequency Continuous Wave Radar Measurements Using the State Space Method," IEEE MTT-S Int. Microwave Symp. Dig., May 2015.

[7.4]   K. M. Chen, et al., "Microwave Life-detection Systems for Searching Human Subjects under Earthquake Rubble or Behind Barrier," IEEE Trans. Biomed. Eng., vol. 27, pp. 105-114, Jan. 2000.

[7.5] C. Li, J. Lin, "Optimal carrier frequency of non-contact vital sign detectors", Proc. IEEE Radio and Wireless Symp., pp. 281-284, Jan. 2007.

APPENDIX

Appendix 1.A: No-OS main.c file for SDR

```c
/*************************** Include Files ****************************/
#define XILINX_PLATFORM
#include "xil_io.h"
#include <stdio.h>
#include "config.h"
#include "ad9361_api.h"
#include "parameters.h"
#include "platform.h"
#ifdef XILINX_PLATFORM
#include <xil_cache.h>
#endif
#if defined XILINX_PLATFORM || defined LINUX_PLATFORM
#include "adc_core.h"
#include "dac_core.h"
#endif

/****Variables Definitions ****************************/

AD9361_InitParam default_init_param = {
    /* Device selection */
    ID_AD9361,    // dev_sel
    /* Identification number */
    0,            //id_no
    /* Reference Clock */
    40000000UL,   //reference_clk_rate
    /* Base Configuration */
    0,            //two_rx_two_tx_mode_enable *** adi,2rx-2tx-mode-enable
    1,            //one_rx_one_tx_mode_use_rx_num *** adi,1rx-1tx-mode-use-rx-num
    1,            //one_rx_one_tx_mode_use_tx_num *** adi,1rx-1tx-mode-use-tx-num
    1,            //frequency_division_duplex_mode_enable *** adi,frequency-division-duplex-mode-enable
    0,            //frequency_division_duplex_independent_mode_enable *** adi,frequency-division-duplex-independent-mode-enable
    0,            //tdd_use_dual_synth_mode_enable *** adi,tdd-use-dual-synth-mode-enable
    0,            //tdd_skip_vco_cal_enable *** adi,tdd-skip-vco-cal-enable
    0,            //tx_fastlock_delay_ns *** adi,tx-fastlock-delay-ns
    0,            //rx_fastlock_delay_ns *** adi,rx-fastlock-delay-ns
    0,            //rx_fastlock_pincontrol_enable *** adi,rx-fastlock-pincontrol-enable
    0,            //tx_fastlock_pincontrol_enable *** adi,tx-fastlock-pincontrol-enable
    0,            //external_rx_lo_enable *** adi,external-rx-lo-enable
    0,            //external_tx_lo_enable *** adi,external-tx-lo-enable
    5,            //dc_offset_tracking_update_event_mask *** adi,dc-offset-tracking-update-event-mask
    6,            //dc_offset_attenuation_high_range *** adi,dc-offset-attenuation-high-range
    5,            //dc_offset_attenuation_low_range *** adi,dc-offset-attenuation-low-range
    0x28, //dc_offset_count_high_range *** adi,dc-offset-count-high-range
    0x32, //dc_offset_count_low_range *** adi,dc-offset-count-low-range
    0,            //split_gain_table_mode_enable *** adi,split-gain-table-mode-enable
    MAX_SYNTH_FREF,    //trx_synthesizer_target_fref_overwrite_hz *** adi,trx-synthesizer-target-fref-overwrite-hz
    1,            // qec_tracking_slow_mode_enable *** adi,qec-tracking-slow-mode-enable
    /* ENSM Control */
    0,            //ensm_enable_pin_pulse_mode_enable *** adi,ensm-enable-pin-pulse-mode-enable
    0,            //ensm_enable_txnrx_control_enable *** adi,ensm-enable-txnrx-control-enable
```

```
        /* LO Control */
        2000000000UL,//rx_synthesizer_frequency_hz *** adi,rx-synthesizer-frequency-hz
        2000000000UL,//tx_synthesizer_frequency_hz *** adi,tx-synthesizer-frequency-hz
        /* Rate & BW Control */
        {983040000, 245760000, 122880000, 61440000, 30720000, 30720000},
//uint32_t    rx_path_clock_frequencies[6] *** adi,rx-path-clock-frequencies
        {983040000, 122880000, 122880000, 61440000, 30720000, 30720000},
//uint32_t    tx_path_clock_frequencies[6] *** adi,tx-path-clock-frequencies
        18000000, //rf_rx_bandwidth_hz *** adi,rf-rx-bandwidth-hz
        18000000, //rf_tx_bandwidth_hz *** adi,rf-tx-bandwidth-hz
        /* RF Port Control */
        0,              //rx_rf_port_input_select *** adi,rx-rf-port-input-select
        0,              //tx_rf_port_input_select *** adi,tx-rf-port-input-select
        /* TX Attenuation Control */
        10000, //tx_attenuation_mdB *** adi,tx-attenuation-mdB
        0,              //update_tx_gain_in_alert_enable *** adi,update-tx-gain-in-alert-enable
        /* Reference Clock Control */
        0,                 //xo_disable_use_ext_refclk_enable *** adi,xo-disable-use-ext-refclk-enable
        {8, 5920},    //dcxo_coarse_and_fine_tune[2] *** adi,dcxo-coarse-and-fine-tune
        CLKOUT_DISABLE,     //clk_output_mode_select *** adi,clk-output-mode-select
        /* Gain Control */
        0,              //gc_rx1_mode *** adi,gc-rx1-mode
        0,              //gc_rx2_mode *** adi,gc-rx2-mode
        58,             //gc_adc_large_overload_thresh *** adi,gc-adc-large-overload-thresh
        4,              //gc_adc_ovr_sample_size *** adi,gc-adc-ovr-sample-size
        47,             //gc_adc_small_overload_thresh *** adi,gc-adc-small-overload-thresh
        8192,  //gc_dec_pow_measurement_duration *** adi,gc-dec-pow-measurement-duration
        0,              //gc_dig_gain_enable *** adi,gc-dig-gain-enable
        800,    //gc_lmt_overload_high_thresh *** adi,gc-lmt-overload-high-thresh
        704,    //gc_lmt_overload_low_thresh *** adi,gc-lmt-overload-low-thresh
        24,             //gc_low_power_thresh *** adi,gc-low-power-thresh
        15,             //gc_max_dig_gain *** adi,gc-max-dig-gain
        /* Gain MGC Control */
        1,              //mgc_dec_gain_step *** adi,mgc-dec-gain-step
        1,              //mgc_inc_gain_step *** adi,mgc-inc-gain-step
        0,              //mgc_rx1_ctrl_inp_enable *** adi,mgc-rx1-ctrl-inp-enable
        0,              //mgc_rx2_ctrl_inp_enable *** adi,mgc-rx2-ctrl-inp-enable
        0,              //mgc_split_table_ctrl_inp_gain_mode *** adi,mgc-split-table-ctrl-inp-gain-mode
        /* Gain AGC Control */
        10,             //agc_adc_large_overload_exceed_counter *** adi,agc-adc-large-overload-exceed-counter
        2,              //agc_adc_large_overload_inc_steps *** adi,agc-adc-large-overload-inc-steps
        0,              //agc_adc_lmt_small_overload_prevent_gain_inc_enable *** adi,agc-adc-lmt-small-overload-prevent-gain-inc-enable
        10,             //agc_adc_small_overload_exceed_counter *** adi,agc-adc-small-overload-exceed-counter
        4,              //agc_dig_gain_step_size *** adi,agc-dig-gain-step-size
        3,              //agc_dig_saturation_exceed_counter *** adi,agc-dig-saturation-exceed-counter
        1000,  // agc_gain_update_interval_us *** adi,agc-gain-update-interval-us
        0,                 //agc_immed_gain_change_if_large_adc_overload_enable *** adi,agc-immed-gain-change-if-large-adc-overload-enable
        0,                 //agc_immed_gain_change_if_large_lmt_overload_enable *** adi,agc-immed-gain-change-if-large-lmt-overload-enable
        10,             //agc_inner_thresh_high *** adi,agc-inner-thresh-high
        1,              //agc_inner_thresh_high_dec_steps *** adi,agc-inner-thresh-high-dec-steps
        12,             //agc_inner_thresh_low *** adi,agc-inner-thresh-low
        1,              //agc_inner_thresh_low_inc_steps *** adi,agc-inner-thresh-low-inc-steps
```

```
10,              //agc_lmt_overload_large_exceed_counter *** adi,agc-lmt-overload-large-exceed-counter
2,               //agc_lmt_overload_large_inc_steps *** adi,agc-lmt-overload-large-inc-steps
10,              //agc_lmt_overload_small_exceed_counter *** adi,agc-lmt-overload-small-exceed-counter
5,          //agc_outer_thresh_high *** adi,agc-outer-thresh-high
2,               //agc_outer_thresh_high_dec_steps *** adi,agc-outer-thresh-high-dec-steps
18,         //agc_outer_thresh_low *** adi,agc-outer-thresh-low
2,               //agc_outer_thresh_low_inc_steps *** adi,agc-outer-thresh-low-inc-steps
1,               //agc_attack_delay_extra_margin_us; *** adi,agc-attack-delay-extra-margin-us
0,               //agc_sync_for_gain_counter_enable *** adi,agc-sync-for-gain-counter-enable
/* Fast AGC */
64,              //fagc_dec_pow_measuremnt_duration *** adi,fagc-dec-pow-measurement-duration
260,   //fagc_state_wait_time_ns ***  adi,fagc-state-wait-time-ns
/* Fast AGC - Low Power */
0,               //fagc_allow_agc_gain_increase *** adi,fagc-allow-agc-gain-increase-enable
5,               //fagc_lp_thresh_increment_time *** adi,fagc-lp-thresh-increment-time
1,               //fagc_lp_thresh_increment_steps *** adi,fagc-lp-thresh-increment-steps
/* Fast AGC - Lock Level */
10,          //fagc_lock_level ***  adi,fagc-lock-level
1,               //fagc_lock_level_lmt_gain_increase_en *** adi,fagc-lock-level-lmt-gain-increase-enable
5,               //fagc_lock_level_gain_increase_upper_limit *** adi,fagc-lock-level-gain-increase-upper-limit
/* Fast AGC - Peak Detectors and Final Settling */
1,               //fagc_lpf_final_settling_steps *** adi,fagc-lpf-final-settling-steps
1,               //fagc_lmt_final_settling_steps *** adi,fagc-lmt-final-settling-steps
3,               //fagc_final_overrange_count *** adi,fagc-final-overrange-count
/* Fast AGC - Final Power Test */
0,               //fagc_gain_increase_after_gain_lock_en *** adi,fagc-gain-increase-after-gain-lock-enable
/* Fast AGC - Unlocking the Gain */
0,               //fagc_gain_index_type_after_exit_rx_mode *** adi,fagc-gain-index-type-after-exit-rx-mode
1,               //fagc_use_last_lock_level_for_set_gain_en *** adi,fagc-use-last-lock-level-for-set-gain-enable
1,               //fagc_rst_gla_stronger_sig_thresh_exceeded_en *** adi,fagc-rst-gla-stronger-sig-thresh-exceeded-enable
5,          //fagc_optimized_gain_offset ***  adi,fagc-optimized-gain-offset
10,              //fagc_rst_gla_stronger_sig_thresh_above_ll *** adi,fagc-rst-gla-stronger-sig-thresh-above-ll
1,               //fagc_rst_gla_engergy_lost_sig_thresh_exceeded_en *** adi,fagc-rst-gla-engergy-lost-sig-thresh-exceeded-enable
1,               //fagc_rst_gla_engergy_lost_goto_optim_gain_en *** adi,fagc-rst-gla-engergy-lost-goto-optim-gain-enable
10,              //fagc_rst_gla_engergy_lost_sig_thresh_below_ll *** adi,fagc-rst-gla-engergy-lost-sig-thresh-below-ll
8,               //fagc_energy_lost_stronger_sig_gain_lock_exit_cnt *** adi,fagc-energy-lost-stronger-sig-gain-lock-exit-cnt
1,               //fagc_rst_gla_large_adc_overload_en *** adi,fagc-rst-gla-large-adc-overload-enable
1,               //fagc_rst_gla_large_lmt_overload_en *** adi,fagc-rst-gla-large-lmt-overload-enable
0,               //fagc_rst_gla_en_agc_pulled_high_en *** adi,fagc-rst-gla-en-agc-pulled-high-enable
0,               //fagc_rst_gla_if_en_agc_pulled_high_mode *** adi,fagc-rst-gla-if-en-agc-pulled-high-mode
64,              //fagc_power_measurement_duration_in_state5 *** adi,fagc-power-measurement-duration-in-state5
/* RSSI Control */
1,          //rssi_delay *** adi,rssi-delay
1000,  //rssi_duration *** adi,rssi-duration
3,          //rssi_restart_mode *** adi,rssi-restart-mode
0,          //rssi_unit_is_rx_samples_enable *** adi,rssi-unit-is-rx-samples-enable
1,          //rssi_wait *** adi,rssi-wait
/* Aux ADC Control */
256,   //aux_adc_decimation *** adi,aux-adc-decimation
40000000UL,  //aux_adc_rate *** adi,aux-adc-rate
/* AuxDAC Control */
1,          //aux_dac_manual_mode_enable ***  adi,aux-dac-manual-mode-enable
```

```
0,              //aux_dac1_default_value_mV *** adi,aux-dac1-default-value-mV
0,              //aux_dac1_active_in_rx_enable *** adi,aux-dac1-active-in-rx-enable
0,              //aux_dac1_active_in_tx_enable *** adi,aux-dac1-active-in-tx-enable
0,              //aux_dac1_active_in_alert_enable *** adi,aux-dac1-active-in-alert-enable
0,              //aux_dac1_rx_delay_us *** adi,aux-dac1-rx-delay-us
0,              //aux_dac1_tx_delay_us *** adi,aux-dac1-tx-delay-us
0,              //aux_dac2_default_value_mV *** adi,aux-dac2-default-value-mV
0,              //aux_dac2_active_in_rx_enable *** adi,aux-dac2-active-in-rx-enable
0,              //aux_dac2_active_in_tx_enable *** adi,aux-dac2-active-in-tx-enable
0,              //aux_dac2_active_in_alert_enable *** adi,aux-dac2-active-in-alert-enable
0,              //aux_dac2_rx_delay_us *** adi,aux-dac2-rx-delay-us
0,              //aux_dac2_tx_delay_us *** adi,aux-dac2-tx-delay-us
/* Temperature Sensor Control */
256,   //temp_sense_decimation *** adi,temp-sense-decimation
1000,  //temp_sense_measurement_interval_ms *** adi,temp-sense-measurement-interval-ms
0xCE,  //temp_sense_offset_signed *** adi,temp-sense-offset-signed
1,              //temp_sense_periodic_measurement_enable *** adi,temp-sense-periodic-measurement-enable
/* Control Out Setup */
0xE0,  //ctrl_outs_enable_mask *** adi,ctrl-outs-enable-mask
0x01,          //ctrl_outs_index *** adi,ctrl-outs-index
/* External LNA Control */
0,              //elna_settling_delay_ns *** adi,elna-settling-delay-ns
0,              //elna_gain_mdB *** adi,elna-gain-mdB
0,              //elna_bypass_loss_mdB *** adi,elna-bypass-loss-mdB
0,              //elna_rx1_gpo0_control_enable *** adi,elna-rx1-gpo0-control-enable
0,              //elna_rx2_gpo1_control_enable *** adi,elna-rx2-gpo1-control-enable
0,              //elna_gaintable_all_index_enable *** adi,elna-gaintable-all-index-enable
/* Digital Interface Control */
0,              //digital_interface_tune_skip_mode *** adi,digital-interface-tune-skip-mode
0,              //digital_interface_tune_fir_disable *** adi,digital-interface-tune-fir-disable
1,              //pp_tx_swap_enable *** adi,pp-tx-swap-enable
1,              //pp_rx_swap_enable *** adi,pp-rx-swap-enable
0,              //tx_channel_swap_enable *** adi,tx-channel-swap-enable
0,              //rx_channel_swap_enable *** adi,rx-channel-swap-enable
1,              //rx_frame_pulse_mode_enable *** adi,rx-frame-pulse-mode-enable
0,              //two_t_two_r_timing_enable *** adi,2t2r-timing-enable
0,              //invert_data_bus_enable *** adi,invert-data-bus-enable
0,              //invert_data_clk_enable *** adi,invert-data-clk-enable
0,              //fdd_alt_word_order_enable *** adi,fdd-alt-word-order-enable
0,              //invert_rx_frame_enable *** adi,invert-rx-frame-enable
0,              //fdd_rx_rate_2tx_enable *** adi,fdd-rx-rate-2tx-enable
0,              //swap_ports_enable *** adi,swap-ports-enable
0,              //single_data_rate_enable *** adi,single-data-rate-enable
1,              //lvds_mode_enable *** adi,lvds-mode-enable
0,              //half_duplex_mode_enable *** adi,half-duplex-mode-enable
0,              //single_port_mode_enable *** adi,single-port-mode-enable
0,              //full_port_enable *** adi,full-port-enable
0,              //full_duplex_swap_bits_enable *** adi,full-duplex-swap-bits-enable
0,              //delay_rx_data *** adi,delay-rx-data
0,              //rx_data_clock_delay *** adi,rx-data-clock-delay
4,              //rx_data_delay *** adi,rx-data-delay
7,              //tx_fb_clock_delay *** adi,tx-fb-clock-delay
```

```
0,              //tx_data_delay *** adi,tx-data-delay
150,    //lvds_bias_mV *** adi,lvds-bias-mV
1,              //lvds_rx_onchip_termination_enable *** adi,lvds-rx-onchip-termination-enable
0,              //rx1rx2_phase_inversion_en *** adi,rx1-rx2-phase-inversion-enable
0xFF,   //lvds_invert1_control *** adi,lvds-invert1-control
0x0F,   //lvds_invert2_control *** adi,lvds-invert2-control
/* GPO Control */
0,              //gpo0_inactive_state_high_enable *** adi,gpo0-inactive-state-high-enable
0,              //gpo1_inactive_state_high_enable *** adi,gpo1-inactive-state-high-enable
0,              //gpo2_inactive_state_high_enable *** adi,gpo2-inactive-state-high-enable
0,              //gpo3_inactive_state_high_enable *** adi,gpo3-inactive-state-high-enable
0,              //gpo0_slave_rx_enable *** adi,gpo0-slave-rx-enable
0,              //gpo0_slave_tx_enable *** adi,gpo0-slave-tx-enable
0,              //gpo1_slave_rx_enable *** adi,gpo1-slave-rx-enable
0,              //gpo1_slave_tx_enable *** adi,gpo1-slave-tx-enable
0,              //gpo2_slave_rx_enable *** adi,gpo2-slave-rx-enable
0,              //gpo2_slave_tx_enable *** adi,gpo2-slave-tx-enable
0,              //gpo3_slave_rx_enable *** adi,gpo3-slave-rx-enable
0,              //gpo3_slave_tx_enable *** adi,gpo3-slave-tx-enable
0,              //gpo0_rx_delay_us *** adi,gpo0-rx-delay-us
0,              //gpo0_tx_delay_us *** adi,gpo0-tx-delay-us
0,              //gpo1_rx_delay_us *** adi,gpo1-rx-delay-us
0,              //gpo1_tx_delay_us *** adi,gpo1-tx-delay-us
0,              //gpo2_rx_delay_us *** adi,gpo2-rx-delay-us
0,              //gpo2_tx_delay_us *** adi,gpo2-tx-delay-us
0,              //gpo3_rx_delay_us *** adi,gpo3-rx-delay-us
0,              //gpo3_tx_delay_us *** adi,gpo3-tx-delay-us
/* Tx Monitor Control */
37000, //low_high_gain_threshold_mdB *** adi,txmon-low-high-thresh
0,              //low_gain_dB *** adi,txmon-low-gain
24,             //high_gain_dB *** adi,txmon-high-gain
0,              //tx_mon_track_en *** adi,txmon-dc-tracking-enable
0,              //one_shot_mode_en *** adi,txmon-one-shot-mode-enable
511,    //tx_mon_delay *** adi,txmon-delay
8192,   //tx_mon_duration *** adi,txmon-duration
2,              //tx1_mon_front_end_gain *** adi,txmon-1-front-end-gain
2,              //tx2_mon_front_end_gain *** adi,txmon-2-front-end-gain
48,             //tx1_mon_lo_cm *** adi,txmon-1-lo-cm
48,             //tx2_mon_lo_cm *** adi,txmon-2-lo-cm
/* GPIO definitions */
-1,             //gpio_resetb *** reset-gpios
/* MCS Sync */
-1,             //gpio_sync *** sync-gpios
-1,             //gpio_cal_sw1 *** cal-sw1-gpios
-1,             //gpio_cal_sw2 *** cal-sw2-gpios
/* External LO clocks */
NULL,   //(*ad9361_rfpll_ext_recalc_rate)()
NULL,   //(*ad9361_rfpll_ext_round_rate)()
NULL    //(*ad9361_rfpll_ext_set_rate)()
};
```

```c
AD9361_RXFIRConfig rx_fir_config = {    // BPF PASSBAND 3/20 fs to 1/4 fs
        3, // rx
        0, // rx_gain
        1, // rx_dec
        {-4, -6, -37, 35, 186, 86, -284, -315,
         107, 219, -4, 271, 558, -307, -1182, -356,
         658, 157, 207, 1648, 790, -2525, -2553, 748,
         865, -476, 3737, 6560, -3583, -14731, -5278, 14819,
         14819, -5278, -14731, -3583, 6560, 3737, -476, 865,
         748, -2553, -2525, 790, 1648, 207, 157, 658,
         -356, -1182, -307, 558, 271, -4, 219, 107,
         -315, -284, 86, 186, 35, -37, -6, -4,
         0, 0, 0, 0, 0, 0, 0, 0,
         0, 0, 0, 0, 0, 0, 0, 0,
         0, 0, 0, 0, 0, 0, 0, 0,
         0, 0, 0, 0, 0, 0, 0, 0,
         0, 0, 0, 0, 0, 0, 0, 0,
         0, 0, 0, 0, 0, 0, 0, 0,
         0, 0, 0, 0, 0, 0, 0, 0,
         0, 0, 0, 0, 0, 0, 0, 0}, // rx_coef[128]
        64, // rx_coef_size
        {0, 0, 0, 0, 0, 0}, //rx_path_clks[6]
        0 // rx_bandwidth
};

AD9361_TXFIRConfig tx_fir_config = {    // BPF PASSBAND 3/20 fs to 1/4 fs
        3, // tx
        -6, // tx_gain
        1, // tx_int
        {-4, -6, -37, 35, 186, 86, -284, -315,
         107, 219, -4, 271, 558, -307, -1182, -356,
         658, 157, 207, 1648, 790, -2525, -2553, 748,
         865, -476, 3737, 6560, -3583, -14731, -5278, 14819,
         14819, -5278, -14731, -3583, 6560, 3737, -476, 865,
         748, -2553, -2525, 790, 1648, 207, 157, 658,
         -356, -1182, -307, 558, 271, -4, 219, 107,
         -315, -284, 86, 186, 35, -37, -6, -4,
         0, 0, 0, 0, 0, 0, 0, 0,
         0, 0, 0, 0, 0, 0, 0, 0,
         0, 0, 0, 0, 0, 0, 0, 0,
         0, 0, 0, 0, 0, 0, 0, 0,
         0, 0, 0, 0, 0, 0, 0, 0,
         0, 0, 0, 0, 0, 0, 0, 0,
         0, 0, 0, 0, 0, 0, 0, 0,
         0, 0, 0, 0, 0, 0, 0, 0}, // tx_coef[128]
        64, // tx_coef_size
        {0, 0, 0, 0, 0, 0}, // tx_path_clks[6]
        0 // tx_bandwidth
};

struct ad9361_rf_phy *ad9361_phy;
```

```c
/***********@brief main*********************************************/
int main(void)
{
// Default Settings Begin
#ifdef XILINX_PLATFORM
       Xil_ICacheEnable();
       Xil_DCacheEnable();
#endif


       // NOTE: The user has to choose the GPIO numbers according to desired
       // carrier board.
       default_init_param.gpio_resetb = GPIO_RESET_PIN;
#ifdef FMCOMMS5
       default_init_param.gpio_sync = GPIO_SYNC_PIN;
       default_init_param.gpio_cal_sw1 = GPIO_CAL_SW1_PIN;
       default_init_param.gpio_cal_sw2 = GPIO_CAL_SW2_PIN;
       default_init_param.rx1rx2_phase_inversion_en = 1;
#else
       default_init_param.gpio_sync = -1;
       default_init_param.gpio_cal_sw1 = -1;
       default_init_param.gpio_cal_sw2 = -1;
#endif

#ifdef LINUX_PLATFORM
       gpio_init(default_init_param.gpio_resetb);
#else
       gpio_init(GPIO_DEVICE_ID);
#endif
       gpio_direction(default_init_param.gpio_resetb, 1);

       spi_init(SPI_DEVICE_ID, 1, 0);

       if (AD9364_DEVICE)
             default_init_param.dev_sel = ID_AD9364;
       if (AD9363A_DEVICE)
             default_init_param.dev_sel = ID_AD9363A;

       ad9361_init(&ad9361_phy, &default_init_param);

       ad9361_set_tx_fir_config(ad9361_phy, tx_fir_config);
       ad9361_set_rx_fir_config(ad9361_phy, rx_fir_config);

#ifndef AXI_ADC_NOT_PRESENT
#if defined XILINX_PLATFORM || defined LINUX_PLATFORM
#ifdef DAC_DMA
#ifdef FMCOMMS5
       dac_init(ad9361_phy_b, DATA_SEL_DMA, 0);
#endif
       dac_init(ad9361_phy, DATA_SEL_DMA, 1);
#else
#ifdef FMCOMMS5
```

```c
        dac_init(ad9361_phy_b, DATA_SEL_DDS, 0);
#endif
        dac_init(ad9361_phy, DATA_SEL_DDS, 1);
#endif
#endif
#endif

        printf("Done.\n");

#ifdef XILINX_PLATFORM
        Xil_DCacheDisable();
        Xil_ICacheDisable();
#endif
// Default Settings End

// SFCW Settings Begin
// Gain control mode is Manual        (gc_rx1_mode = 0), so need to specify RX RF Gain
        ad9361_set_rx_rf_gain (ad9361_phy, 0, 20);

        int32_t pulse_count;
        int32_t freq_count;
        uint64_t LO_FREQ;

        uint8_t freq_reg_tx[FREQ_NUMBER][16], freq_reg_rx[FREQ_NUMBER][16];

        uint32_t data[2*PULSE_NUMBER][FREQ_NUMBER];

        printf("%u\n", PULSE_NUMBER); //PULSE or FRAME NUMBER saved in ad9361.h
        printf("%u\n", FREQ_NUMBER); //FREQUENCY NUMBER saved in ad9361.h

        printf("%u\n", SAMPLE_NUMBER); //SAMPLE NUMBER saved in ad9361.h

        LO_FREQ= START_FREQ; //LO START FREQURNCY, value saved in ad9361.h

        // This loop saves the fastlock register values for the different frequencies
        for (freq_count= 0; freq_count< FREQ_NUMBER; freq_count++)
        {
                mdelay(40);
                ad9361_set_tx_lo_freq (ad9361_phy, LO_FREQ);
                mdelay(40);
                ad9361_set_rx_lo_freq (ad9361_phy, LO_FREQ);
                mdelay(40);

                ad9361_tx_fastlock_store(ad9361_phy, 0);
                ad9361_rx_fastlock_store(ad9361_phy, 2);

                ad9361_tx_fastlock_save(ad9361_phy, 0, &freq_reg_tx[freq_count]);
                ad9361_rx_fastlock_save(ad9361_phy, 2, &freq_reg_rx[freq_count]);

                LO_FREQ+= STEP_FREQ; // Increment by STEP_FREQUENCY saved in ad9361.h
        }
        mdelay(40);
```

178

```c
        gpio_direction(GPIO_ENABLE_PIN, 1);
        gpio_set_value(GPIO_ENABLE_PIN, 0);


        printf("Start\n");

        // This loop actually does the sweep and saves adc samples for each sweep in the data matrix
        for(pulse_count= 0; pulse_count< PULSE_NUMBER; pulse_count++)
        {
                for (freq_count= 0; freq_count< FREQ_NUMBER; freq_count++)
                {
                ad9361_tx_fastlock_load(ad9361_phy, 1, freq_reg_tx[freq_count]);
                //mdelay(1);
                ad9361_rx_fastlock_load(ad9361_phy, 3, freq_reg_rx[freq_count]);
                //mdelay(1);

                ad9361_tx_fastlock_recall(ad9361_phy, 1);
                //mdelay(1);
                ad9361_rx_fastlock_recall(ad9361_phy, 3);

                //mdelay(1);

                adc_capture(10, ADC_DDR_BASEADDR);
                Xil_DCacheInvalidateRange(ADC_DDR_BASEADDR,10);
                data[pulse_count][freq_count] = Xil_In32(ADC_DDR_BASEADDR+36);

                gpio_set_value(GPIO_ENABLE_PIN, 1);
                udelay(10);

                adc_capture(10, ADC_DDR_BASEADDR);
                Xil_DCacheInvalidateRange(ADC_DDR_BASEADDR,10);
                data[pulse_count+PULSE_NUMBER][freq_count] = Xil_In32(ADC_DDR_BASEADDR+36);

                gpio_set_value(GPIO_ENABLE_PIN, 0);
                udelay(10);
                }
        }
        printf("End\n");

        // This loop sends the data through UART to MATLAB for processing/plotting
        for(pulse_count= 0; pulse_count< 2*PULSE_NUMBER; pulse_count++)
        {
        for (freq_count= 0; freq_count< FREQ_NUMBER*SAMPLE_NUMBER; freq_count++)
                {
                        printf("%4x\n", data[pulse_count][freq_count]);
                }
        }

        mdelay(40000);
        return 0;
}
```

Appendix 1.B: MATLAB Script to Read and Parse Data from SDR:

```matlab
clc;
close all;
clearvars;

% Need to change this according to what the computer identifies the port as
s = serial ('COM9');

s.BaudRate = 115200;
fopen(s);
init = fscanf(s)
data = zeros(0,1);


init_done = fscanf(s)

pulse_num = str2double(fscanf(s)); % Get pulse number from No-OS
freq_num = str2double(fscanf(s)); % Get frequency number from No-OS
sample = str2double(fscanf(s)); % Get sample number from No-OS

N = 2*pulse_num*freq_num*sample; %Total number of samples

start_sweep = fscanf(s) % Sweep starts
tic
end_sweep = fscanf(s) % Sweep ends
Time = toc; % For calculating total sweep time

% Read data through serial port
for i = 1:N
    temp = fscanf(s, '%x\n');
    data = [data;temp];
end

fclose(s);
delete(s);

%% Separating 32 bit numbers consisting of the I & Q samples (16 bit each)
MASK = hex2dec('ffff')

datai = zeros(N,1);
dataq = zeros(N,1); % Q samples 16 MSB
for i = 1:length(data)
    datai(i) = uint16(bitand(MASK, data(i,1))); % I samples: 16 LSB
    if datai(i) > 32768
        datai(i) = datai(i) - 65536; % signed-unsigned conversion
    end
    % Q samples: 16 MSB
    dataq(i) = uint16(bitand(MASK, bitsrl(uint32(data(i,1)),16)));
    if dataq(i) > 32768
        dataq(i) = dataq(i) - 65536; % signed-unsigned conversion
    end
end
```

180

```matlab
%% Data Saving, Calibrating and Plotting

data = dataq+1i*datai;
figure(1);plot(abs(data(1:end)))

% Saving data by frame
data_c = reshape(data, [freq_num*sample, 2*pulse_num]);
data_q = reshape(dataq, [freq_num*sample, 2*pulse_num]);
data_i = reshape(datai, [freq_num*sample, 2*pulse_num]);


data_avg = data_c;


figure;mesh(abs(data_avg));


data_cal = data_avg(:,1:pulse_num); % Calibration Data
data_meas = data_avg(:,pulse_num+1:2*pulse_num); % Actual Measurement Data

% Compensating for phase incoherence
post_cal = data_meas .*exp(-1j*angle(data_cal));


hrrp_post_cal = ifftshift(ifft(post_cal,64,1),1);


post_cal_nodc = post_cal - repmat(mean(post_cal),size(post_cal,1),1);
hrrp_post_cal_nodc = ifftshift(ifft(post_cal_nodc,64,1),1);


figure
mesh(abs(hrrp_post_cal))
title(' Postcal w/ DC HRRP')


figure
mesh(abs(hrrp_post_cal_nodc))
title(' Postcal wo/DC HRRP')
```

VITA

Farhan Quaiyum was born in Dhaka, Bangladesh, in 1989. He received his B.Sc. degree in Electrical and Electronic Engineering from Bangladesh University of Engineering and Technology in 2012. He joined the University of Tennessee, Knoxville in August 2013 and received the M.S. degree in Electrical Engineering in 2017. He is studying toward his Ph.D. degree in Electrical Engineering at the University of Tennessee, Knoxville, with expected completion date in December 2018. He was a Design Engineering Intern with Qorvo in Chelmsford, MA from May 2017 to August 2017, where he was engaged in the design of highly linear and high isolation RF switches. He has authored or coauthored numerous journal/conference papers and has presented at numerous international conferences.

Mr. Quaiyum was the recipient of the four year chancellor's fellowship at the University of Tennessee in August 2013. He also received the Best Oral Presentation Award at Microelectronics and Optoelectronics Symposium held at University of Connecticut in April 2014. He was also the recipient of the Chancellor's Citation Award for Extraordinary Professional Promise, in the years 2015, 2017 and 2018 from the University of Tennessee, Knoxville.